DISSERTATION

MORPHOLOGY, LIFECYCLES, AND ENVIRONMENTAL SENSITIVITIES OF TROPICAL TRIMODAL CONVECTION

Submitted by

George Alexander Sokolowsky

Department of Atmospheric Science

In partial fulfillment of the requirements

For the Degree of Doctor of Philosophy

Colorado State University

Fort Collins, Colorado

Fall 2022

Doctoral Committee:

Advisor: Susan C. van den Heever

Sonia M. Kreidenweis
Eric D. Maloney
Shantanu Jathar

ABSTRACT

MORPHOLOGY, LIFECYCLES, AND ENVIRONMENTAL SENSITIVITIES OF TROPICAL TRIMODAL CONVECTION

Convective clouds are ubiquitous in the tropics and typically follow a trimodal distribution of cumulus, congestus, and cumulonimbus clouds. Due to the crucial role each convective mode plays in tropical and global transport of heat and moisture, there has been both historical and recent interest in the characteristics, sensitivities, and lifecycles of these clouds. However, designing novel studies to further our knowledge has been challenging due to several limitations: the extensive computing resources needed to conduct modeling studies at sufficient resolution and scale to capture the trimodal distribution in detail; the lack of analysis tools which can objectively detect and track these clouds throughout their lifetime; and a need for more observational and modeling data of the tropical convective environments that produce these clouds. In this dissertation, three distinct but related studies that address these problems to advance the knowledge of our field on the morphology, lifecycles, and environmental sensitivities of tropical trimodal convection are presented.

The first study examines the sensitivities of the tropical trimodal distribution and the convective environment to initial aerosol loading and low-level static stability. The Regional Atmospheric Modeling System (RAMS) configured as a Large Eddy Simulation (LES) is utilized to resolve all three modes in detail through two full diurnal cycles. Three initial static stabilities and three aerosol profiles are independently and simultaneously varied for a suite of nine simulations. This research found that (1) large aerosol loading and strong low-level static

stability suppress the bulk environment and the intensity and coverage of convective clouds; (2) cloud and environmental responses to aerosol loading tend to be stronger than those from static stability; (3) the effects of aerosol and stability perturbations modulate each other substantially; (4) the deepest convection and highest dynamical intensity occur at moderate aerosol loading, rather than at low or high loading; and (5) most of the strongest feedbacks due to aerosol and stability perturbations are seen in the boundary layer (the latter being applied within the boundary layer themselves), though some are stronger above the freezing level.

The second study presented seeks to further enhance an artificial intelligence analysis tool, the Tracking and Object-Based Analysis of Clouds (*tobac*) Python package, from both a scientific and procedural standpoint to enable a wider variety of research uses, including process-level studies of tropical trimodal convection. Scientific improvements to *tobac v1.5* include an expansion of the tool from 2D to 3D analyses and the addition of a new spectral filtering tool. Procedural enhancements added include greater computational efficiency, data regridding capabilities, and treatments for processing data with singly or doubly periodic boundary conditions (PBCs). My distinct contributions to this work focused on the 2D to 3D expansion and the PBC treatment. These new capabilities are presented through figures, schematics, and discussion of the new science that *tobac v1.5* facilitates, such as the analysis of large basin-scale datasets and detailed simulations of layered clouds, that would have been impossible before.

Finally, the last study in this dissertation is a process-focused modeling study on the sensitivities of upscale growth of tropical trimodal convection to environmental aerosol loading. This project was enabled by the scientific and procedural improvements to *tobac* discussed in the second study, in particular the new abilities of *tobac* to detect and track objects in 3D and with model PBCs. Here, we used a subset of RAMS simulations from the first study, where only

aerosol loading was changed and the upscale growth from shallow cumulus through congestus and cumulonimbus during the nighttime hours was investigated. This study revealed that moderately increasing aerosol loading enhances collision-coalescence processes in the middle of the cloud, which delays initial glaciation but promotes it later in the growth period. Greatly increasing aerosol, however, produces a cloud structure with a more extreme aspect ratio and greater entrainment aloft that rapidly loses buoyancy and vertical velocity with height, as well as exhibiting a greater amount of condensate loading towards the top of the cloud. We also found the relative timing of these processes to be especially important, with more rapid initial growth and lofting of condensate often inhibiting deeper convective growth.

ACKNOWLEDGMENTS

As someone who was “bitten by the weather bug” upon seeing a tornado at age 6, completing a Ph.D. in Atmospheric Science has been a lifelong dream. However, it was by far the most challenging effort I have undertaken in my life, and I would not have made it this far without the support of many individuals and groups along the way. This is also the only part of the dissertation where I get to indulge my natural long-windedness, and I think it’s only fitting since I have so many people to thank and acknowledge.

First and foremost, I extend my deepest gratitude to my doctoral advisor, Dr. Susan van den Heever. Sue is a wonderful mentor who has greatly honed my skills and intuition as a scientist, encouraged me to pursue my own interests, and provided me with a great wealth of opportunities to broaden my intellectual horizons, such as participation in the CAMP^{2}Ex field campaign in the Philippines (one of the best experiences I’ve ever had). Equally as important as her academic advising, I have also found Sue to be extremely supportive with personal issues - not just the ordinary stresses that come along with the intense workload of a Ph.D., but also difficulties borne out of the COVID-19 pandemic and several serious health issues within my family. Without Sue, I could not have made it to where I am today.

I also want to thank my doctoral committee for their service: Drs. Sonia Kreidenweis, Eric Maloney, and Shantanu Jathar. Beyond their helpful perspectives and guidance as my committee members, I have also had the pleasure of taking classes taught by both Sonia and Eric, and have also interacted with Eric extensively in his role as Associate Department Head (now, Department Head) during my time as a department Grad Rep. I also benefited from Shantanu’s expertise in aerosols from a mechanical engineering point of view, which is a unique perspective

I was grateful to have on my committee. My Ph.D. dissertation and the work contained within it also would not have been possible without the financial support of NASA, who funded my research and Ph.D. degree through Grant # 80NSSC18K0149 – I am appreciative of NASA for this support as well!

Thanks also to the Meteorology and Atmospheric Science Department at Penn State University, where I received my B.S. and M.S. degrees in Meteorology. While I did not become a fully independent scientist until my doctoral studies at CSU, such an evolution would not have been possible without the fantastic education and mentorship I received during my 6 years at Penn State. I especially want to thank Drs. Eugene Clothiaux, Anthony Didlake, Steven Feldstein, Jerry Harrington, Tim Kane, Matt Kumjian, Sukyoung Lee, Jon Nese, Yvette Richardson, Dave Stensrud, and Hans Verlinde for their invaluable support and guidance during different stages of my Bachelors and Masters education.

I'd also like to thank the past and present members of the van den Heever Cloud Processes group for their friendship and intellectual support during my Ph.D. I truly believe that we have all lifted each other up to be better people and scientists during our time working together, and I have thoroughly enjoyed being a part of such a wonderful academic family. Special thanks are due to Dr. Jennie Bukowski, Dr. Aryeh Drager, Dr. Sean Freeman, Dr. Leah Grant, Bee Leung, Dr. Peter Marinescu, Dr. Minnie Park, and Steve Saleeby for their close friendship and fruitful scientific conversations/collaborations during my time in the group.

One of the most fulfilling aspects of my doctoral education has been the opportunity to participate in service at the Department level. During my time at CSU, I have been a Graduate Representative, a student member of the Diversity, Equity, and Inclusion (DEI) Committee, and a founding member of the leadership team for the CIRA/ATS Mentoring Program (CAMP)

which started last year. It has been incredibly fulfilling to be working alongside so many inspiring and motivated people who are passionate about making our great department even better, and I will greatly miss working with my colleagues on these efforts.

I was also fortunate enough to have the opportunity to participate on a field campaign deployment as part of my Ph.D. research – the Cloud, Aerosol, and Monsoon Processes Philippines Experiment ($CAMP^2Ex$), jointly administered by NASA, the Naval Research Laboratory, and the Manila Observatory. This campaign was based in Clark, Pampanga, Philippines and ran for about 2 months, during which time I was able to serve as the dropsonde instrument scientist on 13 of the 19 P-3 science flights. I also had opportunities to hike Mt. Pinatubo and present on my research to high school students on some of our down days, which were great experiences overall but especially helped to break up the intense work pace of field campaigns. In addition to my advisor Sue, who was the dropsonde PI for the campaign, special thanks are due to the late Dr. Gemma Narisma, Dr. Hal Maring, Dr. Jeff Reid, and others for ensuring that the field campaign went smoothly, and an especially huge thanks is due to the people of the Philippines for graciously hosting us in their country for the duration of this field campaign.

A great thanks is also due to my many friends and extended family who have supported me and my academic endeavors over the years. Principal among these is my wife, Dr. Minnie Park. I met Minnie the very first time I visited CSU in January 2018, and our friendship and relationship quickly blossomed after I started in the van den Heever group in August 2018. Minnie's presence and support through my Ph.D. have been unyielding, and I could not have possibly made it through the many academic hurdles, the difficulties of the COVID pandemic, and other struggles during my Ph.D. without her. I have met many wonderful people over the

years – including at various stages of school, in the neighborhood I grew up in, and even on travel – and I couldn't be more grateful for the companionship and emotional support of these friends, including that of my cousin and best friend, Jimmy McNicholas. There are many other family members who have supported me throughout the years as well: my mother Kathy, who is the most selfless and determined person I know, and raised my brother and I as a single parent for years; my brother Nick, who is the exemplification of maintaining optimism in the face of adversity; my grandparents Olimpia and Jim McNicholas, who always encourage my academic and scientific endeavors; and my Uncle and Godfather Bill Sokolowsky, who has been a father figure to me since losing my dad and always enthusiastically supported my chosen academic path. My family dog, Shyla, has been an additional source of comfort, peace of mind, and companionship through my doctoral studies. I also want to acknowledge my new extended family in Korea who have been incredibly helpful and supportive from afar: my Appa, Park Kwandong; my Umma, Jin Youngmi; and my new brother-in-law Park Sanghyun.

Lastly, I want to make a special note of dedication to the three most precious loved ones I have lost: my dad, George Sokolowsky; my aunt and Godmother, Mary Pillo; and my grandma, Alice Sokolowsky. All three of these people sadly passed away from cancer (with my Godmother and Grandma passing during my Ph.D. studies) and serve as continuous inspiration to be the best person and scientist I can be.

TABLE OF CONTENTS

CHAPTER 1 – INTRODUCTION

1.1) Overview of the tropical trimodal convective distribution

Convective clouds are ubiquitous within the tropics and play important roles in energy and moisture transport on both local and global scales (Riehl and Malkus 1958; Malkus and Riehl 1964; Schumacher et al. 2004; Harrop and Hartmann 2015). These clouds follow a trimodal distribution of cumulus, cumulus congestus (hereafter 'congestus') and cumulonimbus clouds first recognized by Johnson et al. (1999), in contrast to older bimodal models of tropical convection focusing solely on cumulus and cumulonimbus (Schubert 1976; Randall 1980; Emanuel 1994). This trimodal distribution manifests due to the existence of three tropical-mean layers of elevated stability (Johnson et al. 1999), and each mode also has a myriad of sensitivities to aerosol properties (van den Heever et al. 2011; Tao et al. 2012). Due to the connections between the modes and their environment, altering the bulk environment (mesoscale thermodynamic, condensate, and aerosol structure) may strongly impact the development of clouds within it, which subsequently also feeds back onto the environment.

Cumulus are the shallowest and most numerous convective clouds, both within the tropics and globally, and tend to be short-lived, dynamically weak, and lower in precipitation production versus their deeper counterparts (Johnson et al. 1999). These shallow tropical cumuli are variable in nature and sensitive to marine boundary layer characteristics (Wood et al. 2011), while also contributing strongly to the transport of heat and moisture within the boundary layer (Schumacher et al. 2004) and from the subtropics into the ITCZ core by affecting subtropical free tropospheric humidity, thereby impacting upscale growth of convection (Neggers et al. 2007). Cumulonimbus clouds' role in the global energy budget was first identified by Riehl and

Malkus (1958) who found them to drive the surface-to-tropopause transport of heat and mass within the tropics, which subsequently drive large-scale tropical convergence (Neelin and Held 1987) and ultimately support the heat losses and energy export towards the poles through the Hadley Cell circulation. Tropical cumulonimbus may manifest as either isolated convective towers or as parts of larger cloud systems (Cotton et al. 2011), with their organization and convective/stratiform precipitation percentage affecting the tropospheric heating structure (Schumacher et al. 2004).

Congestus clouds, however, were only recognized as being an important part of the trimodal distribution with the seminal work of Johnson et al. (1999), despite having been identified over 100 years earlier (Maze 1889). Johnson et al. found that congestus produced 28% of convective rainfall in the Tropical Ocean Global Atmosphere Coupled Ocean-Atmosphere Response Experiment (TOGA COARE; Webster and Lukas 1992) field campaign and suggested, as have others (Ruppert and Johnson 2015), that congestus clouds precondition the environment for deep convection. Some other studies (Hohenegger and Stevens 2013) found evidence for this hypothesis lacking in favor of mesoscale organization driving this preconditioning. Luo et al. (2009) classified congestus into transient and terminal categories depending on their buoyancy at the freezing level. This distinction strongly impacts the ability of congestus to grow upscale to cumulonimbus: Radiative-Convective Equilibrium (RCE) studies of trimodal convection conducted by Posselt et al. (2008) identified the formation of vertical circulations separated by the trade, freezing level and tropopause inversions. Finally, congestus heating profiles resemble those of shallow cumulus and isolated cumulonimbus, but typically extend to the freezing layer (Schumacher et al. 2004, 2007). In the next subsection, we discuss some of the findings on these

sensitivities in previous literature and their motivation of the studies contained within this dissertation.

1.2) Environmental Sensitivities of Tropical Trimodal Convection

While ubiquitous throughout the tropics, these three convective modes exhibit a myriad of sensitivities to their environment that can substantially alter their characteristics on a variety of scales and even locally suppress deeper convection altogether. Both the thermodynamic and aerosol environments in and around the Maritime Continent (MC), and the Philippines more specifically, are subject to a great deal of variance that influences cloud properties. These environments and associated interactions between aerosols, clouds, and thermodynamics were studied extensively during the recent Cloud, Aerosol, and Monsoon Processes Philippines Experiment ($CAMP^2Ex$; Reid et al. 2022) field campaign conducted by NASA, NRL, and the Manila Observatory (MO). Thermodynamically, this region is well-characterized by the tropical West Pacific warm pool environment identified by Yanai et al. (1973) but is also subject to natural variance. The aforementioned Posselt et al. study identified that the 3 prominent tropical-mean stable layers separate vertical circulations, and thus variations in these layers (as well as any changes due to large-scale oscillations) can substantially impact the convection produced here (e.g. Del Genio and Kovari 2002; Masunaga et al. 2005; Jakob et al. 2005; Benedict and Randall 2007; Del Genio et al. 2012; Toms et al. 2020a,b).

Aerosol particles in the MC originate from a variety of sources: transportation, agriculture, heavy industry, biomass burning, and natural marine processes, among other causes, and number concentrations of these particles can range from tens to thousands per cubic centimeter (Reid et al. 2013, 2016a,b; Hilario et al. 2020). Aerosols directly scatter solar radiation and some species also absorb it (the “direct effect” and “semi-direct” effect,

respectively; Charlson and Pilat 1969; Ackerman et al. 2000) and impact clouds via cloud-aerosol interactions or "Aerosol Indirect Effects" (AIEs), which have also been observed in this geographic region (Rosenfeld and Lensky 1998). Increases in aerosol number concentrations have long been recognized to produce a narrower distribution of cloud drops than would be in the presence of lower concentrations at the same liquid water content (Squires 1958), thereby resulting in a suppression of warm rain production (e.g. Squires and Twomey 1960; Warner and Twomey 1967), an increase in cloud albedo (e.g. Twomey 1974, 1977; Twomey et al. 1984) and cloud lifetime (Albrecht 1989), and reduced precipitation in low clouds (e.g. Feingold et al. 1996; Xue et al. 2008; Saleeby et al. 2015). Deeper convective clouds have far more complex AIEs that have been more challenging to disentangle. Many studies have discussed convective invigoration as an AIE in deeper convection (Andreae et al. 2004; Khain et al. 2005; van den Heever et al. 2006; Rosenfeld et al. 2008; Fan et al. 2009; Altaratz et al. 2010), though some of these findings of invigoration have been tied to mitigating factors such as wind shear, CAPE, and RH (Khain et al. 2008; Fan et al. 2009; Storer et al. 2010, 2014; Lebo and Morrison 2014); have been disputed (Grabowski 2018; Varble 2018) or have been nonmonotonic with increasing loading (Tao et al. 2012; Altaratz et al. 2014; Marinescu et al. 2021). Some of this uncertainty appears rooted in aerosol-induced convective invigoration being a balancing act between condensate loading, buoyancy, and updraft strength (e.g., Lebo and Seinfeld 2011; Lebo et al. 2012; Grabowski and Morrison 2020; Igel and van den Heever 2021) and the impacts to ice-phase processes, with some studies showing weaker updrafts for cold-based clouds (Igel and van den Heever 2021) or a mixed ice phase response across modeling platforms despite robust warm-phase invigoration (Marinescu et al. 2021). In contrast to the deep convective mode, relatively little attention has been paid to congestus. Li et al. (2013) and Sheffield et al. (2015) are among

the few who have specifically explored aerosol impacts on congestus, and despite different modeling frameworks, both found a dynamical invigoration of congestus from increases in aerosol content.

Many of these environmental sensitivities of tropical trimodal convection were gleaned through either observational or modeling studies which used snapshot or bulk analyses of convective clouds. However, these kinds of approaches are unable to capture temporal evolution of such clouds at a process level, which is crucial for understanding how the convective modes develop – i.e., why do some cumuli grow upscale to congestus while others remain shallow, and further, why do some congestus clouds terminate in this mode while others continue growing upscale to cumulonimbus? Due to these gaps in understanding, temporally focused studies of trimodal convective cloud evolution are needed, but no tracking tools capable of analyzing such a complex scene existed until recently.

1.3) History of Tracking Tools for Convection and Other Atmospheric Phenomena

Recently, there has been great interest in robust, large-scale objective identification and tracking of clouds and other meteorological features (e.g., Heus and Seifert, 2013; Hu et al., 2019; Núñez Ocasio et al., 2020). As the atmosphere is not a static system, diffusive, advective, dynamic, and thermodynamic processes ensure that atmospheric phenomena of interest are nearly always either in motion or in a moving frame of reference, which is indicative of the utility of tracking frameworks for atmospheric data in general. Clouds are one such phenomenon for which tracking is useful: they are near-ubiquitous features in the Earth's atmosphere; play critical roles in tropospheric heat and moisture transport; scatter shortwave (SW) radiation and absorb/emit longwave (LW) radiation; and strongly impact the global climate. Convective clouds and cloud systems can range in size from tens of meters to hundreds of km; exist for as short as a

few minutes and as long as days; exhibit a wide variety of morphological characteristics; and undergo complex lifecycles (Cotton et al. 2011). All of these elements make clouds prime candidates for objective analysis techniques (e.g. Gill and Rasmusson 1983; Weickmann 1983; Marinescu et al. 2021), but they are far from the only atmospheric phenomena where robust tracking tools are useful. For example, tracking has been performed on convective cold pools (e.g. Tompkins, 2001; Feng et al., 2015; Drager and van den Heever, 2017; Drager et al., 2020); large-scale phenomena such as Mesoscale Convective Systems (MCSs), tropical and extratropical cyclones, and atmospheric waves (e.g. Ullrich and Zarzycki 2017; Núñez Ocasio et al. 2020) aerosol and trace gas advection (Bukowski and van den Heever, 2021; Zhang et al., 2022); and even bird and bug seasonal migration (e.g. Crewe et al., 2020; Knight et al., 2019). This clearly indicates that if such tools are made general enough, people working outside the realm of atmospheric science can also benefit from them. Presently, only one such tool can address all these uses: the Tracking and Object-based Analysis of Clouds (*tobac*; Heikenfeld et al., 2019) library, a Python package based in objective analysis principles that uses artificial intelligence to identify, discretize, and track objects and fields of interest.

The most powerful and unique feature of *tobac* is its variable and grid agnosticity – i.e., it can be used with virtually any gridded input dataset and variable, meteorological or not. *tobac* was initially developed for use with clouds and associated meteorological data (Heikenfeld et al. 2017), and has been used for applications such as tracking warm-season deep convective systems and MCSs via satellite-observed infrared brightness temperature (e.g. Li et al., 2021; Kukulies et al., 2021, respectively). However, due to this unique variable agnosticity, *tobac* has also had other uses: for example, tracking of haboobs via dust concentration (e.g. Bukowski and van den

Heever, 2021). *tobac* both draws from and expands upon the procedures developed in earlier cloud identification and tracking tools.

Historically, tracking has required a great deal of human input and attention due to a lack of computationally efficient methods for the location, assessment, and connection of different features in time. One such early method, the Thunderstorm Identification, Tracking, Analysis, and Nowcasting tool (TITAN; Dixon and Weiner, 1993), is a well-designed and powerful approach for the detection and tracking of thunderstorms, and while it does incorporate computational analysis of data, it is heavily based in physical principles (i.e., it requires specific datasets/variables and can only be used to track certain things) and manual assessment of output due to computational limitations at the time. As discussed in Dawe and Austin (2012), earlier studies involving tracking of clouds (e.g. Zhao and Austin, 2005a, b; Heus et al., 2009) required scientists to contribute a great degree of manual/visual selection of the clouds they considered in their studies. This is time-consuming to the extent that is impossible to scale for large datasets and introduces subjectivity to an analysis that should ideally be objective. Some later studies (e.g. Plant, 2009; Dawe and Austin, 2012; Heus and Seifert, 2013) have more general criteria allowing for automated selection, but exhibit computational or scientific limitations due to their design. For example, Dawe and Austin's (2012) and Heus and Seifert's (2013) methods were designed to be used in LES output fields of shallow cumuli with a vertical extent of less than 4 km, limiting the applicability of these methods with cloud systems that exhibit more vertical structure (e.g., layered clouds, deep convection, or slantwise convection) and other datasets with similarly complex 3D morphology. A number of other tools, while powerful and reliable for certain meteorological structures such as large thunderstorms, MCSs, and supercells, are similarly limited by their specific case uses and cannot be easily generalized (e.g. Dixon and

Weiner, 1993; Gambheer and Bhat, 2000; Hu et al., 2019; Núñez Ocasio et al., 2020, Gropp and Davenport, 2021). *tobac* utilizes many of the strengths of these preexisting tools while broadening science applications and optimizing procedures to result in a more general and powerful analysis tool.

Despite the utility of *tobac* and the strengths of this tool over earlier such packages, the increasing resolution of models and identification of new use cases (e.g., in LES modeling) led us to recognize that the code base required both scientific and procedural enhancements. Introducing these improvements to *tobac* not only serves to enable the kind of process-focused studies referenced in Section 1.2, but also facilitates a wide breadth of science approaches and applications across different subfields of atmospheric science as well as a multitude of other disciplines.

1.4) Upscale Growth of Tropical Convection

Exploring the evolution of tropical convective growth and its sensitivities is, as discussed in Section 1.2, essential to understanding how the different modes of the tropical trimodal distribution develop. It is generally agreed that these clouds follow a dynamic lifecycle comprised of growth, mature/steady-state, and decay stages (e.g. Byers and Braham, 1948; Betts, 1973; Cruz, 1973; Cotton et al., 2011). The growth stage is dominated by updrafts, positive vertical mass flux, and a rising cloud top or radar echo height; the steady-state or mature stage is comprised of a mix of updrafts and downdrafts with little change in vertical cloud top or radar echo position; and the decay stage exhibits a decreasing cloud or echo top height, prevalence of downdrafts throughout the system, and a net negative vertical mass flux (Byers and Braham, 1948; Cruz, 1973; Betts, 1973). However, at the time of writing, surprisingly few observations of convective cloud vertical velocities exist, particularly over global oceans (Battaglia et al., 2013),

that can be used to evaluate theories on convective lifecycles and the upscale growth of convective clouds. Collecting the data needed to characterize these different stages is challenging due to the opacity of moderate-to-strong convection to common remote sensing platforms (e.g. W-band attenuation; Tanelli et al. 2008), the difficulty of timing, placement, and accuracy in measurement of ground-based in situ observations for interaction with convection (e.g. tethered balloons or radiosonde launches; Cotton et al. 2011; Marinescu et al. 2020), and the dynamical intensity of such systems requiring specific airborne platforms and targeted intrusions to safely collect data (e.g. Geerts et al., 2018). These challenges and historical dearth in observations of the time evolution of cumulonimbus were key motivations behind the recently funded Investigation of Convective Updrafts (INCUS; van den Heever 2022) NASA Earth Ventures mission, which will use a constellation of satellites with a variety of remote sensing equipment to capture the temporal evolution of tropical convective updrafts.

Due in part to this historical lack of observations, modeling studies are crucial to both bridge this gap in knowledge and provide a context within which future observations can be placed and examined at a process level. Modeling studies of AIEs on convection (e.g. convective invigoration) are also critical for advancing our knowledge, as the intertwined responses of microphysics, dynamics, and precipitation are extremely difficult to disentangle without being able to ascertain the process evolution in some way. It is clear when considering the collective scientific history of tropical convection, convective upscale growth, and objective tracking tools that a multi-pronged approach including both novel scientific approaches and new scientific tools is necessary to pursue a robust examination of trimodal convective sensitivities.

1.5) Outline of Dissertation

In summary, the primary goal of the research contained in this dissertation has been to explore the morphology, sensitivities, and upscale growth of tropical trimodal convection. As discussed in the previous subsections, an extensive, combined approach which investigates bulk analyses of trimodal convective sensitivities, improves existing analysis and tracking tools, and utilizes these tools to conduct a process-based assessment are essential to understand the trimodal distribution's sensitivities to aerosol loading.

To outline the remainder of this dissertation, Chapter 2[1] presents the results of an LES modeling study using the Regional Atmospheric Modeling System (RAMS; Pielke et al. 1992; Cotton et al. 2003; Saleeby and van den Heever 2013) which explores the individual and integrated impacts of initial low-level static stability and aerosol on tropical trimodal convection using bulk analyses of the environment and each mode of the tropical trimodal distribution. Chapter 3[2] details the development and details of key scientific (e.g. including the third spatial dimension) and procedural (e.g. including a PBC treatment) improvements contained within *tobac v1.5*, the newest version of this tool, which were essential to perform the final study detailed in this dissertation. Chapter 4[3] discusses a Lagrangian object- and process-oriented

---

[1] This study, entitled "Sensitivities of Maritime Tropical Trimodal Convection to Aerosols and Boundary Layer Static Stability", has been published at the Journal of the Atmospheric Sciences (Sokolowsky et al. 2022, ©American Meteorological Society). Sokolowsky, G.A., S.W. Freeman, and S.C. van den Heever (2022). Sensitivities of Maritime Tropical Trimodal Convection to Aerosols and Boundary Layer Static Stability. *J. Atmos. Sci.* https://doi.org/10.1175/JAS-D-21-0260.1

[2] This study, entitled "*tobac* v1.5: Introducing Fast 3D Tracking, Splits and Mergers, and Other Enhancements for Identifying Meteorological Phenomena", is a joint-first-author paper led by G.A. Sokolowsky and S.W. Freeman, and is currently in preparation for submission to Geoscientific Model Development (Sokolowsky and Freeman et al. 2022 – in preparation)

[3] This study, entitled "Upscale Growth Sensitivities of Tropical Trimodal Convection to Aerosol", is currently in preparation for submission to the Journal of Geophysical Research (Sokolowsky and van den Heever 2022 – in preparation)

RAMS modeling endeavor which utilizes a subset of the simulations in Chapter 2 and focuses on the changes in the convective growth stage between the three modes of convection at different initial aerosol loadings. Finally, Chapter 5 presents a summary of the dissertation studies, key conclusions, and the future work avenues this research has enabled.

CHAPTER 2 – BULK SENSITIVITIES OF TRIMODAL CONVECTION TO ENVIRONMENTAL STABILITY AND AEROSOL[1]

2.1) Introduction

Convective clouds are ubiquitous within the tropics and play important roles in energy and moisture transport on both local and global scales (Riehl and Malkus 1958; Malkus and Riehl 1964; Schumacher et al. 2004; Harrop and Hartmann 2015). These clouds follow a trimodal distribution of cumulus, cumulus congestus (hereafter 'congestus') and cumulonimbus clouds first recognized by Johnson et al. (1999), in contrast to older bimodal models of tropical convection focusing solely on cumulus and cumulonimbus (Schubert 1976; Randall 1980; Emanuel 1994). This trimodal distribution manifests due to the existence of three tropical-mean layers of elevated stability (Johnson et al. 1999). The individual modes also have a myriad of sensitivities to aerosol properties (Tao et al. 2012). Due to the connections between the modes and their environment, altering the bulk environment (mesoscale thermodynamic, condensate, and aerosol structure) may strongly impact the development of clouds within it, which subsequently also feeds back onto the environment.

Cumulus are the shallowest and most numerous convective clouds, both within the tropics and globally, and tend to be short-lived, dynamically weak, and lower in precipitation production versus their deeper counterparts (Johnson et al. 1999). These shallow tropical cumuli typically cease growing below the tropical-mean trade wind inversion around 2 km above ground

---

[1] This study, entitled "Sensitivities of Maritime Tropical Trimodal Convection to Aerosols and Boundary Layer Static Stability", has been published at the Journal of the Atmospheric Sciences (Sokolowsky et al. 2022, ©American Meteorological Society). Sokolowsky, G.A., S.W. Freeman, and S.C. van den Heever (2022). Sensitivities of Maritime Tropical Trimodal Convection to Aerosols and Boundary Layer Static Stability. *J. Atmos. Sci.* https://doi.org/10.1175/JAS-D-21-0260.1

level (e.g. Rauber et al. 2007; Ghate et al. 2016), and are "closely linked to turbulence within the marine boundary layer that is primarily driven by the surface turbulent fluxes, radiative cooling, and wind shear" per Ghate et al. Not only are these clouds variable in nature and sensitive to marine boundary layer characteristics (Wood et al. 2011), but they also strongly contribute to the transport of heat and moisture within the boundary layer (Schumacher et al. 2004) and act as a "humidity throttle" on deep convection within the ITCZ core by impacting the humidity of the subtropical free tropospheric air which is advected towards the ITCZ core (Neggers et al. 2007). Riehl and Malkus (1958) identified the role of cumulonimbus clouds, which they hypothesized to be undilute and referred to as "hot towers", in surface-to-tropopause transport of heat and mass within the tropics. These clouds often extend to the tropopause, and based on the assumption of undilution, Riehl and Malkus determined that about 1500 – 5000 hot towers were required to support the heat losses and energy export from the tropics. Later theoretical and modeling studies (e.g. Zipser 2003) found this assumption to be unnecessary if boosts to moist static energy from glaciation were accounted for in balancing cloud entrainment. Tropical cumulonimbus may manifest as isolated convective towers, or as parts of larger cloud systems (Cotton et al. 2011). Isolated cumulonimbus heat through the troposphere, though organization and convective/stratiform percentage affect the heating profile structure (Schumacher et al. 2004).

Congestus clouds were only recognized as being an important part of the trimodal distribution with the seminal work of Johnson et al. (1999), despite having been identified over 100 years earlier (Maze 1889). Congestus are common in the tropics and exhibit a vertical extent reaching to the freezing stable layer (~4-6 km in the tropics; Johnson et al. 1999) and sometimes beyond (Luo et al. 2009). Johnson et al. found that congestus produced 28% of convective rainfall in the Tropical Ocean Global Atmosphere Coupled Ocean-Atmosphere Response

Experiment (TOGA COARE; Webster and Lukas 1992) field campaign and suggested, as have others (Ruppert and Johnson 2015), that congestus clouds precondition the environment for deep convection by moistening it. Some other studies (Hohenegger and Stevens 2013) found evidence for this hypothesis lacking in favor of mesoscale organization driving this preconditioning. Radiative-Convective Equilibrium (RCE) studies of trimodal convection conducted by (Posselt et al. 2008) identified the formation of vertical circulations separated by the trade, freezing level and tropopause inversions, the middle one of which is likely to impact upscale growth of congestus into deeper convection. Luo et al. (2009), for example, classified congestus into transient and terminal categories depending on their buoyancy at the freezing level. Congestus heating profiles resemble those of shallow cumulus and isolated cumulonimbus, but typically extend to the freezing layer (Schumacher et al. 2004, 2007).

Both the thermodynamic and aerosol environments in and around the Maritime Continent (MC), and the Philippines more specifically, are subject to a great deal of variance, which, as stated previously, influences cloud properties. These environments and associated interactions between aerosols, clouds, and thermodynamics were studied extensively during the recent Cloud, Aerosol, and Monsoon Processes Philippines Experiment (CAMP^{2}Ex; Reid et al. 2022) field campaign conducted by NASA, NRL, and the Manila Observatory (MO). Thermodynamically, this region is well-characterized by the tropical West Pacific warm pool environment identified by (Yanai et al. 1973) but is also subject to natural variance including several large-scale oscillations that alter thermodynamic environments and influence cloud fields. The aforementioned Posselt et al. study identified that the 3 prominent tropical-mean stable layers separate vertical circulations, and thus variations in these layers (as well as any changes due to large-scale oscillations) can substantially impact the convection produced here (e.g.(Del Genio

and Kovari 2002; Masunaga et al. 2005; Jakob et al. 2005; Benedict and Randall 2007; Del Genio et al. 2012; Toms et al. 2020a,b)

Aerosol particles in the MC originate from a variety of sources: transportation, agriculture, heavy industry, biomass burning, and natural marine processes, among other causes, and number concentrations of these particles can range from tens to thousands per cubic centimeter (Reid et al. 2013, 2016a,b; Hilario et al. 2020). Aerosols directly scatter solar radiation (the "direct effect"; Charlson and Pilat 1969) and impact clouds via cloud-aerosol interactions or "Aerosol Indirect Effects" (AIEs), which have also been observed in this geographic region (Rosenfeld and Lensky 1998). Increases in aerosol number concentrations have long been recognized to produce a narrower distribution of drops than would be in the presence of lower concentrations (Squires 1958), thereby resulting in a suppression of warm rain production (e.g. Squires and Twomey 1960; Warner and Twomey 1967), an increase in cloud albedo (e.g. Twomey 1974, 1977; Twomey et al. 1984) and lifetime (Albrecht 1989), and reduced precipitation in low clouds (e.g. Feingold et al. 1996; Xue et al. 2008; Saleeby et al. 2015). Deeper convective clouds have far more complex AIEs that have been more challenging to disentangle. Many studies have discussed convective invigoration as an AIE in deeper convection (Andreae et al. 2004; Khain et al. 2005; van den Heever et al. 2006; Rosenfeld et al. 2008; Fan et al. 2009; Altaratz et al. 2010), though such findings of invigoration have been disputed (Grabowski 2018; Varble 2018) or have not been uniform with loading (Tao et al. 2012; Altaratz et al. 2014; Marinescu et al. 2021). Some of this uncertainty appears rooted in aerosol-induced convective invigoration being a balancing act between condensate loading, buoyancy, and updraft strength (e.g., Lebo and Seinfeld 2011; Lebo et al. 2012; Grabowski and Morrison 2020) and the impacts to ice-phase processes, with some studies showing weaker updrafts for

cold-based clouds (Igel and van den Heever 2021) or a mixed response across modeling platforms despite robust warm-phase invigoration (Marinescu et al. 2021). In contrast to the deep convective mode, relatively little attention has been paid to congestus. Li et al. (2013) and Sheffield et al. (2015) are among the few who have specifically explored aerosol impacts on congestus, and despite different modeling frameworks, both found a dynamical invigoration of congestus from increases in aerosol content.

The goal in this study is to use high-resolution numerical models to explore how individually and simultaneously varying initial low-level thermodynamic and aerosol properties affect the evolution of the bulk environment and the nature of the three modes of the tropical convective cloud distribution contained within it. To address this goal, we ran a suite of idealized LES model experiments for two full diurnal cycles in which we covaried the initial thermodynamic and aerosol environments. Section 2.2 describes our model and experimental setups; Section 2.3 details our results and analysis with foci on the bulk environment and convective cloud modes; and Section 2.4 presents our conclusions and future work directions.

2.2) Model Setup and Experiments

2.2.1) Model Setup

The simulations were conducted using the Regional Atmospheric Modeling System (RAMS) v. 6.2.12 (Pielke et al. 1992; Cotton et al. 2003; Saleeby and van den Heever 2013; van den Heever et al. 2021b). RAMS is a fully compressible, non-hydrostatic model with bin-emulating 2-moment bulk microphysics (Meyers et al. 1997), 2-stream radiative transfer (Harrington 1997), a fully interactive land surface model (Lee 1992; Walko et al. 2000), and a sophisticated aerosol scheme that allows for radiative interactions (Saleeby and van den Heever 2013).

For this study, we chose to run RAMS as an LES model (Table 2.1) on a grid of 150 km x 150 km x 17.6 km. We used a horizontal grid spacing of 100 m, with vertical grid spacing stretched from 50 m to 300 m, and a timestep of 0.75 s with a total integration time of 48 hours. The domain was centered at 4.46 ºN, 126.9 ºE (south of Mindanao in the Philippines) and the surface was fully ocean, with a uniform SST of 302.1 K (area-averaged from 3.25-5.50 ºN, 125.75-128.00 ºE in European Centre for Medium-Range Weather Forecast Re-Analysis (ERA-5) data (Hersbach et al. 2018). As these experiments are idealized, small islands present in reality were removed from our domain for simplicity. The top boundary was a rigid lid, with 4 Rayleigh damping levels for dispersion of gravity waves, and the lateral boundaries were cyclic. Aerosols were configured to be a single mode of ammonium sulfate/dust composite aerosols (each component being a common species in the MC; Atwood et al. 2017), with a lognormal distribution that had a geometric mean radius of 0.09 μm and geometric standard deviation of 1.8 (Reid and Wang 2020, personal communication). No sources or sinks of aerosols were included but they were radiatively active and could advect and diffuse around the domain. The basic initial thermodynamic profile is horizontally homogeneous (Fig. 2.1a), and was produced by interpolating a coarser basin-scale simulation by one of the authors (Freeman et al. 2019, 2022) onto a finer grid, and then area-averaging the thermodynamics from 4.2-4.6 ºN and 127.2-128.8 ºE on 21 August 2018, a region which primarily contained shallow convection. Over the course of the model runs, all experiments described below produce convection at a range of depths, accurately capturing the trimodal distribution (Fig. 2.2).

Table 2.1: A summary of the RAMS LES model options and experimental configuration used in this study.

Model Aspect	Setting
Model Version	RAMS v. 6.2.12 (Pielke et al. 1992; Cotton et al. 2003; Saleeby and van den Heever 2013; van den Heever et al. 2021b)
Dimensionality	3D
Grid	Arakawa C-Grid (Arakawa and Lamb 1977) Cartesian Projection centered at 4.4673 N, 126.900 E dx = dy = 100 m 1500 x 1500 x-y gridpoints (150 km x 150 km domain) 98 stretched vertical levels dz stretched from 50 m to 300 m at 1.026 ratio Model top approx. 17.6 km
Time Step	0.75 s
Simulation Duration	48 hours, starting at 0000Z on 21 August 2018
Boundary Conditions	Cyclic in both horizontal directions 4 Rayleigh damping layers at top beneath rigid lid Rigid bottom level with a fixed SST and no land surface
Surface Treatment	LEAF-3 Model (Lee 1992; Walko et al. 2000) Fully ocean domain with constant SST = 302.1 K Set from spatially averaged ERA-5 reanalysis data (Hersbach et al. 2018)
Initialization	Horizontally homogeneous initial sounding – averaged from a region producing mostly shallow convection in a basin-scale simulation nudged with ERA-5 data (Freeman et al. 2019, 2022) Convection initialized with random perturbations
Microphysics	Two-Moment Bin-Emulating Bulk (Meyers et al. 1997) Cloud, Drizzle, Rain, Pristine Ice, Snow, Aggregates, Graupel, Hail species Ice nucleation following DeMott et al. (2010)
Aerosol Treatment	Overall treatment follows (Saleeby and van den Heever 2013) Initialized as exponential profile based on prescribed surface concentration Composite Ammonium Sulfate/Dust CCN aerosol; no Giant CCN (GCCN), dust, or sea salt modes Composite Ice Nuclei (IN; DeMott et al. 2010) with surface concentration 10 L^{-1} No aerosol sources or sinks, aerosol radiative activity on
Radiation	Harrington 2-stream radiation (Harrington 1997), updated every 5 minutes

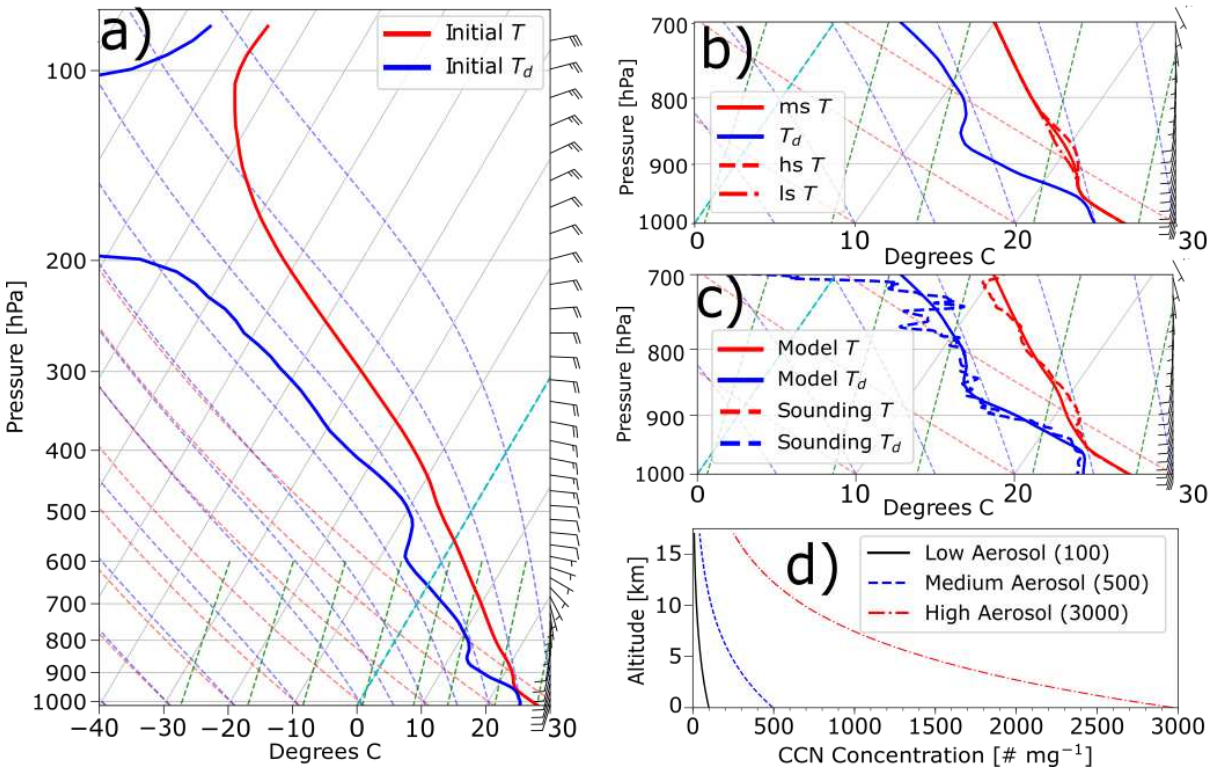

Figure 2.1: Thermodynamic and aerosol profiles used in our LES numerical experiments. Various thermodynamic and aerosol profiles are shown demonstrating the range of thermodynamic and aerosol conditions applied: (a) the medium stability thermodynamic profile derived from the Freeman et al. (2019) basin-scale run, (b) the temperature perturbations applied, (c) a comparison of the domain mean profile in the lower troposphere after 4 hours of model time in the ms-100 simulation to a CAMP^{2}Ex dropsonde observation from 1 October 2019, and (d) a depiction of the 3 initial aerosol profiles used.

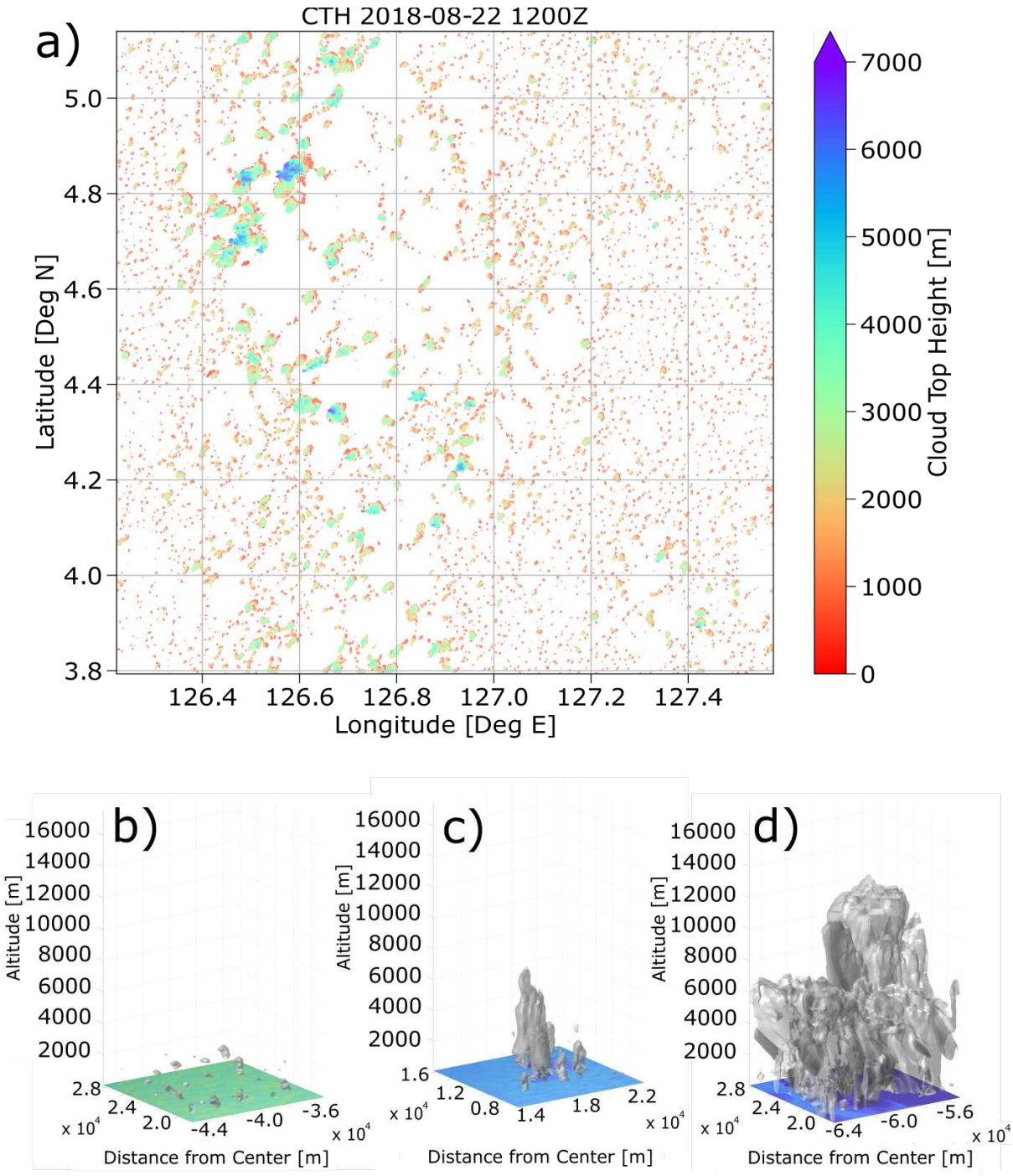

Figure 2.2: Depictions of the cloud fields represented in the simulations. (a) a plan view of the cloud top height field for the full domain of the ms-100 simulation after 36 hours of model time; (b-d) examples of cumulus, congestus, and cumulonimbus (respectively) plotted on limited domains from different times in the ms-100 simulation.

2.2.2) Experiment Setup

In our numerical experiments, we initialized the simulations with 3 different thermodynamic profiles and 3 different surface aerosol concentrations, comprising a total of 9 experiments (Table 2.2). The naming scheme we use for reference, also shown in Table 2.2, combines a stability prefix (*ls*, *ms*, or *hs* for low, medium, or high stability, respectively) with an aerosol suffix ("100", "500", or "3000", denoting the surface aerosol mixing ratio in mg^{-1}). The thermodynamics shown in Figure 1a were used for the *ms* runs, and the *ls* and *hs* profiles were perturbed by applying a negative or positive Gaussian temperature perturbation, respectively, with a maximum amplitude of 0.5 K between ~600 – 2000 m above ground level (Fig. 2.1b). The Gaussian perturbation allows for a smooth perturbation of temperature without producing discontinuities in the thermodynamic profile, and these perturbations are representative of the static stability range seen in five CAMP^{2}Ex flights (Reid et al. 2022) where similar cloud fields exhibiting convective clouds with a low cloud fraction were observed (Fig 2.3). The ms-100 profile produces a simulation environment representative of CAMP^{2}Ex and the West Pacific warm pool (Fig. 2.1c), and the details of the evolution of static stability is discussed in Section 3. Aerosol mixing ratio profiles decay exponentially with height (initial setups seen in Fig. 2.1d), and the surface values used were based on observations made in the region of the field campaign (Reid et al. 2013, 2016a,b; Atwood et al. 2017; Reid and Wang 2020, personal communication). Aerosol advection and diffusion near the surface reduce our initial surface mixing ratio by about 15% at the end of the ls-100 simulation, and advection leads to some vertical stratification of aerosol, but the initial profile remains largely intact above the well-mixed surface layer. In our results and analysis, the ls-100 simulation was designated as our control simulation due to having the least stability and aerosol versus the remainder.

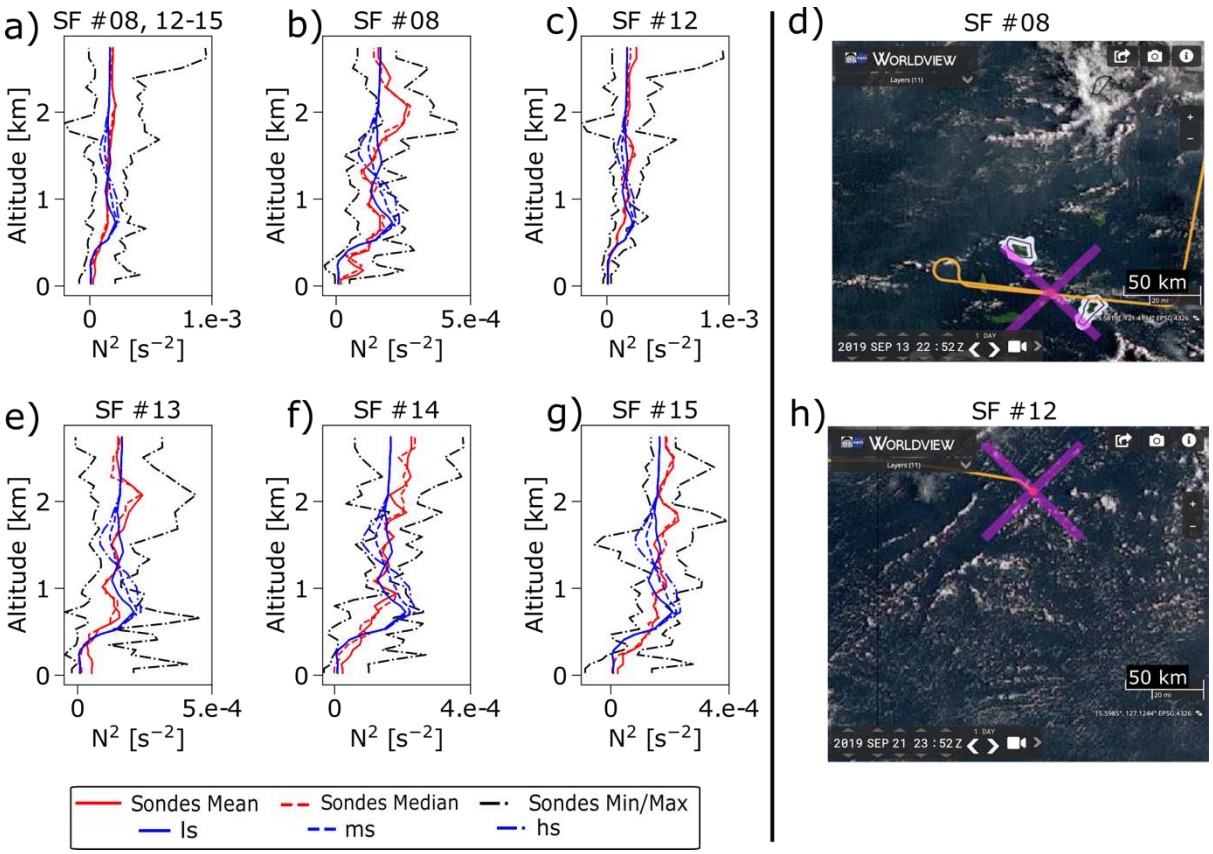

Figure 2.3: Vertical profiles of our initial static stability settings (quantified as N^2, the square of the Brünt-Väisälä frequency) versus those collected from CAMP^{2}Ex dropsondes launched in conditions comparable to our simulations. Panel (a) shows values from all of Science Flights 8 and 12-15, whereas panels (b)-(c) and (e)-(g) show those from the individual flights 8, 12, 13, 14, and 15, respectively. Panels (d) and (h) display Himawari-8 1 km visible satellite imagery from Science Flights 8 and 12, respectively. The red solid and red dashed lines on the stability panels represent the sondes' mean and median for each flight grouping, the black dash-dotted lines represent the sondes' minimum and maximum for each grouping, and the solid, dashed, and dash-dotted blue lines represent the values from our low stability, medium stability, and high stability simulation initial settings, respectively. Also note the different x-axis scaling between different panels. Panels (d) and (h) display Himawari-8 1 km visible satellite imagery from Science Flights 8 and 12, respectively. In panels (d) and (h), P-3 position and flight track are denoted by the magenta "X" and orange line, respectively. (University of Wisconsin/NASA GeoWorldview Website (http://geoworldview.ssec.wisc.edu)).

Table 2.2: A depiction of the experimental suite presented within this study and the naming convention used. "B-V freq." here denotes the Brunt-Väisälä frequency at initialization.

	Low Aerosol 100 mg^{-1} at surface	Medium Aerosol 500 mg^{-1} at surface	High Aerosol 3000 mg^{-1} at surface
High Stability ~ +6% max B-V freq. from Fig 1a ~ +0.85% mean B-V freq. from Fig 1a	"hs-100"	"hs-500"	"hs-3000"
Medium Stability Uses Fig. 1a profile	"ms-100"	"ms-500"	"ms-3000"
Low Stability ~ -6% max B-V freq. from Fig 1a ~ -0.85% mean B-V freq. from Fig 1a	"ls-100" (CONTROL)	"ls-500"	"ls-3000"

After conducting these experiments, our methodology for analyzing results largely seeks to capture the changes and responses in domain-wide and domain-mean cloud and environmental qualities, and to further assess changes in certain key variables within the specific modes of the tropical trimodal convective distribution. Most of these properties were assessed at 5-minute temporal resolution, though some of the analyses include temporally integrated contoured-frequency-by-altitude diagrams (CFADs; Yuter and Houze 1995), and spatiotemporal means of cloud properties. For all analyses, the first 2 hours of simulation time were considered as model spin-up and discarded. At each analysis timestep, the total condensate field was masked to hide values less than 0.01 g/kg (the same threshold as van den Heever et al. 2011 and Sheffield et al. 2015), and the "label" function from the Python SciPy package (Weaver 1985; Virtanen et al. 2020) was used to identify contiguous 3D regions of condensate above this threshold. All convective cloud regions were required to be contiguous in 3D space and have a cloud base below 2 km, with cumulus terminating below 4 km, congestus from 4 to 7 km, and deep convection above 7 km (Johnson et al. 1999; Sheffield et al. 2015; see examples in Fig. 2.2). The coordinates of different clouds were grouped by mode for our analysis, and below we report the

means and standard deviations of key properties when at least one cloud of that mode was present. Our horizontal grid spacing of 100 m allows us to capture all modes of the tropical trimodal distribution, and is comparable to previous LES studies of cumulus clouds (e.g. Xue et al. 2008). However, the very smallest cumulus clouds (length of order ~200 m or less; Wang et al. 2009; Ghate et al. 2016) will not be adequately represented (Heus and Seifert 2013). As the vast majority of clouds (> 90%) by surface area and volume are properly resolved, we feel that this grid spacing is sufficient for this study.

2.3) Results and Analysis

2.3.1) Bulk Dynamics and Microphysics Responses to Static Stability and Aerosol

We start by providing an overview of the environmental evolution of our simulations, quantified via static stability, radiative transfer, cloud fraction, dynamical intensity (updraft and downdraft strengths), and condensate glaciation. While panel (g) in each of Figures 2.4-2.10 represents the control simulation and shows actual values of the property of interest, the remaining panels demonstrate differences or percent changes from control (control being the ls-100 run; EXPERIMENT – CONTROL). Initial static stability and aerosol increase when moving upwards and rightwards amongst the figure panels, respectively. Precipitation responses largely reflected the findings of previous literature: with increased aerosol loading, the total precipitation and number of raining columns were reduced, while some of the raining columns did demonstrate increases in precipitation intensity (e.g. Albrecht 1989; Xue et al. 2008; Lebo and Seinfeld 2011; van den Heever et al. 2011; Tao et al. 2012; Saleeby et al. 2015). As these findings are not overly novel, they will not be discussed further in this study.

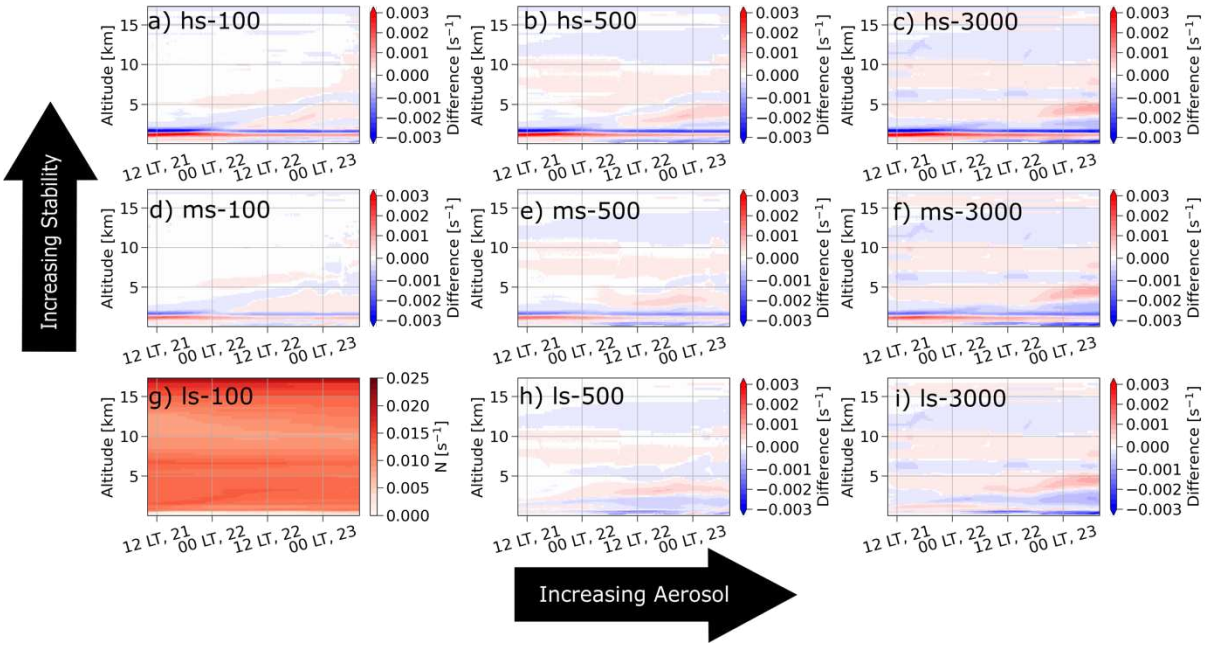

Figure 2.4: Time-height series plots of (g) static stability (quantified as *N*, the Brunt-Vaisala frequency) for the control ls-100 simulation and (a-f,h-i) differences in total cloud fraction of the aerosol and static stability sensitivity experiments from the control ls-100 simulation. Differences from control less than +/- 0.0001 s^{-1} are indicated in white in panels (a-f,h-i). Aerosol concentrations increase from left to right, and static stability increases from the bottom row to the top row as indicated by the solid black arrows.

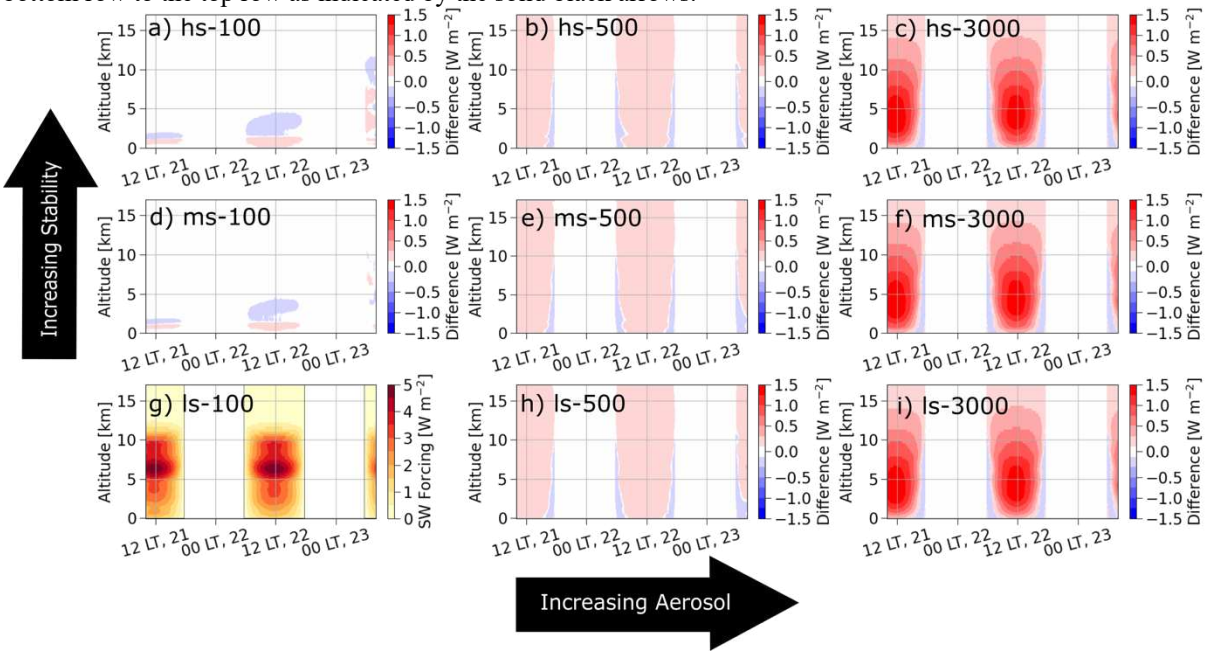

Figure 2.5: The same as Figure 2.4, but for all-sky shortwave (SW) radiative forcing. Differences from control less than +/- 0.01 W m^{-2} are indicated in white in panels (a-f,h-i).

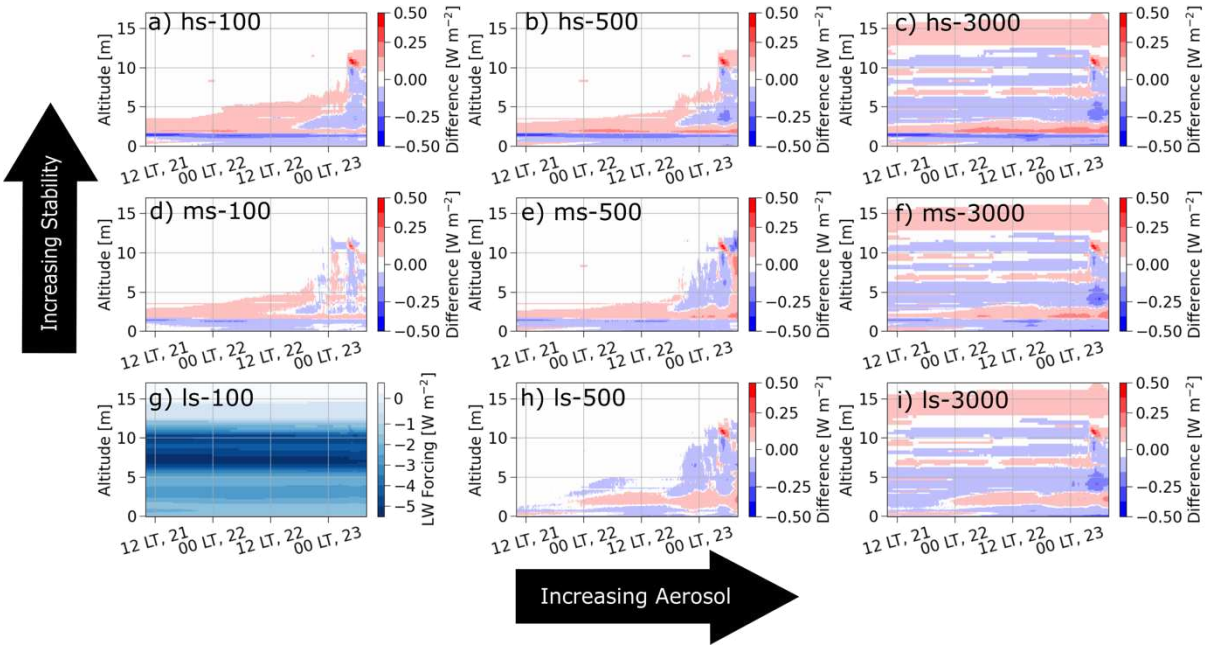

Figure 2.6: The same as Figures 2.4-2.5, but for all-sky longwave (LW) radiative forcing. Differences from control less than +/- 0.01 W m^{-2} are indicated in white in panels (a-f,h-i).

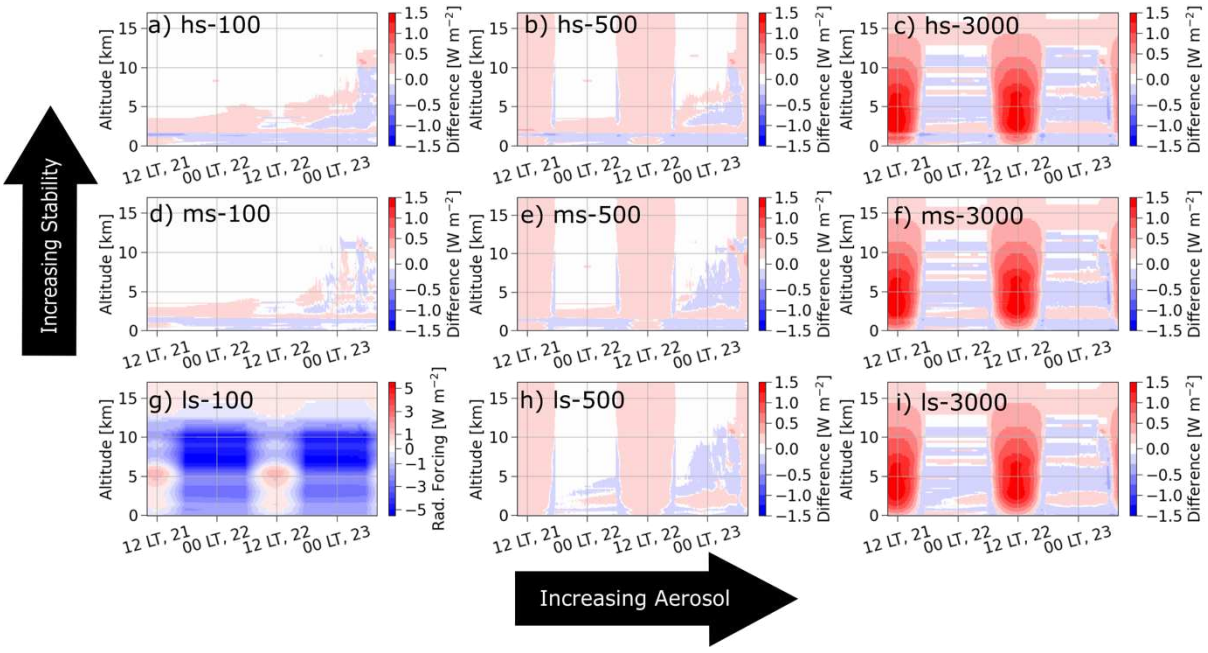

Figure 2.7: The same as Figures 2.4-2.6, but for all-sky total radiative forcing. Differences from control less than +/- 0.01 W m^{-2} are indicated in white in panels (a-f,h-i).

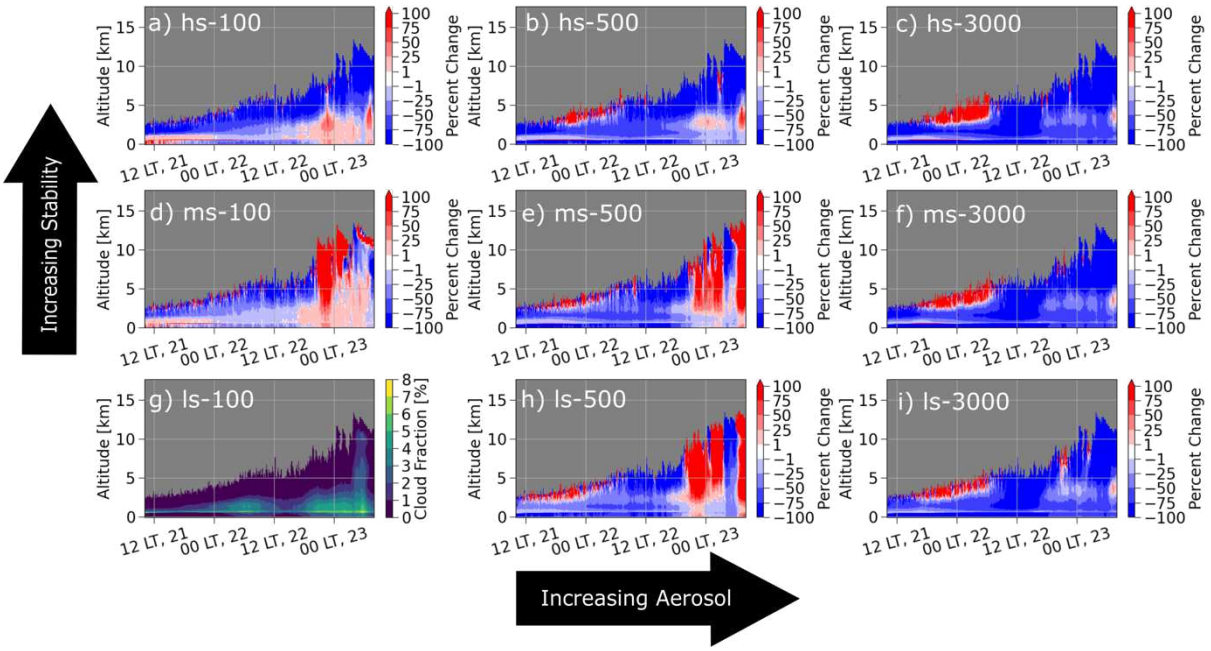

Figure 2.8: The same as Figures 2.4-2.7, but for cloud fraction. Note that unlike Figures 2.4-2.7, the difference plots show percent changes rather than the actual difference in values. Time-altitude pairings where either one (g) or both (all other panels) simulations had a cloud fraction of zero were masked in gray. Percent changes with a magnitude less than 1% are marked in white.

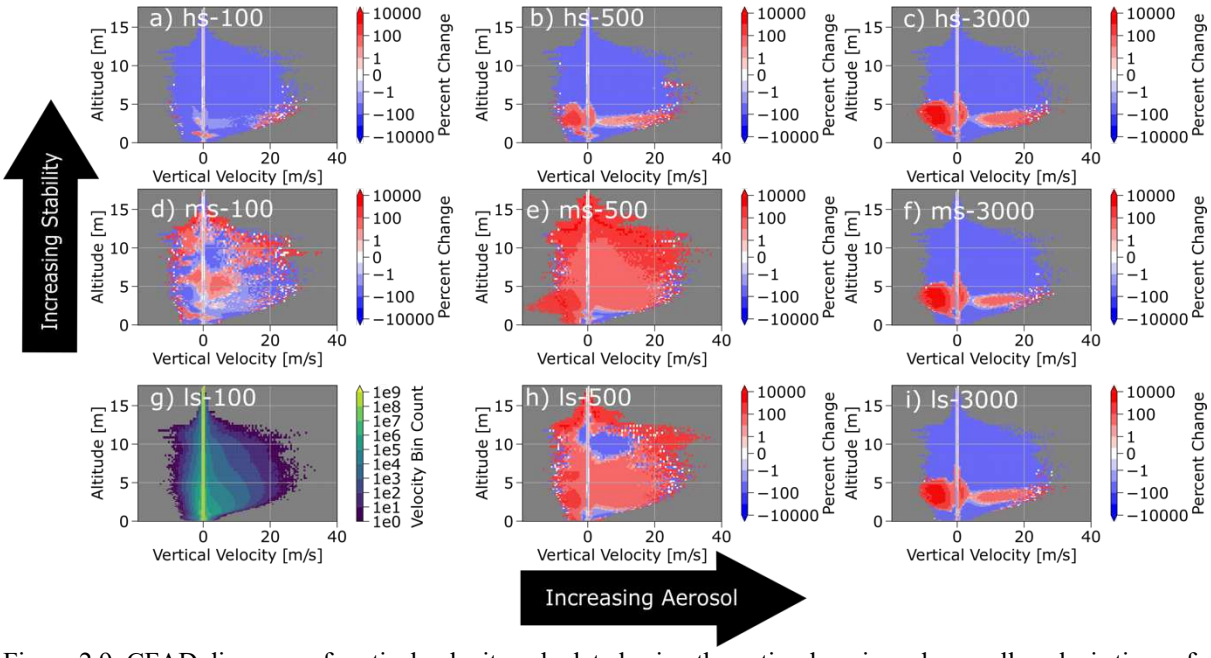

Figure 2.9: CFAD diagrams of vertical velocity calculated using the entire domain and over all analysis times, for (g) the control ls-100 simulation and (a-f,h-i) percent changes in bin count from the ls-100 simulation. Regions where either one (g) or both (all other panels) simulations had a CFAD bin count of zero were masked in gray, and percent changes less than +/- 0.1% are indicated in white in panels (a-f,h-i). Aerosol concentrations increase from left to right, and static stability increases from the bottom row to the top row as indicated by the solid black arrows. Note that the colorbars here are logarithmically scaled.

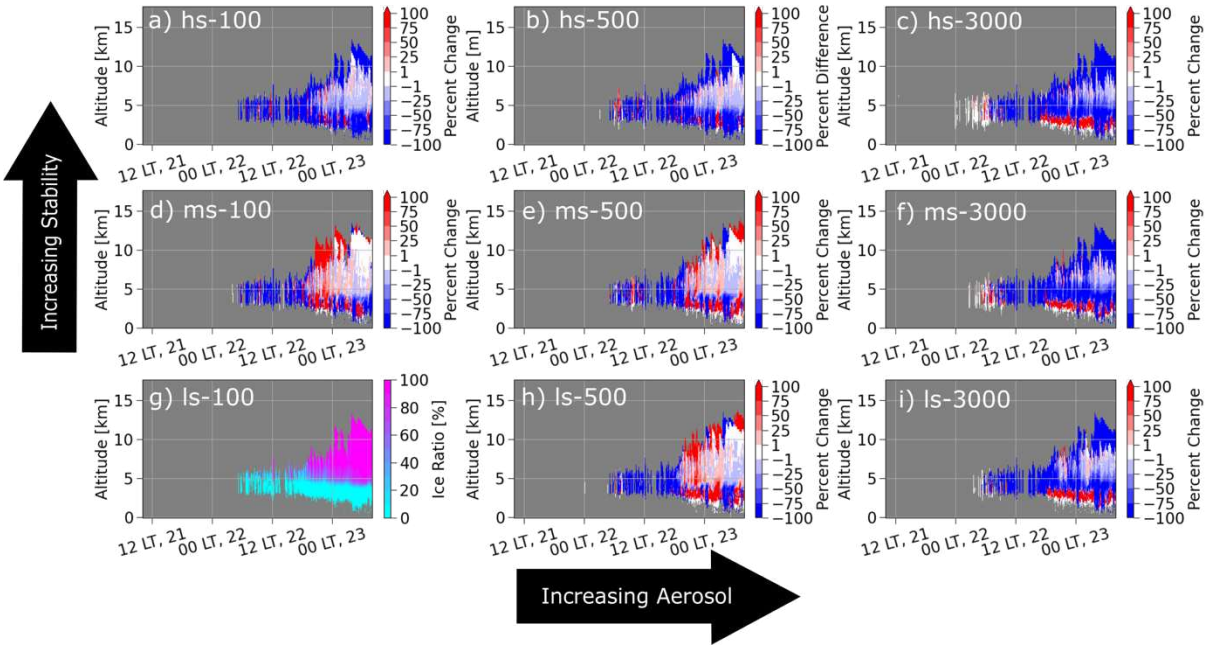

Figure 2.10: The same as Figure 2.8, but for ice ratio (mean ice condensate mixing ratio/mean total condensate mixing ratio for each vertical level and time). For the difference plots, regions where the mean condensate mixing ratio was less than 0.01 g/kg were masked, areas where the control had no cloud were provided with the ice ratio of the simulation being compared, and percent changes less than +/- 1% were indicated in white in panels (a-f,h-i).

First, we examine the changes in environmental static stability. The Gaussian temperature perturbation for the ls-100 run produces a Brünt-Väisälä frequency profile with two low-level maxima at initialization, the stronger at ~700 m (coinciding with the stability peaks in our *ms* and *hs* runs) and the weaker around 1400 m, with the *ms* and *hs* runs exhibiting a single maximum at 700 m (Fig. 2.3). Two hours after initialization, a weak unstable surface layer develops due to our initial air-sea temperature difference of about 1 K (similar to that seen in the basin-scale run) that, while persistent, does not robustly grow in either depth or strength (Fig. 2.4g) and would likely not occur if the sea surface was coupled with the atmosphere and allowed to freely evolve. Qualitatively, the vertical locations of our initially perturbed stability maxima and minima narrow but otherwise vary little over the simulation, and the boundary layer gradually destabilizes in time (more so close to the surface) due to clear-sky nocturnal longwave (LW) cooling driven by our moisture profile in conjunction with our fixed SST (Fig. 2.5, 2.6).

Due to low cloud fraction (which is in keeping with the CAMP^{2}Ex observations, e.g. Fig 2.3d,h), this clear-sky LW cooling, driven by the moisture profile, dominates the domain-wide LW signal. As the temporal frequency of radiation updates (5 min) is coarser than our dynamical timestep (0.75 s) and the cloud fraction is low (Figs. 2.2, 2.8g), cloud impacts on radiative transfer beyond their bulk moisture transport are relatively small and uncertain versus the clear-sky changes. The contrast in update frequency may also impact changes in cloud cover and precipitation, as has been identified in previous studies (e.g. Matsui et al. 2018).

Aerosols also impact the stability evolution of the environment via changes to clear-air radiative transfer. The slight vertical stratification of aerosol has little effect on stability for the low- and mid-aerosol runs (Fig. 2.4, left and center columns), but leads to stability stratification at high aerosol (Fig. 2.4, right column). Though multiple scattering in the vertical is seen to enhance daytime shortwave (SW) heating (Figs. 2.6-2.7, center and right columns), this affects stability little in comparison to the changes in the LW profile from absorption by the mixed ammonium sulfate/dust aerosols (Figs. 2.5, 2.7). In this version of RAMS, these aerosols were comprised of an ammonium sulfate coating over a dust core, with a 10% / 90% composition split, respectively, leading to greater absorption by our aerosols than pure ammonium sulfate. Stability and AIE impacts on clouds (discussed more in the following section) and ensuing changes in moisture transport also feed back on stability in the lower troposphere, though these are weaker than the initial stability perturbations (Figs. 2.3 and 2.4).

We now examine the simulation evolution in terms of cloud fraction (Fig. 2.8). Shallow boundary layer clouds are ubiquitous throughout the control simulation, but cover little area (ls-100; Fig. 2.8g). Thus, cloud coverage at any altitude remains low overall as is seen in some of the CAMP^{2}Ex observations, rarely exceeding 5% anywhere within the domain (Figs. 2.2; 2.3d,h;

2.8g). Clouds remain shallow until the first overnight period (~1735-0540 LT, 21-22 August), deepening overnight due to progressive moistening of the lower troposphere by boundary layer cumulus. The first congestus are produced around 0000 LT, 22 August, and a deep convective cloud briefly appears about 12 hours later. However, due to the low frequency of deep convection, cumulus clouds dominate the scene until the second sunset (~1735 LT, 22 August). At 18 LT, 22 August, cumulonimbi with CTHs of 8 km emerge again, and subsequently deepen to 10 km at 0000 LT, 23 August and 12 km at 0300 LT. In the final hours on the morning of the third day, deep convection decays, with maximum CTH reducing from over 12.5 km before sunrise to 11 km at the simulation's end (0800 LT, 23 August).

Changes in static stability manifest the most strongly at low and moderate aerosol concentrations (Fig. 2.8, left and center columns), with the influence of stability becoming more muted as aerosol concentrations are increased (Fig. 2.8, right column). Moderate static stability (Fig. 2.8 d,e) appears to favor deeper cloud penetration when compared with the control ls-100 run, though boundary layer cloud cover is slightly reduced. However, high stability (the top row of Fig. 2.8) generally suppresses cloud coverage. This behavior is consistent with previous studies: the trade wind stable layer is often not a true inversion in the deep tropics (Ghate et al. 2016), but the stronger it is, the more it inhibits cloud growth (Malkus 1958; Malkus and Riehl 1964; Johnson et al. 1999). Overall, increasing the static stability traps more moisture in the boundary layer, which is favorable for the development of deep convection later, but too high an initial stability ultimately impedes this convective development due to the greater buoyancy required to break through the stable layer.

Responses to increased aerosol loading are similar to those for increased stability in the lower troposphere (Fig. 2.8, center and right columns). These responses arise due to two

processes: (1) enhancement of the stability above the boundary layer by aerosol LW absorption; and (2) dynamic-thermodynamic-microphysical AIEs such as warm rain suppression (e.g. Albrecht 1989; Saleeby et al. 2015). Moderate aerosol loading leads to some enhanced production of deep convection, a finding seen in previous studies (e.g.(Khain et al. 2005; Rosenfeld et al. 2008; van den Heever et al. 2011). However, the highest amount of aerosol loading does produce consistent trends of reduced cloud cover, likely due to increased entrainment and evaporation of the smaller cloud droplets produced from greater aerosol concentrations. This indicates a reduced sensitivity to changes in static stability for high aerosol loading.

Dynamical intensity, quantified by updraft and downdraft velocities domain-wide throughout the simulation (Fig. 2.9g, note the logarithmic scale) exhibits a broad range in strengths, although most vertical velocities are weak – an expected result considering that cloud fractions are low and the CFADs include both clear and cloudy regions. The frequency of updrafts and downdrafts tends to decrease in both directions the further they are from 0 m/s, with most falling between about -10 and 30 m/s. The distribution width also varies little throughout much of the profile, though narrowing occurs above 12 km (a height that few clouds penetrate) and within the boundary layer (where static stabilities are the highest). Similar responses to cloud fraction for enhanced stability and aerosol are seen in the dynamical intensity: moderate aerosol increases result in increased dynamical intensity (Table 2.3; Fig 2.9d,e,h), with strong enhancements in either stability or aerosol suppressing it (Table 2.3; Fig 2.9, top row and right column). The only exception is for low-level vertical velocities, which are enhanced at high aerosol loading due to warm-phase invigoration. These changes, which are discretized by simulation initial characteristics, tropospheric altitude, and strength of vertical motion in Table

2.3, are reflective of the changes seen in cloud fraction, further illustrating the connections between vertical circulations and cloud field characteristics.

Table 2.3: A discretization of percent changes in vertical velocities from the control simulation (ls-100) for the other 8 model runs, categorized by vertical location, simulation initial characteristics, and strength of updraft/downdraft. Low-levels range from 0-4 km (corresponding to the possible CTH range of the cumulus mode), Mid-levels from 4-7 km (corresponding to the CTH range of the congestus mode), and Upper-levels from 7 km up (corresponding to the CTH range of the cumulonimbus mode). "Weak" updrafts and downdrafts refer to those with a magnitude between 0-1 m/s, "Moderate" between 1-5 m/s, "Strong" from 5-10 m/s, and "Very Strong" greater than 10 m/s.

Differences from ls-100 run		Weak Updrafts	Weak Downdrafts	Moderate Updrafts	Moderate Downdrafts	Strong Updrafts	Strong Downdrafts	Very Strong Updrafts	Very Strong Downdrafts
hs-100	Low levels	-0.61%	- 2.58%	- 20.8%	- 33.4%	- 24.7%	- 59.3%	- 2.63%	- 100%
	Mid-levels	-14.9%	- 16.0%	- 53.6%	- 38.9%	- 60.6%	- 67.7%	- 59.1%	- 75.0%
	Upper-levels	-45.3%	- 46.2%	- 95.4%	- 98.0%	- 98.0%	- 98.1%	- 97.1%	- 100%
hs-500	Low-levels	+ 7.43%	- 0.03%	- 22.0%	+ 46.4%	- 20.6%	+ 49.5%	+ 13.7%	0%
	Mid-levels	-9.57%	- 13.5%	- 57.5%	- 24.8%	-67.4%	- 40.0%	- 62.2%	- 35.0%
	Upper-levels	-44.9%	- 45.9%	- 97.4%	- 95.2%	- 97.3%	- 92.2%	- 86.7%	- 100%
hs-3000	Low-levels	+ 11.7%	- 1.61%	- 25.4%	+ 307%	- 23.2%	+ 2450%	+ 26.6%	+ 95.5%
	Mid-levels	+ 26.8%	+ 14.5%	- 46.7%	+ 59.8%	- 76.1%	+ 766%	- 69.1%	+ 50.0%
	Upper-levels	- 44.6%	- 46.0%	- 99.6%	- 98.9%	- 99.8%	- 99.4%	- 99.9%	- 100%
ms-100	Low-levels	- 0.02%	- 0.61%	- 1.52%	- 7.07%	- 7.44%	+ 19.5%	- 7.34%	- 75.0%
	Mid-levels	+ 2.81%	+ 3.88%	+ 8.77%	+ 1.77%	+ 6.43%	- 11.2%	- 20.0%	- 16.7%
	Upper-levels	- 3.99%	+ 6.28%	+ 25.0%	+ 44.7%	+ 17.7%	+ 35.8%	+ 31.2%	- 19.2%
ms-500	Low-levels	+ 9.60%	+ 3.76%	+ 2.62%	+ 111%	+ 2.16%	+ 412%	+ 38.2%	+ 100%
	Mid-levels	+ 29.3%	+ 29.8%	+ 45.2%	+ 68.2%	+ 41.3%	+ 105%	+ 51.0%	+ 45.7%
	Upper-levels	+ 146%	+ 455%	+ 329%	+ 458%	+ 197%	+ 268%	+ 237%	+ 44.1%
ms-3000	Low-levels	+ 13.2%	+ 0.36%	- 21.6%	+ 305%	- 19.2%	+ 2480%	+ 5.95%	+ 107%
	Mid-levels	+ 34.6%	+ 21.6%	- 41.6%	+ 70.5%	- 73.1%	+ 723%	- 71.9%	+ 21.4%
	Upper-levels	- 42.9%	- 44.1%	- 99.3%	- 97.9%	- 99.6%	- 99.3%	- 99.8%	- 100%
ls-500	Low-levels	+ 10.3%	+ 5.04%	+ 17.8%	+ 116%	+ 10.8%	+ 155%	+ 51.7%	- 100%
	Mid-levels	+ 30.2	+ 31.7%	+ 55.6%	+ 79.4%	+ 46.3%	+ 92.8%	+ 46.5%	+ 33.3%
	Upper-levels	+ 47.0%	+ 142%	+ 122%	+ 272%	+ 38.9%	+ 152%	+ 94.7%	+ 5.56%
ls-3000	Low-levels	+ 14.7%	+ 2.23%	- 17.6%	+ 322%	- 13.0%	+ 2540%	+ 16.7%	+ 103%
	Mid-levels	+ 39.3%	+ 26.9%	- 36.3%	+ 80.2%	- 66.8%	+ 709%	- 56.8%	+ 29.4%
	Upper-levels	- 42.2%	- 43.5%	- 98.7%	- 95.7%	- 99.1%	- 96.3%	- 98.7%	- 100%

Finally, the relative contribution of ice to the total condensate illuminates some stark changes over the course of the simulation (Fig. 2.10g). As the 0 ºC level is located at ~4.5-5 km in each simulation, the vast majority of condensate below this altitude is liquid. Ice first emerges in the domain around 6 LT, 22 August, when some congestus clouds glaciate. As the congestus are primarily liquid, the ice ratios generally remain low until deep convective clouds become more frequent around 12 hours later. After 18 LT on 22 August, we see a mixed-phase region from roughly 4.5 – 6 km, near-total glaciation above 9 km, and pulses of elevated and reduced ice ratios above and below the freezing level. These regions of greater and lesser ice ratios in the mixed-phase region indicate falling ice precipitation and lofted supercooled water, respectively. Ice phase responses to enhancements in static stability and aerosol further reinforce and explain the changes seen in cloud fraction and dynamical intensity. At moderate stability and aerosol loading, we see a delayed onset of glaciation but later increases in both deep glaciated clouds and sub-freezing level ice precipitation (Fig 2.10 d,e,h), indicating the importance of glaciation and the timing of these ice processes for cold-phase invigoration of deep convection. As previously discussed, high static stability impedes the vertical growth of shallower convection, which subsequently suppresses glaciation. Additionally, while moderate amounts of aerosol induce both warm and cold phase invigoration, high aerosol loading only produces the former, resulting in lower cloud tops, cloud coverage, and glaciation. This robust warm phase invigoration, and more mixed response in the cold phase with suppression at the highest aerosol loading, are in agreement with the findings of recent studies of deep convection ((Igel and van den Heever 2021; Marinescu et al. 2021; Park and van den Heever 2021).

Generally, our simulations initiate as a shallow cumulus field that gradually deepens and dynamically intensifies as diurnal cycles of convection and radiation progressively moisten the

lower troposphere and destabilize the middle and upper troposphere. The initiation of deeper convection further impacts the evolution of the domain by deepening the vertical transport of moisture and producing considerably more precipitation, although cloud cover remains low overall. Since our idealized simulations lack the presence of SST variations, SST feedbacks and large-scale wind disturbances that some studies have identified to be important to the diurnal cycle (e.g. (Weller and Anderson 1996; Sui et al. 1997; Ruppert and Johnson 2015), some of this variability cannot be fully captured. However, the overall diurnal cycle and our understanding of the role of convective moistening are reasonably consistent with previous studies using a fixed SST (e.g. Liu and Moncrieff 1998). Increasing the static stability and aerosol both impact the thermodynamic evolution of the scene, with moderate (strong) enhancements in either of the two amplifying (suppressing) convective favorability. Lastly, it appears that impacts from changing both stability and aerosol may operate synergistically to invigorate convection (a "Goldilocks Zone") in some circumstances. This is most evident in the ms-500 simulation, which exhibits deeper convection, more widespread updraft and downdraft invigoration, and more vertically contiguous fluctuations of enhanced and reduced ice ratio (i.e., more lofting of supercooled water and precipitation of ice) than the control run. Stability-induced enhancement of boundary layer moisture coupled with greater condensational growth due to higher aerosol concentrations is a prime driver of this response.

Having examined these responses to aerosol and static stability, we now turn our attention to examining the response of each convective mode to these initial conditions. While shallow convection can and does grow upscale to deep convection in our simulations, considering each mode and its responses to aerosol and stability in relative isolation is important

for understanding the role each mode plays in the evolution of the bulk environment, cloud and precipitation processes themselves, and radiative transfer.

2.3.2) The Response of Cloud Mode Properties to Static Stability and Aerosol

Cloud mode characteristics were obtained by saving all grid points classified as a particular convective mode at all analysis times, and then calculating statistics, mean profiles, and net profiles over all the times when at least one cloud of a particular mode (categorized as discussed in Section 2b) was present. The cloud properties in Figures 2.11-2.14 are separated by mode, with the top row showing the control (ls-100) profiles for cumulus (panel a), congestus (b) and cumulonimbus (c), and the bottom row (d-f) showing the simulation differences from the control for each mode, respectively. Note that each column's vertical axis differs – cumulus extend to 4 km, congestus to 7 km, and cumulonimbus to about 14 km – and also recall the presence of background stable layers at ~ 1 km (boundary layer), ~ 6.5 km (freezing level), and ~16 km (tropopause).

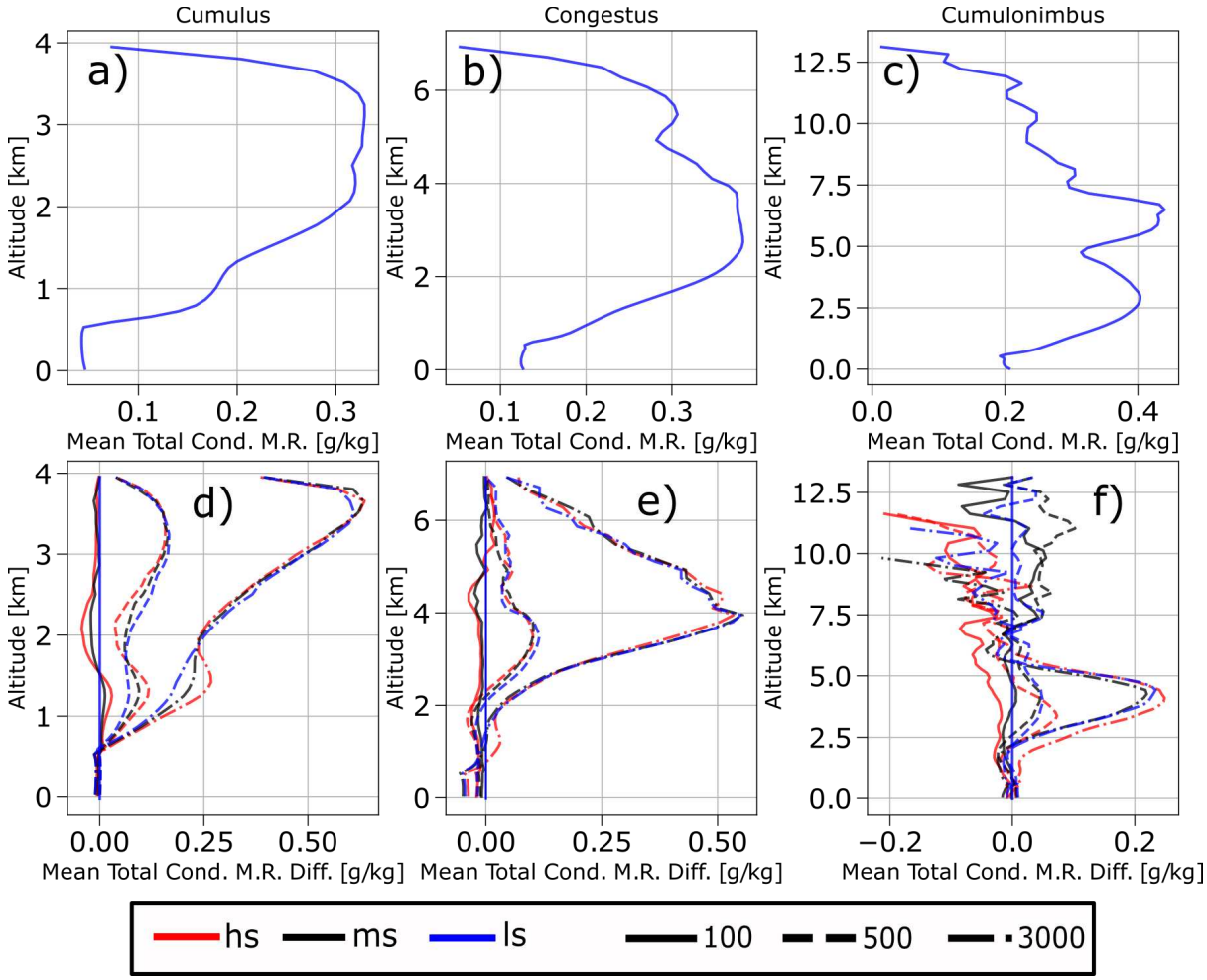

Figure 2.11: Profiles of mean total condensate mixing ratio ("Total Cond. M.R.") for the (a) cumulus, (b) congestus, and (c) cumulonimbus modes for the ls-100 control simulation, and differences from control for the other sensitivity experiments for the (d) cumulus, (e) congestus, and (f) cumulonimbus modes. Note that each column's vertical axis differs – cumulus extend to 4 km, congestus to 7 km, and cumulonimbus to about 14 km.

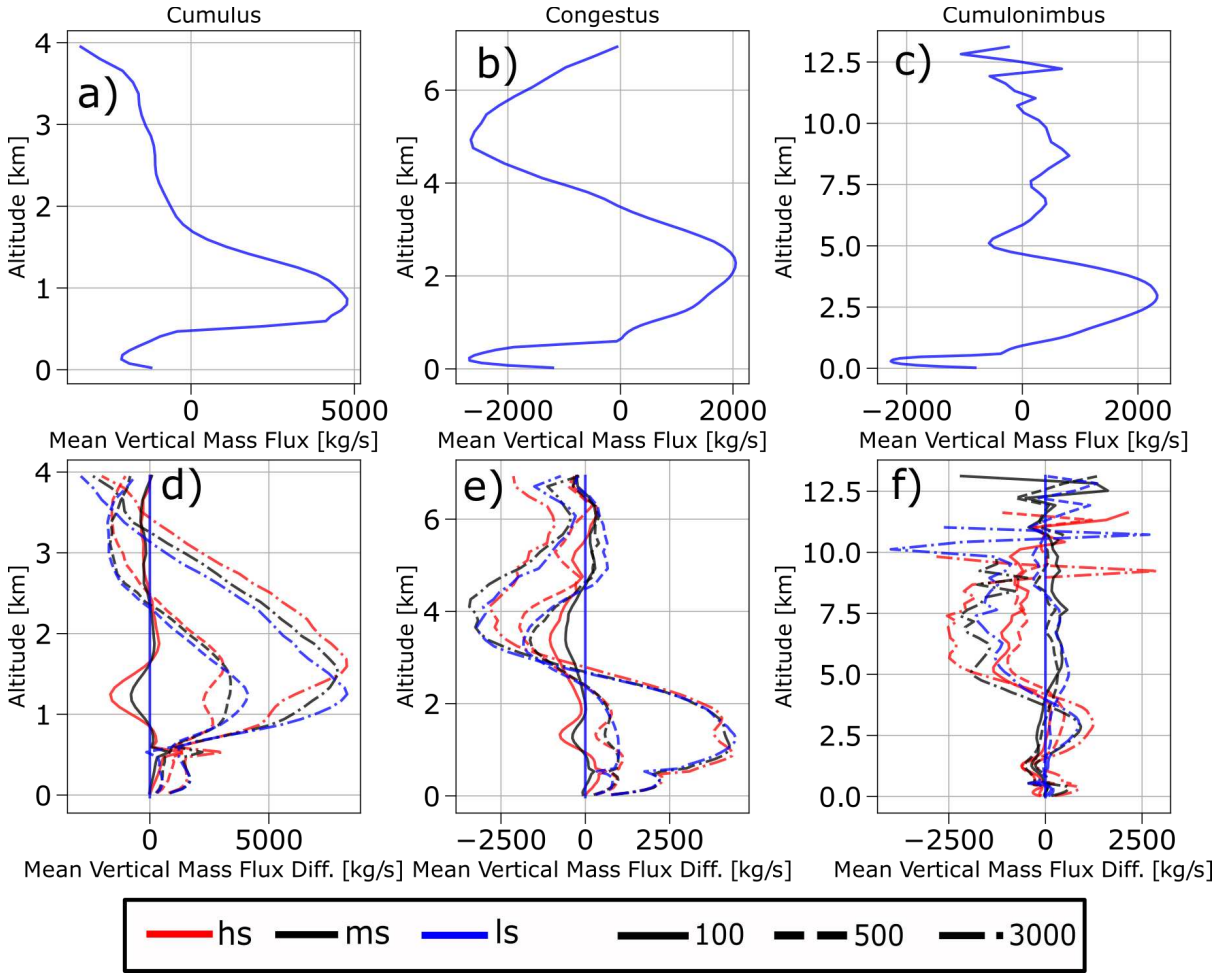

Figure 2.12: Profiles of mean vertical mass flux. Each panel of the plot represents the same simulation(s) and cloud species as its counterpart in Figure 2.11. Note that each column's vertical axis differs – cumulus extend to 4 km, congestus to 7 km, and cumulonimbus to about 14 km.

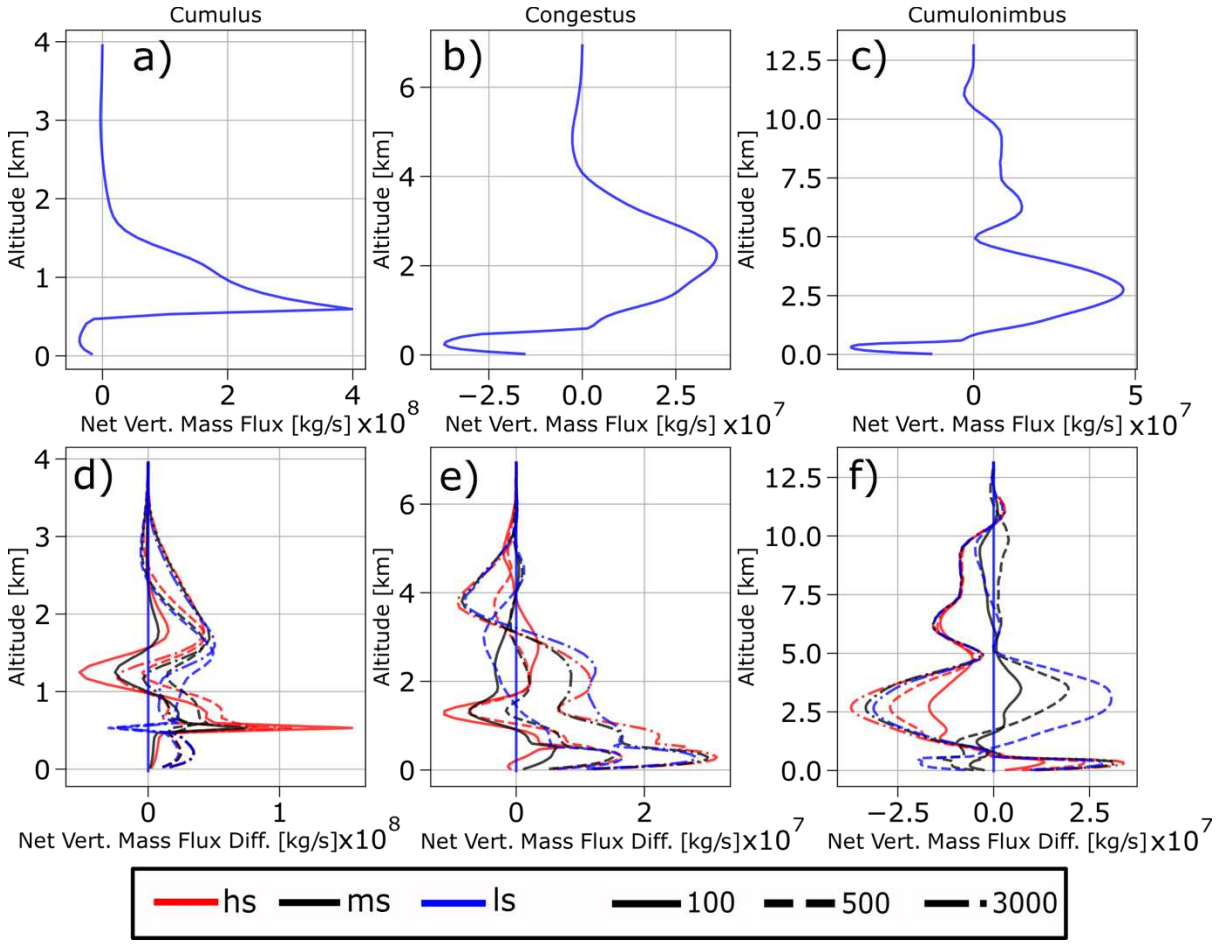

Figure 2.13: Profiles of net vertical mass flux. Each panel of the plot represents the same simulation(s) and cloud species as its counterpart in Figures 2.11 and 2.12. Note that the x-axis units for panels (a) and (d) are in 1e8 kg s^{-1}, while the remainder are in 1e7 kg s^{-1}. Note that each column's vertical axis differs – cumulus extend to 4 km, congestus to 7 km, and cumulonimbus to about 14 km.

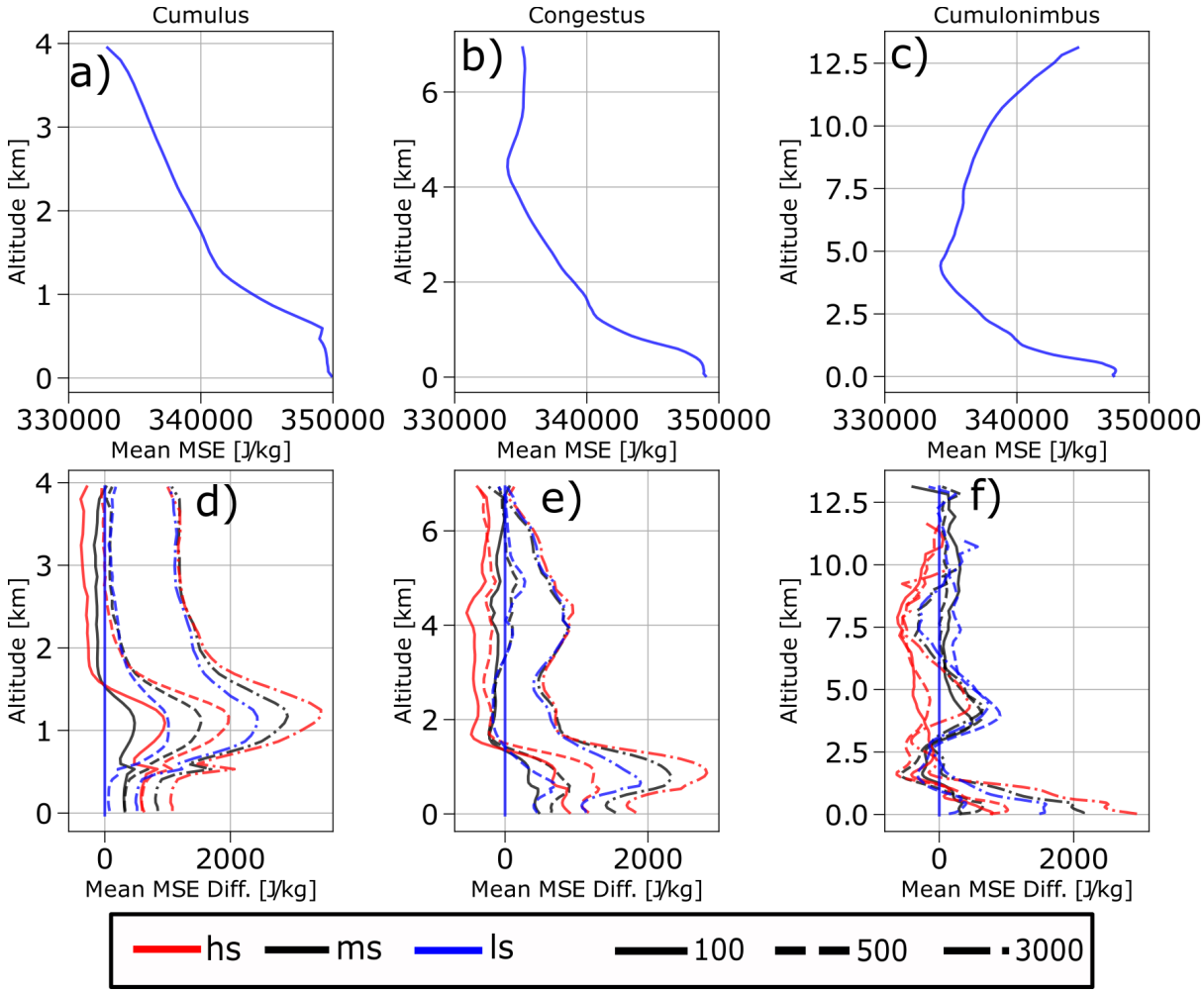

Figure 2.14: Profiles of mean MSE. Each panel of the plot represents the same simulation(s) and cloud species as its counterpart in Figures 2.11-2.13. Note that each column's vertical axis differs – cumulus extend to 4 km, congestus to 7 km, and cumulonimbus to about 14 km.

Cumulus clouds are small, dynamically weak, and numerous in the ls-100 simulation (Table 2.4). The average cumulus cloud precipitates weakly, if at all, resulting in a low condensate mixing ratio below 500 m in the mean and a sharp increase above this height (Fig. 2.11a). Cumulus deeper than the mean CTH exhibit heavier condensate loading between 2-3.5 km that then drops off sharply just below the 4 km cutoff. The mean vertical mass flux is negative below 500 m indicating precipitation and/or sedimentation, is positive from 500 – 1500 m, and increasingly negative above 1500 m (Fig. 2.12a). When aggregated to consider the net vertical mass transport by the cumulus mode, there is a strongly positive net flux between 500-

1500 m, with considerably weaker negative fluxes above and below this level (Fig. 2.13a), indicating that cumulus primarily act to transport mass, moisture, heat, and aerosol upwards within the boundary layer, as noted in previous studies (e.g. Johnson et al. 1999; Schumacher et al. 2004). The mean moist static energy (MSE) contained within the cumulus mode is highest at the surface, with an additional local maximum just above 500 m (Fig. 2.14a). The mean MSE decreases sharply from 500 to about 1200 m, where environmental static stability is the lowest and entrainment may reduce MSE. Above 1200 m, this reduction is slower and more even.

Table 2.4: Some key characteristics (cloud top height (m), maximum vertical velocity [w Max; m/s], maximum areal coverage (km^2), single-timestep mean count, and total count) of clouds which were classified as cumulus in each simulation. For each pair of values, the leftmost number is the arithmetic mean, and the rightmost number following the +/- is the standard deviation. All clouds identified as cumulus between 0200 Z on 21 August (2 hours after initialization) and 0000 Z on 23 August were included in this analysis.

	CTH [m]	w Max [m/s]	Max Area [km^2]	Mean Count [#]	Total Count [#]
hs-100	958.01 +/- 541.41	1.574 +/- 1.917	0.1994 +/- 0.3006	6312.0 +/- 1559.4	3.49×10^6
hs-500	941.36 +/- 522.02	1.497 +/- 1.918	0.1662 +/- 0.2399	6591.3 +/- 1215.9	3.64×10^6
hs-3000	871.55 +/- 456.46	1.329 +/- 1.811	0.1497 +/- 0.1840	6227.3 +/- 899.54	3.44×10^6
ms-100	964.84 +/- 542.02	1.576 +/- 1.951	0.2002 +/- 0.3151	6027.2 +/- 1559.7	3.33×10^6
ms-500	952.25 +/- 524.32	1.502 +/- 1.944	0.1637 +/- 0.2401	6414.7 +/- 1376.4	3.55×10^6
ms-3000	895.68 +/- 471.90	1.364 +/- 1.851	0.1458 +/- 0.1763	6435.7 +/- 826.93	3.56×10^6
ls-100	971.20 +/- 541.78	1.579 +/- 1.988	0.2024 +/- 0.3393	5703.0 +/- 1558.6	3.15×10^6
ls-500	971.22 +/- 540.38	1.522 +/- 1.989	0.1637 +/- 0.2489	6211.7 +/- 1542.7	3.44×10^6
ls-3000	916.71 +/- 485.94	1.385 +/- 1.885	0.1425 +/- 0.1758	6464.6 +/- 919.73	3.57×10^6

When stability is increased for the same aerosol loading, the CTH and mean maximum vertical velocity of cumulus clouds are unambiguously suppressed (Table 2.4). However, stability-driven changes in mean maximum area and frequency are modulated by aerosol loading. With greater static stability, condensate loading (Fig. 2.11d) and MSE (Fig. 2.14d) are enhanced in the boundary layer and reduced above, while the opposite trends are seen in the vertical mass fluxes (Fig. 2.12-2.13d). Enhanced low-level static stability reduces the ability of cumulus to penetrate beyond the trade wind stable layer, which increases condensate loading and moisture within the boundary layer. This reinforces our discussion in Section 3a regarding the impact of the strength of the trade wind stable layer on vertical cloud growth.

Increasing aerosol loading reduces the CTH, maximum vertical velocity, and maximum area of the cumulus mode (Table 2.4), in agreement with some previous studies (Xue et al. 2008). Despite this, there are some signs of warm-phase enhancement: greater condensate loading (Fig. 2.11d) that agrees with the 2nd AIE (Albrecht 1989), greater MSE (Fig. 2.14d), and deeper positive mean mass flux (Fig. 2.12d). However, negative mean mass flux values higher in the column are enhanced for increased aerosol concentrations, and there is also reduced net vertical mass flux in parts of the boundary layer (Fig. 2.13d). Increasing condensate loading to the point of weighing down cumulus updrafts, as well as an enhancement of stability and stratification above the boundary layer, contribute to these aerosol responses.

While the middle mode of congestus is about 2 orders of magnitude less frequent than the cumulus mode in our simulations, these clouds are much wider, taller, and more dynamically vigorous clouds. Their key statistics are presented in Table 2.5. Observational studies on tropical oceanic congestus are limited and definitions vary, so contextualizing these values is challenging – for example, previously defined CTH varies from as wide as 3-9 km (e.g. Luo et al. 2009) to as

narrow as 5-7 km (e.g. Cotton et al. 2011). Our values fit reasonably well within those reported by previous observational studies, albeit on the shallower and narrower side (e.g. Cotton et al. 2011). Congestus clouds have greater condensate relative to cumulus, particularly in the lowest 500 m due to precipitating more frequently and heavily (Fig. 2.11b). A local maximum in condensate occurs between 2.5-4 km from warm and cold rain production, while another local maximum at 5.5 km (0.5-1 km above the freezing level) indicates boosts from ice production and lofted cloud water. Both maxima exhibit contributions from ice and cold rain production in transient congestus, which remain buoyant at the freezing level and continue growing (Luo et al. 2009; Leung and van den Heever 2022). The local minimum at 4.5-5 km is indicative of lower condensate loading near cloud top in terminal congestus (also identified by Luo et al.), which are negatively buoyant at the freezing level, as well as enhanced freezing level detrainment (Zuidema 1998; Posselt et al. 2008). Some of these changes are reflected in the mean vertical mass flux profile, such as a stronger negative mean flux below 500 m (Fig. 2.12b). The region of positive mean flux is deeper than the cumulus mode (extending from ~500 – 3500 m), though its maximum value is about half as large, and the minimum around 4.75 km (near the freezing level) is roughly the maximum altitude terminal congestus would reach. The net vertical mass flux reflects similar patterns to the mean flux, further illuminating that most of the congestus mass transport occurs below ~3.5 km (Fig. 2.13b). However, the congestus net flux is about an order of magnitude less than for the cumulus mode, meaning that far less moisture is lofted to the mid-levels via congestus than occurs within the lower levels due to cumulus transport. Finally, the congestus mean MSE profile in the low levels appears similar to that of cumulus but has a minimum around 4.5 km indicative of terminal congestus and an increase above this altitude from glaciation-related boosts to MSE from transient congestus (Fig. 2.14b).

Congestus exhibits two distinct behavioral regimes due to its more varied dependencies on the environment, which makes isolating individual responses to aerosol or static stability more challenging. To first order, greater static stability results in narrower and more frequent congestus, but neither maximum vertical velocity nor CTH respond monotonically (Table 2.5). Stability impacts above the boundary layer are primarily modulated by aerosol, but higher stability also results in reduced precipitation. This can be seen through lower total condensate (Fig. 2.11e) and less-negative vertical mass fluxes (Fig. 2.12e, 2.13e) below 500 m, which subsequently increase congestus MSE within the boundary layer (Fig. 2.14e). On the other hand, first-order results from increasing aerosol concentrations are congestus that are shallower and narrower, but also more frequent in occurrence and dynamically vigorous (Table 2.5). Like enhanced stability, greater aerosol loading reduces precipitation (Fig. 2.11-2.13 e). However, condensate loading is enhanced above 500 m and the mean vertical mass flux (Fig. 2.12e) is boosted below the freezing level with greater aerosol loading, both of which indicate warm-phase invigoration as identified by previous studies (e.g. Li et al. 2013; Sheffield et al. 2015).

Table 2.5: The same as Table 2.4, but for those clouds classified as congestus.

	CTH [m]	w Max [m/s]	Max Area [km^2]	Mean Count [#]	Total Count [#]
hs-100	4802.9 +/- 739.00	11.48 +/- 4.123	6.517 +/- 6.772	32.991 +/- 33.280	1.13×10^4
hs-500	4758.3 +/- 699.08	12.02 +/- 4.039	5.225 +/- 4.937	32.689 +/- 35.680	1.26×10^4
hs-3000	4730.7 +/- 637.77	13.12 +/- 4.090	4.044 +/- 4.017	29.331 +/- 26.945	1.10×10^4
ms-100	4800.4 +/- 730.22	11.49 +/- 4.025	7.109 +/- 7.754	25.763 +/- 21.014	9.22×10^3
ms-500	4826.8 +/- 758.73	12.23 +/- 4.051	6.286 +/- 6.645	26.057 +/- 25.105	9.64×10^3
ms-3000	4720.8 +/- 633.72	12.89 +/- 4.035	4.120 +/- 4.557	28.647 +/- 28.587	1.10×10^4
ls-100	4795.2 +/- 717.68	11.58 +/- 4.050	7.892 +/- 9.145	25.401 +/- 14.704	9.20×10^3
ls-500	4783.2 +/- 747.98	12.10 +/- 4.037	6.323 +/- 7.141	22.461 +/- 21.241	8.33×10^3
ls-3000	4736.1 +/- 652.03	12.86 +/- 4.036	4.387 +/- 4.810	29.825 +/- 28.118	1.09×10^4

Above the freezing level, some of the synergies discussed regarding the "Goldilocks Zone" in Section 3a manifest in congestus. While high aerosol loading substantially reduces mass fluxes above 4 km (Fig. 2.12e, 2.13e), moderate aerosol loading coupled with low-to-moderate boundary layer static stability appears to be the most favorable environment for more expansive and vigorous congestus. The increased stability acts to enhance boundary layer moisture and energy. Coupled with the warm-phase invigoration from moderate aerosol loading, this allows developing congestus to draw on the enhanced MSE enough to invigorate its updraft and boost condensate loading, without too much condensate loading, entrainment, and evaporation weakening the updrafts.

Cumulonimbus are highly infrequent compared with the cumulus and congestus modes (Table 2.6), and only manifest once sufficient environmental moistening by cumulus and congestus has occurred. Tropical oceanic deep convection can reach the tropical tropopause in nature (Johnson et al. 1999), though our cumulonimbi are considerably shallower (Table 2.6) due to the high environmental wind shear (Igel and van den Heever 2015) and sharp drop in moisture above 10 km, in keeping with observations. The mean maximum vertical velocity also agrees well with that reported by Heymsfield et al. (2010). Cumulonimbus precipitate heavily, exhibiting much greater mean condensate loading in the lowest 500 m than either cumulus or congestus, as well as greater mean condensate loading overall (Fig. 2.11c). The condensate loading profile also reveals greater maxima above and below the freezing level than congestus, indicating greater ice and cold rain production, and a less-prominent freezing level local minimum that is typically associated with greater freezing level stability and detrainment (e.g. Posselt et al. 2008). The mean vertical mass flux of the cumulonimbus mode has deeper positive transport (~1-4.5 km) and weaker near-surface and freezing level negative mean fluxes than the

congestus mode, as well as positive mean flux from ~6-10 km (Fig. 2.12c). The net vertical mass flux is of the same magnitude as that for congestus but produces greater positive net flux in the low levels, and a positive net flux from ~1 km through the freezing level all the way up to ~10 km (Fig. 2.13c), exhibiting deep mass, moisture, and heat transport past the freezing level by cumulonimbus as characterized by Schumacher et al. (2004). Lastly, the mean MSE profile for cumulonimbus largely mirrors that of cumulus and congestus for the lower levels but increases more steadily above 4.5 km (except for a relatively static layer around 7 km) and reaches a maximum nearing that of the surface value at the top of the profile (Fig. 2.14c), further indicating deep transport of near-surface MSE.

Table 2.6: The same as Tables 2.4 and 2.5, but for those clouds classified as cumulonimbus.

	CTH [m]	w Max [m/s]	Max Area [km^2]	Mean Count [#]	Total Count [#]
hs-100	7795.2 +/- 853.65	16.65 +/- 5.482	39.29 +/- 36.91	3.9909 +/- 2.6302	4.39 x 10^2
hs-500	7875.9 +/- 921.86	16.89 +/- 5.255	28.23 +/- 22.19	3.0667 +/- 1.8633	3.22 x 10^2
hs-3000	7626.7 +/- 560.35	17.75 +/- 4.941	16.71 +/- 8.296	1.8690 +/- 1.0210	1.57 x 10^2
ms-100	8719.8 +/- 1636.1	16.62 +/- 5.725	76.21 +/- 66.37	4.2550 +/- 2.3606	6.34 x 10^2
ms-500	8582.2 +/- 1504.2	17.12 +/- 5.742	62.41 +/- 76.11	6.2797 +/- 3.6992	8.98 x 10^2
ms-3000	7709.2 +/- 613.97	16.54 +/- 4.601	22.74 +/- 13.75	1.9208 +/- 1.1997	1.94 x 10^2
ls-100	8670.2 +/- 1610.2	16.45 +/- 6.657	76.80 +/- 71.32	3.8675 +/- 2.1887	5.84 x 10^2
ls-500	8806.7 +/- 1513.2	17.47 +/- 6.194	70.03 +/- 70.08	5.6225 +/- 3.2013	8.49 x 10^2
ls-3000	7759.6 +/- 661.64	17.16 +/- 4.670	22.67 +/- 13.80	2.3047 +/- 1.3951	2.95 x 10^2

The cumulonimbus mode responses to perturbations of initial stability and aerosols are even more complex and non-linear than congestus. Cumulonimbi tend to be shallower and smaller in area but more dynamically intense at high static stability and are most frequent at middling stability (Table 2.6). Signs of precipitation suppression, such as low-level mass flux changes (Figs. 2.12f, 2.13f), are not robust despite reduced condensate loading (Fig. 2.11f) and enhanced boundary layer moisture (seen through MSE changes, Fig. 2.14f). This illustrates the greater role of cold-phase precipitation in cumulonimbus versus cumulus and congestus, and the relative insensitivity of such processes to boundary layer static stability alone, despite the latter's role in the evolution of boundary layer moisture and energy. Indeed, a regime separation can be seen between the ms-100, ms-500, and ls-500 responses and those of the other runs, particularly above 4 km, further highlighting the nonlinearity present.

Regarding aerosols, moderate loading produces the deepest, strongest, and most frequent cumulonimbus, though the greatest cloud area is seen at low aerosol loadings (Table 2.6). With enhanced aerosol concentrations, condensate loading (Fig. 2.11f), mean vertical mass flux (Fig. 2.12f), and mean MSE (Fig. 2.14f) are generally enhanced from 2-6 km, 2-4 km, and 3-6 km, respectively, all of which are strong signs of warm-phase invigoration. Values above these altitudes, however, are reduced at high aerosol loading and otherwise modulated by stability, and the net vertical mass flux (Fig. 2.13f) shows a strong regime separation above 2 km. Boundary layer MSE is consistently enhanced with greater aerosol (Fig. 2.14f), but not above the freezing level due to the mixed cold-phase responses. Considered as a whole, these responses illustrate similar "Goldilocks Zone" sensitivities for cumulonimbus as we noted for congestus: the control (ls-100) environment is favorable for deep convection, and moderate increases to aerosol (ls-500, ms-500) or static stability (ms-100, ms-500) preserve or enhance convective ingredients present

in ls-100 by providing more vapor growth sites, enhanced condensate lofting (aerosol); increased boundary layer moisture and energy (stability); or some combination of these. These findings agree with several studies in the literature (e.g. Khain et al. 2005, 2008; Fan et al. 2009; Storer et al. 2010, 2014; Marinescu et al. 2021; Park and van den Heever 2022) that identify mitigating environmental factors on robust warm and cold phase invigoration from increased aerosol loading.

In summary, each of the 3 cloud modes evident in these simulations exhibit characteristics that are generally consistent with observations (e.g. Johnson et al. 1999) and the understood role that each mode plays in vertical mass, heat, and moisture transport (e.g. Schumacher et al. 2004). Their changes in response to perturbations in initial static stability and aerosol profiles are also in keeping with past literature. However, the complex modulations and interactions between different aspects of the responses to aerosol loading and static stability indicate the importance of considering mitigating factors and environmental characteristics when assessing aerosol-cloud interactions.

2.4) Conclusions and Future Work

Our primary research goal was to explore the sensitivities of the tropical trimodal convective distribution, convective environment, and upscale growth of convection to changes in static stability and aerosol loading. We considered the impacts of covarying three different initial static stabilities and three different initial aerosol profiles in a base environment representative of tropical maritime regions around the Philippines which were observed during CAMP^{2}Ex. To this end, nine different simulations were run for 48 hours of integration time using the RAMS model in an LES framework. Our analysis has shown that enhanced static stability and aerosol loading both substantially impact the evolution of a tropical, maritime environment and the associated

cloud fields around the Philippines. This work has allowed us to draw five key conclusions as summarized in Figure 2.15 and discussed as follows.

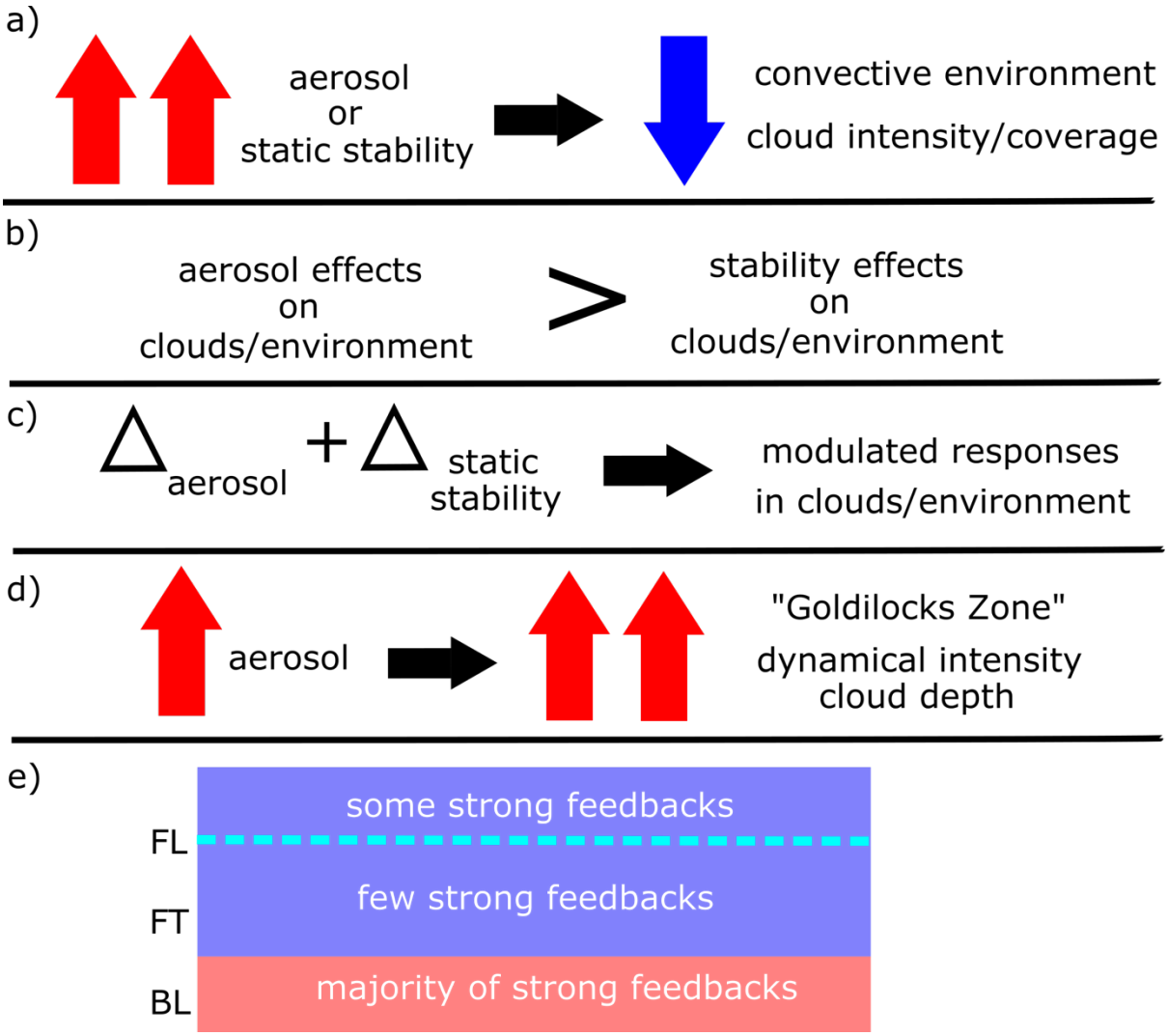

Figure 2.15: A schematic of the five key conclusions drawn from this study. These include: (a) the suppression of the bulk environment and the trimodal convective distribution from high amounts of aerosol loading and boundary layer static stability; (b) the dominance of aerosol effects over stability effects on both clouds and environment; (c) the modulation of cloud/environment responses to static stability and aerosols by changing the characteristics of both; (d) the presence of a "Goldilocks Zone" in dynamical strength and cloud depth of convective clouds due to moderate aerosol loading; and (e) the occurence of most of the strong feedbacks in the boundary layer, with some strong feedbacks seen above the freezing level but relatively few within the warm-phase free troposphere. Double upward arrows indicate high levels of the noted quantity (i.e., high stability and/or high aerosol for (a)), the deltas in (c) denote changes to the subscripted initial characteristic, the single upward arrow in (d) denotes a moderate level of aerosol, and in (5), FL, FT, and BL represent the freezing level, free troposphere, and boundary layer, respectively.

1. ***Large amounts of aerosol loading and low-level static stability suppress the bulk environment and the intensity and coverage of convective clouds (Fig. 2.15a)***

Strong static stability traps more moisture and MSE in the boundary layer but is also a substantial barrier to penetration by convective updrafts. This can be seen in the environmental characteristics (Figs. 2.4-2.10) and cloud mode statistics (Tables 2.4-2.6). Changes to LW radiation from increased low-level stability reinforce the initial perturbation structure and render the bulk environment far less dynamically (Fig. 2.9, Table 2.3) and convectively (Fig. 2.8, Tables 2.4-2.6) active versus lower-stability environments. Similarly, high aerosol loading produces warm-phase invigoration (Fig. 2.9) and increased condensate loading (Fig. 2.11), but the latter counteracts buoyancy enhancements from greater condensational heating and increased LW absorption by aerosols (Fig 2.6-2.7) further enhances environmental stability stratification (Fig 2.4). It appears that entraining cloud edges may have greater evaporative cooling owing to smaller (and subsequently easier-to-evaporate) drops than at lower aerosol loading, which is reinforced by the narrower clouds seen at high aerosol loading (Tables 2.4-2.6).

2. ***Cloud and environmental responses to aerosol loading tend to be stronger than those from static stability (Fig. 2.15b)***

The right columns of Figures 2.4-2.10 illustrate the dominance of high aerosol loading over the benefits of starting with a more convectively favorable (i.e., lower static stability) environment. Beyond the impacts already discussed in the first bullet, the LW and total radiation evolution (Figs. 2.6-2.7, right columns) are stratified at high aerosol loading due to the vertical redistribution of aerosols. This causes a more stratified static stability structure, resulting in stronger boundary layer and freezing level stable layers that inhibit vertical development of deeper convection.

3. ***The effects of aerosol and stability perturbations modulate each other substantially (Fig. 2.15c)***

This conclusion is best seen through the cloud mode statistics (Tables 2.4-2.6) and vertical profiles of condensate loading, mean and net vertical mass flux, and MSE (Figs. 2.11-2.14, respectively). The shallow cumulus mode shows a weak modulation of effects versus deeper convection, with robust trends in the cloud mode statistics (Table 2.4) and stability mostly altering the dominant effects of aerosol as a function of height in the vertical profiles (Figs. 2.11d-2.14d). However, congestus and cumulonimbus (Tables 2.5 and 2.6) exhibit less monotonic trends with stability and aerosol, indicating greater nonlinearity in the combined effects of perturbed stability and aerosol. This is more apparent above the freezing level, where profiles of congestus and especially cumulonimbus group into 2 primary regimes (Figs. 2.11-2.14 e-f).

4. The deepest convection and highest dynamical intensity occur at moderate aerosol loading, rather than at low or high loading (Fig. 2.15d)

The "Goldilocks Zone" runs of ms-100, ms-500, and ls-500 exhibit a more constructive stability-aerosol modulation of each property's impacts on condensate loading (Fig. 2.11d,e,h), mean and net vertical mass fluxes (Figs. 2.12-2.13d,e,h), and mean MSE (Fig. 2.14d,e,h) than the other runs, which exhibit consistently less condensate loading, more negative vertical mass fluxes, and less MSE than our control ls-100 run. Deep convection reaches higher maximum and mean CTH values at moderate aerosol loading (Figs. 2.8 and 2.10, center columns; Table 2.6), largely due to the enhanced ice processes and lofting of supercooled water seen in the ice ratios in Figure 2.10. Updraft and downdraft strengths in the ms-500 and ls-500 runs (Fig. 2.9e,h) also exhibit strong signs of both warm and cold phase invigoration versus strictly the warm phase seen at high aerosol loading. The mean radiative transfer profiles (Fig. 2.14) also indicate that the

mid aerosol runs do not experience the strong stratification and enhancement of static stability from ~2-5 km present at high aerosol loading that inhibit upscale convective growth.

5. ***Most of the strongest feedbacks due to aerosol and stability perturbations are seen in the boundary layer, though some are stronger above the freezing level (Fig. 2.15e)***

While this may seem self-evident due to our experimental approach, the persistence of some of these impacts and their more indirect effects came as a surprise. For example, the stability perturbation structure remained remarkably steady throughout our simulations, since perturbing the temperature affected the LW forcing directly in a positive feedback loop (Fig. 2.6a-f). Strong boundary layer responses can also be seen in cloud fraction (Fig. 2.8) and the cumulus mode statistics (Table 2.4). However, when considering upscale growth, some of these impacts are more prominent above the freezing level, such as the "Goldilocks Zone" enhancement of vertical mass fluxes and condensate loading in congestus and cumulonimbus, changes to ice ratio above 5 km (Fig. 2.10), and changes to stability throughout the column from LW absorption by aerosols.

In summary, this study has not only revealed many complex sensitivities to both thermodynamics and aerosol loading but has also illuminated several paths for future work that we plan to explore. For example, although we have learned a great deal about the bulk responses of the different cloud modes to aerosol loading and static stability, the impacts of these environmental factors on the evolution of the full cloud lifecycles was not examined. A follow-up study examining these impacts on cloud lifecycle is presently underway. Another avenue of future work would be to thoroughly compare the individual clouds in our simulations with observations (e.g., dropsonde, cloud probe, radar, radiometer, and lidar data) from the CAMP^{2}Ex field campaign and other appropriate campaigns, as well as to explore a wider variety of

environmental values for those quantities such as shear, moisture, and CAPE which have been seen to impact convective development and deep convective AIEs. This would further characterize the multifaceted processes occurring in such environments.

CHAPTER 3 – ADDING NEW SCIENTIFIC AND PROCEDURAL IMPROVEMENTS TO A CLOUD TRACKING TOOL[2]

3.1) Introduction

Recently, there has been a great deal of interest in robust, large-scale objective identification and tracking of clouds and other meteorological features (e.g., Heus and Seifert 2013; Hu et al. 2019; Núñez Ocasio et al. 2020). As the atmosphere is not a static system, diffusive, advective, dynamic, and thermodynamic processes ensure that atmospheric phenomena of interest are nearly always either in motion or in a moving frame of reference, which is indicative of the utility of tracking frameworks for atmospheric data in general. Clouds are one such phenomenon for which tracking is useful. Clouds are near-ubiquitous features in the Earth's atmosphere and play critical roles not only in tropospheric heat and moisture transport, but also with respect to scattering of solar radiation and absorption/emission of infrared radiation in the context of the global climate. Convective clouds and cloud systems can range in size from tens of meters to hundreds of km; exist for as short as a few minutes and as long as days; exhibit a wide variety of morphological characteristics; and undergo complex lifecycles that have a growing initiation stage, a quasi-steady-state mature stage, and a collapsing decay stage (Cotton et al. 2011). All of these elements make clouds prime candidates for objective analysis techniques, which has been successfully demonstrated in cloud tracking studies (e.g. Freeman et al. 2022; Leung and van den Heever 2022). However, clouds are far from the only meteorological phenomena where robust tracking tools are useful. For example, tracking on

---

[2] This study , entitled "*tobac* v1.5: Introducing Fast 3D Tracking, Splits and Mergers, and Other Enhancements for Identifying Meteorological Phenomena", is a joint-first-author paper led by G.A. Sokolowsky and S.W. Freeman, and is currently in preparation for submission to Geoscientific Model Development (Sokolowsky and Freeman et al. 2022 – in preparation)

quantities such as aerosol concentration aerosol concentration (e.g. Bukowski and van den Heever 2021) and trace gas concentrations and masses (e.g. Zhang et al. 2022) is of enormous use to atmospheric chemists, climate scientists, and others studying movement of such quantities within the atmosphere. Convective cold pools, which are density currents that manifest via the evaporation of convective precipitation, can be identified and tracked using atmospheric thermodynamic and dynamic quantities such as temperature or temperature proxies (e.g. potential temperature), water vapor concentrations, and near-surface wind fields (e.g. Tompkins 2001; Feng et al. 2015; Drager and van den Heever 2017; Drager et al. 2020). Atmospheric radiative quantities, such as outgoing longwave radiation (OLR), have clear uses in cloud objective identification (e.g. Gill and Rasmusson 1983; Weickmann 1983), but can also be leveraged to detect and track processes such as sea ice evolution (e.g. Singarayer et al. 2006). If such tools are made general enough, even people working outside the realm of atmospheric science can benefit from them, such as ornithologists or entomologists interested in bird and bug seasonal migration, respectively (e.g. Crewe et al. 2020; Knight et al. 2019). At present, however, only one such tool can address this myriad of uses: the Tracking and Object-based Analysis of Clouds (*tobac*; Heikenfeld et al. 2019), a Python package based in objective analysis principles that uses artificial intelligence to identify, discretize, and track objects and fields of interest.

The most powerful and unique feature of *tobac* is its agnosticity regarding input variables and grids – i.e., it can be used with virtually any gridded input dataset and variable, meteorological or not. *tobac* was initially developed for use with clouds and associated meteorological data (Heikenfeld et al. 2019), and has been used for these purposes, such as tracking warm-season deep convective systems and Mesoscale Convective Systems (MCSs) via

satellite-observed infrared brightness temperature (e.g. Li et al. 2021; Kukulies et al. 2021). However, due to this unique variable agnosticity, *tobac* has also been used for other applications: for example, tracking of haboobs via dust concentration (e.g. Bukowski and van den Heever 2021). *tobac* both draws from and expands upon the procedures developed in earlier cloud identification and tracking tools, and we have detailed some of the history of tracking tools in the atmospheric sciences below.

First and perhaps foremost, tracking has historically required a great deal of human input and attention due to a lack of computationally efficient methods for the location, assessment, and connection of different features in time. One such early method, the Thunderstorm Identification, Tracking, Analysis, and Nowcasting tool (TITAN; Dixon and Weiner 1993), is a well-designed and powerful approach for the detection and tracking of thunderstorms, and while it does incorporate computational analysis of data, it is heavily based in physical principles (i.e., it requires specific datasets/variables and can only be used to track certain things) and manual assessment of output due to computational limitations at the time. As discussed in Dawe and Austin (2012), earlier studies involving tracking of clouds (e.g. Zhao and Austin 2005a,b; Heus et al. 2009) required scientists to contribute a great degree of manual/visual selection to the clouds they considered in their studies. This is not only time-consuming to an extent that is impossible to scale for large datasets, but also introduces subjectivity to an analysis that should ideally be objective. Some later publications (e.g. Plant 2009; Dawe and Austin 2012; Heus and Seifert 2013) have more general criteria allowing for automated selection, but exhibit computational or scientific limitations due to their design. Dawe and Austin (2012) tracked clouds as a combination of 3D liquid water content and buoyancy in 3D space, but required computationally expensive determinations of 4D spatiotemporal connectivity and had specific

definitions for different cloud components, limiting use on a variety of different cloud types. Heus and Seifert (2013) simultaneously expanded on and improved the tractability of the approach of Dawe and Austin by connecting thermals, cloud envelopes, and precipitation shafts, but reduced the amount of memory needed by projecting these fields into 2 spatial dimensions and using the vertical dimension as a contiguity check between feature columns. However, both Dawe and Austin's (2012) and Heus and Seifert's (2013) methods were designed to be used in LES output fields of shallow cumulus with a vertical extent of less than 4 km, limiting the applicability of these methods with cloud systems that exhibit more vertical structure (e.g., layered clouds, deep convection, or slantwise convection) and other datasets that have similarly complex 3D morphology.

Gropp and Davenport (2021) recently developed a powerful tracking tool for supercell thunderstorms that was effectively demonstrated at a 3-hourly time resolution (coarser than the requirements of many tracking tools) but is limited by its specific case use and cannot be easily generalized due to its inherent design. Similar utility limitations can be seen in the many tracking tools which have incorporated procedures for splits and mergers of tracked objects (e.g. Dixon and Weiner 1993; Gambheer and Bhat 2000; Hu et al. 2019; Núñez Ocasio et al. 2020): most of these tools leverage the specific phenomena being detected and tracked in order to construct a definition for the determination of splits and mergers, which preclude such treatments from being used outside the framework of these particular cases. Some other tools, such as the TempestExtremes package developed by Ullrich and Zarzycki (2017), utilize a more general framework akin to *tobac*'s variable- and grid-agnosticity and similarly reduce phenomena to single, pointwise features, but lack *tobac*'s comprehensive area and volume analysis tools for further investigation of feature-associated data. As there is a rich history of different detection,

analysis and tracking tools in the atmospheric sciences, *tobac* utilizes many of the strengths of these preexisting tools while broadening science applications and optimizing procedures to result in a more general and powerful analysis tool.

Despite the utility of *tobac* and the strengths of this tool over earlier such packages, the increasing resolution of models and identification of new use cases (such as in LES modeling) have made it clear that the code base requires enhancement from both a scientific and procedural point of view. Necessary updates to *tobac*'s scientific capabilities are the inclusion of the third spatial (vertical) dimension in feature detection and tracking and internal tools allowing for spectral smoothing of data. More procedural improvements which would also further the utility of this package are increases in computational efficiency, ingestion of multiple data sources on different grids (e.g., performing feature detection on one grid and segmentation on a separate grid), and treatments for model periodic boundary conditions (PBCs).

Our goal in this publication is to present each of these new improvements that have been released as part of *tobac* v1.5. In Section 3.2, we discuss the strengths and weaknesses of *tobac* v1.2 with demonstrations of its capabilities, while Section 3.3 details the scientific improvements. Section 3.4 presents the procedural enhancements, and Section 3.5 provides a summary of our changes to *tobac*, concluding thoughts on *tobac* v1.5, and some planned changes which will be included in future releases.

3.2) *tobac* v1.2 overview

Before elaborating on the new capabilities which have been included in *tobac* v1.5, we begin with a general overview of the design and capabilities of the original *tobac* library, denoted v1.2. *tobac* was first developed through a multi-institutional collaboration (Heikenfeld et al., 2019) in order to provide a code base for "tracking and analysing individual clouds in different

types of datasets". This package consists of three primary components: *feature detection*, or the objective identification of features from minima or maxima in gridded data; *segmentation*, or the discretization of the same or different gridded data based on previously detected features; and *tracking,* or the linking of detected features to one another through time. Segmentation and tracking operate independently of each other, but both require feature detection to have been performed on a data field of interest. These procedures can be performed on any gridded data field of interest, though for *tobac* v1.2, it must exist in two (feature detection, segmentation, and tracking) or three (segmentation only) spatial dimensions, requiring some form of data dimensionality reduction for feature detection and tracking when data grids are in 3D. These key elements, demonstrated on a field of radar reflectivity data, can be seen in Figure 3.1. The fine details of how these components were constructed is detailed in Heikenfeld et al. (2019), but we discuss the generalities and how *tobac* can be applied to different use cases within this section.

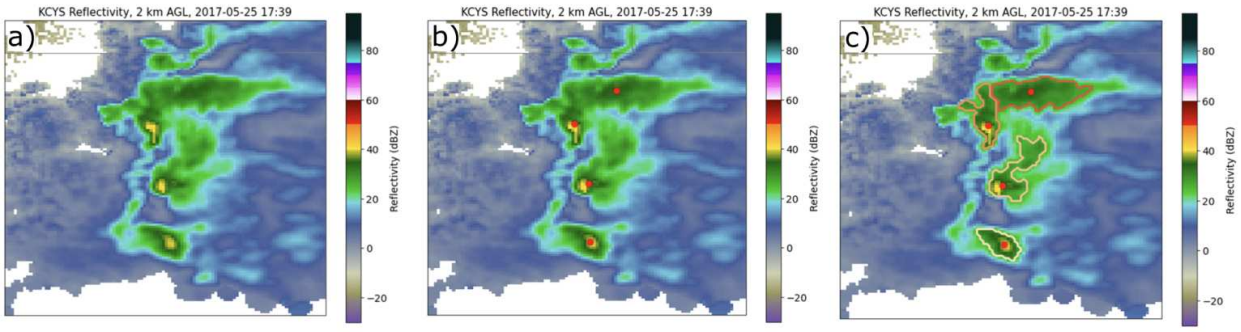

Figure 3.1: Demonstration of *tobac* feature detection and segmentation of NEXRAD radar reflectivity data from the Cheyenne, WY radar on 25 May 2017 during the C^{3}LOUD-Ex field campaign (van den Heever et al. 2021a). Panel (a) shows the actual radar data, panel (b) displays the objectively identified radar reflectivity features for a threshold of 30 dBZ as red dots, and panel (c) shows the reflectivity segmentation regions associated with the features as differently colored outlines.

Feature detection in *tobac* is performed by first establishing one or more data thresholds which gridded data values must exceed in order to be considered for placing features. Contiguous regions of gridded data meeting these criteria, as well as additional criteria such as a user-set minimum size, are saved as unique single-point identifiers (which can be set by users to

either be geometric centroids, weighted-difference positions, or extrema within the data) with their horizontal positions in each spatial dimension. If multiple thresholds are used, features detected at a higher-magnitude threshold that exist within a lower-magnitude region of features supersede and replace the feature(s) detected at the lower-magnitude threshold (e.g. Heikenfeld et al., 2019, their Figure 2). This multi-threshold capability allows for the identification of greater-magnitude data existing within a lower-magnitude data region without losing the sensitivity to lower-magnitude data. For example, using multiple thresholds on a modelled vertical velocity field enables the detection of deep convective updrafts within a broader, weaker updraft region as well as isolated, weak boundary layer thermals. An illustration of feature detection being performed on gridded NEXRAD radar reflectivity data obtained during the CSU Convective Cloud Outflows and UpDrafts Experiment (C^3LOUD-Ex; van den Heever et al. 2021) can be seen in Figure 3.1a-b. In this figure, convective storms in a grouping near Cheyenne, WY (Fig. 1a) are identified using a radar reflectivity threshold of 30 dBZ. Each of these storms is labeled as a single-point feature, marked in Fig. 3.1b. With the identification of such features, the additional components of *tobac* – segmentation and tracking – can be fully utilized.

The segmentation approach within *tobac* v1.2 begins with a previously identified set of *tobac* features. Where the feature detection procedure reduces contiguous regions of data to single points, segmentation discretizes a full volume or surface area associated with each of these features. For both 2D and 3D segmentation, the skimage.segmentation.watershed procedure (van der Walt et al. 2014) is used. In this method, feature locations are used to place 'seeds' in the data, which are expanded outwards progressively until reaching a data boundary or another expanded seed – hence the term 'watershedding'. This allows for the discretization of data

regions pertaining to each feature, even when multiple features exist within the same contiguous data region. In 2D watershedding, this procedure simply operates in two dimensions, but for 3D watershedding, the entire vertical column where our 2D feature is located has markers placed in it, except where data points do not exceed the segmentation data threshold. In circumstances where data fields are layered, staggered, discontinuous in height, or otherwise irregular through the vertical dimension, this may lead to some data fields being erroneously segmented together, but such data are often identifiable through quality control of *tobac* output. The discretized field, or "segmentation mask", for each timestep is saved as an array. Segmentation fields produced on 2D radar reflectivity data from 2D radar reflectivity features are shown in Figure 3.1c. These regions illustrate the wider reflectivity fields outside of the convective cores that are associated with each of the detected features, likely precipitation regions raining out from the larger clouds being driven by the convective cores.

Finally, the tracking procedure within *tobac v1.2* also requires a previously existing set of *tobac* features. These features are then used with the Python Trackpy library (Allan et al. 2021) to predictively link connected features in time. The presence of this tool within the *tobac* package introduces time evolution to the phenomenon identification that feature detection does and feature-associated area/volume produced by segmentation.

Despite the clear objectivity, utility, and power contained within this tool, *tobac* v1.2 had several important limitations from both a scientific and procedural standpoint, as touched on in the introduction. The limitation of feature detection and tracking to 2D, as well as the column-based approach to 3D segmentation using 2D features, means that data fields which do not reduce cleanly into 2 dimensions (e.g., environments with strong vertical wind shear or layered clouds; deep convective clouds with multiple discontinuous vertical regions producing

condensate; tilted convective storms; and intrusions of aerosol layers composed of different species at different altitudes) might produce untrustworthy or confusing results when analysed using *tobac* v1.2. The included data processing tools are also limited, with no bandpass or spectral filter techniques included in the *tobac* v1.2 package to smooth or isolate data in noisy fields. From a computational perspective, the original implementation was also not well optimized (taking weeks or more to process large datasets), requiring substantial increases in computational efficiency for tractable usage with large datasets. Using detected features to segment data that exists on a different grid is also challenging with this version of *tobac*, as it requires a great deal of user processing to remap data to different grids. Finally, *tobac* v1.2 also lacked the ability to recognize and treat features, segmentation fields, and tracks on data with PBCs, a common characteristic in idealized numerical models. All of these needs motivated the improvements that are discussed in the following two sections.

3.3) tobac v1.5 – Scientific Improvements

3.3.1) 3D Inclusion

One of the most scientifically consequential improvements to *tobac* made as a part of v1.5 is the addition of the vertical dimension to feature detection and tracking, as well as an overhaul of 3D segmentation. Due to the structure of *tobac*, each of these changes required different modifications to the core modules contained within the code base.

For feature detection, much of the overall code logic remains unchanged, but is expanded to include the additional spatial dimension. The feature detection functions are now capable of determining whether their input data exists in two or three spatial dimensions, after which they branch accordingly within the code. When 3D data are input, contiguity and spacing of regions within this data are now assessed in all three spatial dimensions versus just the horizontal

dimensions. Further, the code also supports both uniform and non-uniform vertical grid spacing, allowing for use with modelling and observational data exhibiting either of these common grid structures. Data fields with a 3D input now output two additional data points, 'vdim' and 'altitude', which are absent from 2D output. Including these additional data can be used for an abundance of analyses that depend on vertical information, e.g., defining the vertical structure of updrafts and downdrafts within convective clouds; identifying intrusions of concentrated aerosol layers; and highlighting vertical layers of elevated environmental stability, to name a few.

In addition to the wider variety of scientific use cases that vertical information enables, these code changes also lead to substantial differences in feature detection output between 3D data and their counterparts reduced to 2D, such as that seen in Figure 3.2. Here, a model vertical velocity field is used for feature detection of updrafts at 1, 3, 5, and 10 m/s thresholds, with the 2D reduction being a plan view of the column maximum value. Figure 3.2a illustrates how much of the vertical structure of a 10 m/s feature in the data (white dots within the colored isosurfaces) is captured by our new method, and shows via comparison to Figure 3.2b that 3D features' horizontal positions may differ from their 2D-projected counterparts when the vertical dimension is included in feature detection and positioning. While 2D feature detection is less computationally expensive than 3D and may be a faster solution that produces comparable results, users may also find that 2D projections of 3D data can lead to erroneous results, such as that demonstrated in Figure 3.3. Here, a cumulus cloud and cirrus cloud existing within a sheared environment are traveling in opposite horizontal directions, with the cumulus cloud also moving upwards in time. Fig. 3.3a-c depict how *tobac* v1.2 is able to identify the clouds in the initial scene, but fails to track the cumulus cloud due to the cirrus cloud hiding it from view in Fig. 3.3b due to the two-dimensional framework. This leads to the cirrus cloud being correctly tracked

through time, while tracking of the cumulus cloud is nonexistent, its height evolution is missed, and the failure to detect it as a feature in Fig. 3.3b leads to it being considered a separate, completely new tracked feature in Fig. 3.3c. Conversely, Fig. 3.3d-f depict the time evolution of this scene when 3D motion and detection are considered by *tobac* v1.5: not only are these two discrete clouds recognized, identified, and tracked correctly in time, but the vertical displacement of the cumulus cloud is also apparent in its track. Thus, a possible error arising from collapsing 3D data to 2D is the disappearance of 3D features.

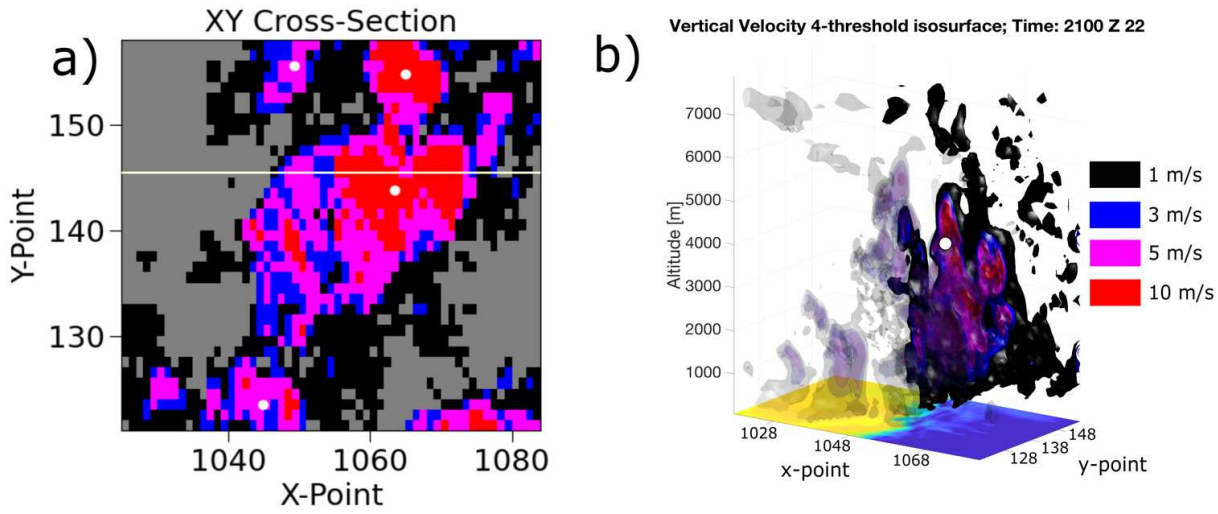

Figure 3.2: An illustration comparing cross-sections of 2D and 3D updraft four-threshold feature detection on the same model 3D vertical velocity field. Panel (a) shows the projection of column maximum vertical velocity and the multiple features contained in this area, while panel (b) shows a cutaway 3D isosurface plot of a 3D updraft detected at the 10 m/s threshold covering the same area as panel (a). Black, blue, magenta, and red shading indicate pixels exceeding the 1 m/s, 3 m/s, 5 m/s, and 10 m/s thresholds, the white dots illustrate feature positions within each cross-section, and the white line in panel (a) represents the location of the front-left cutaway in panel (b), ahead of which (in y-point space) transparent isosurfaces are used to reveal the complex inner structure of the updraft via the opaque isosurfaces.

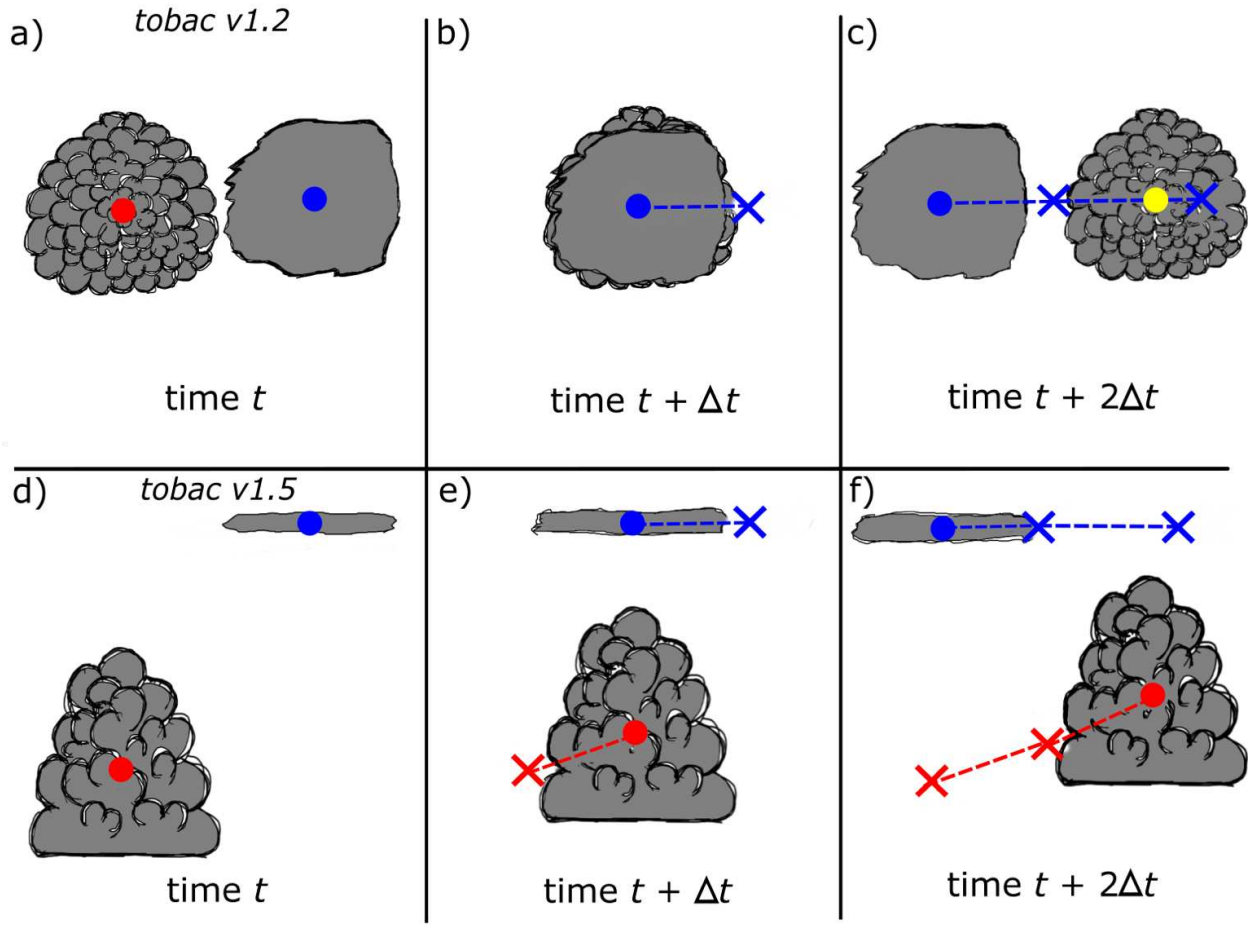

Figure 3.3: A depiction of *tobac v1.2* (top row, plan view) and *tobac v1.5* (bottom row, vertical cross section) feature detection and tracking for a scenario with upper-level cirrus moving over cumulus cloud developing in a sheared environment. Each column's panels are depictions from the same time. The *tobac v1.2* approach pictured in the top row fails to capture the temporal evolution and vertical propagation of the cumulus cloud due to the overlying cirrus, and even incorrectly recognizes the cumulus in panel (c) as a completely new feature and track from its earlier stage in panel (b). In contrast, the *tobac v1.5* approach in panels (d-f) consistently and continuously identifies each cloud due to their separation in 3D space, resulting in correctly linked cloud tracks for each of the cirrus and cumulus. The colored circles denote different features at their present times in each panel, with the colored X's indicating their position at previous times and the dotted lines representing the corresponding tracks. The symbol t here denotes a generic starting time, while Δt denotes the timestep from scene to scene.

Unlike with feature detection, the segmentation routine in *tobac* v1.2 already has some capabilities for 3D data processing, as discussed in the previous section. The column-based 3D segmentation approach – where the entire vertical column at a feature location is seeded with markers for watershedding (the segmented regions are identified growing outward from the seeds) - works reasonably well for 2D features when the 3D field being segmented does not exhibit much vertical stratification or wind shear. However, seeding the full column is not ideal

when we have the feature's vertical position, as seen in 3D-detected features. As such, we have introduced a new "box seeding" method which seeds a box of user-defined size in each dimension centred at the 3D location of the feature. This eliminates the issues from seeding an entire column, while also ensuring that features which are close in 2D space but exhibit greater vertical separation do not unduly influence each other's segmentation masks. A depiction of the differences in 3D segmentation from each method can be seen in the schematic pictured in Figure 3.4. This figure depicts a multi-layered cloud field of cumulus, altostratus, and cumulonimbus, where segmentation is being performed on total condensate. The top row (Fig. 3.4a-b) illustrates the use of the new box seeding method and the ensuing segmentation fields, with the bottom row (Fig. 3.4c-d) visualizing the older column seeding method and its output. The segmentation masks produced are markedly different between 3.4b,d, with there being clear examples of misattributed segmentation fields: the cumulonimbus cloud (red feature) is broken up into multiple segmented regions from the features associated with the altostratus (cyan and magenta features) and cumulus (orange feature) clouds below.

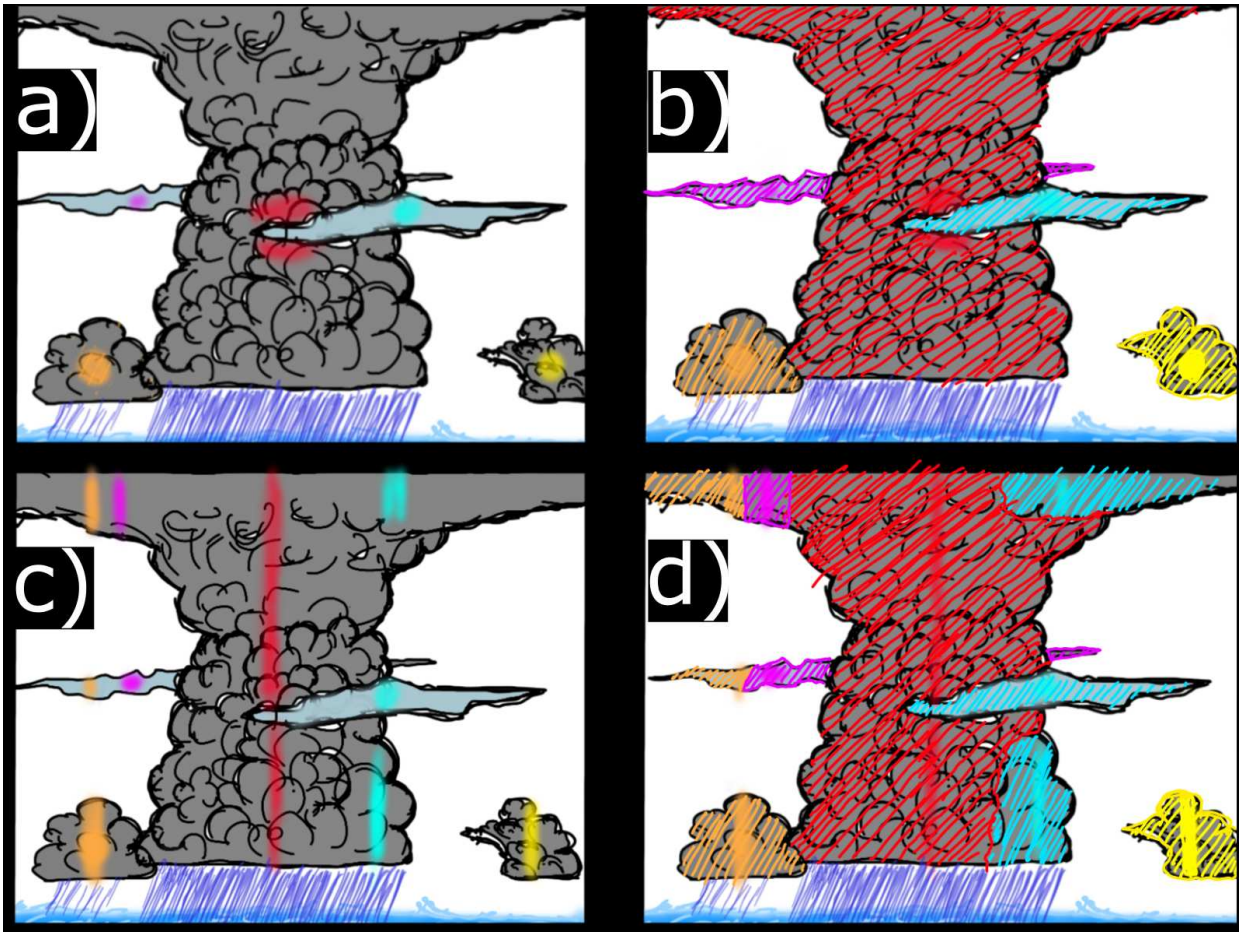

Figure 3.4: A schematic of the new box seeding approach versus the older column seeding approach for *tobac* 3D segmentation. Panels (a-d) depict a scene comprised of a mix of convective and stratiform clouds, with feature detection and segmentation being performed on a total condensate field. The top two panels (a,b) depict the new tobac v1.5 box seeding method, and the bottom two panels (c,d) depict the older column seeding approach. The left column shows the positions of the initial features used as segmentation markers as highlighted lines or circles, with the segmentation regions produced from these markers hatched with the corresponding color in the right column.

A further example of this procedure using LES model data is seen in Figure 3.5: Fig. 3.5a shows the segmentation mask volume produced via column seeding, while Fig. 3.5b's segmentation mask was produced by box seeding covering 5x5x5 cells. Fig. 3.5a's segmentation mask clearly exhibits anomalous cells extending up and down from the main volume, including a disconnected region of cells about 1 km above the rest of the mask, which are unphysical and do not manifest in the box-seeded mask seen in Fig. 3.5b. Since minimizing user effort for objective analysis is one of the key motivators for the development of *tobac* and other comparable tools, use of the box seeding approach here is clearly the superior approach when users have the choice

to do so. This benefits the science itself by making analyses more consistent and less subjective, and also permits layered feature detection and segmentation.

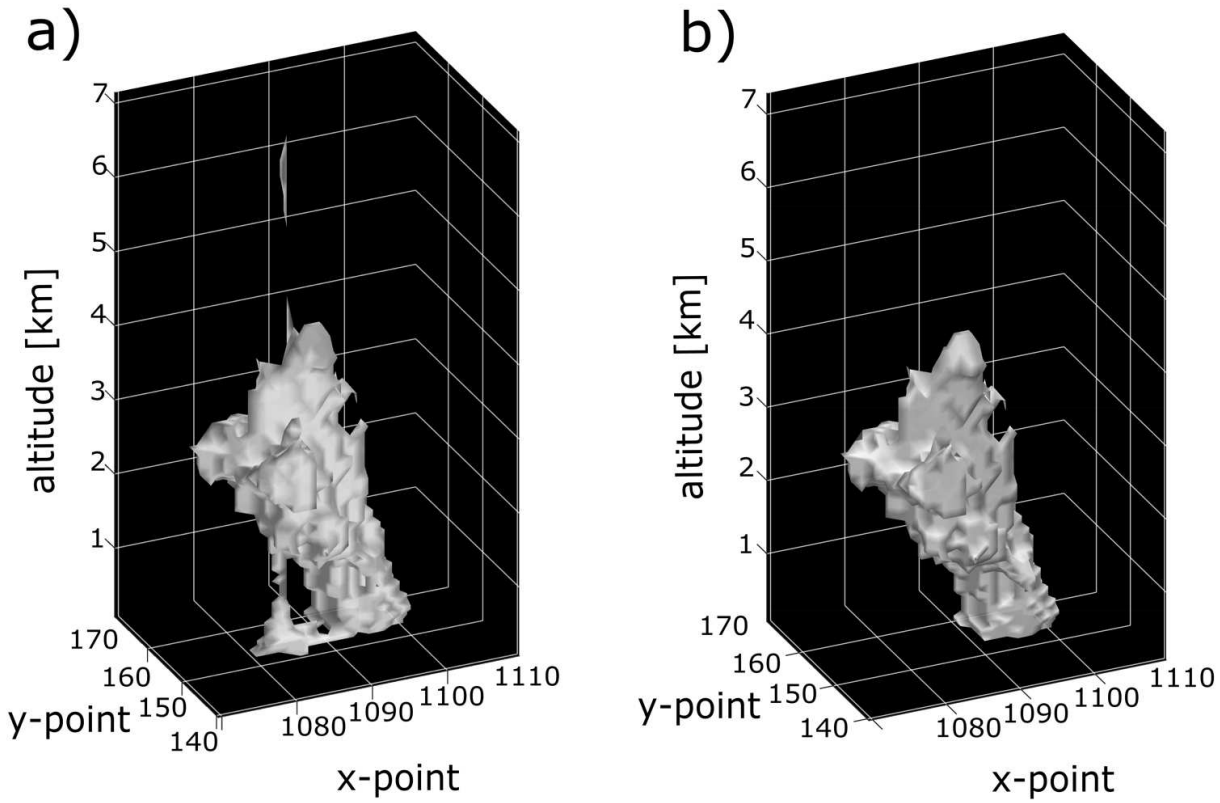

Figure 3.5: Demonstration of 3D segmentation using (a) the original "column" versus (b) the "box" seeding method, showing the differences in output produced by the different methods. 3D feature detection was performed on LES numerical model vertical velocity data from the Regional Atmospheric Modeling System (RAMS) v.6.2.12, with segmentation being performed on the corresponding model total condensate field. Segmentation in panel (b) used a uniform box seed size of 5 in x, y, and z.

Finally, the 3D modifications to tracking are more comparable to those seen for feature detection than segmentation, but include similarly powerful advances to both of these components. Since tracking in *tobac* is largely processed using Trackpy functions, we leveraged the preexisting Trackpy framework to perform 3D tracking, keeping results both internally consistent and enabling the use of the same general methodology, regardless of whether the user is tracking on 2D or 3D data. Further, our implementation of 3D tracking in *tobac* v1.5 allows users to track on data in 3D with irregularly spaced vertical grids (e.g., stretched model grids)

without requiring the user to re-grid the data. Figure 3.6 illustrates the use of 3D tracking on NEXRAD radar reflectivity data. In this data, a convective core that tilts with height is detected and tracked, showing the movement of feature position in both horizontal space (Fig 3.6a-c) and vertical space (Fig 3.6d-f). Since the feature tilts from west to east with height, the actual 3D centroid appears to be misplaced in the 2 km AGL plan view (Fig 3.6a-c), but the vertical cross section (Fig 3.6d-f) indicates that our detected feature centroid is indeed located here in 2D projected space due to its center being at roughly 4 km AGL. Thus, identifying the centers of such features and discretizing associated data fields are much more realistic with 3D feature detection and box seeding, respectively. As tracking brings temporal evolution into feature analyses, incorporating the vertical dimension further expands these capabilities by allowing users to assess the change in vertical position over time instead of just the horizontal projected position. For use cases where the features of interest are known to exhibit vertical movement as part of their evolution – such as the growth and decay of convective clouds; the development of cold pools and hail cores in thunderstorms; and mechanical lofting of aerosols such as dust or pollen – the importance of including this dimension is essential in feature assessments over their life cycles.

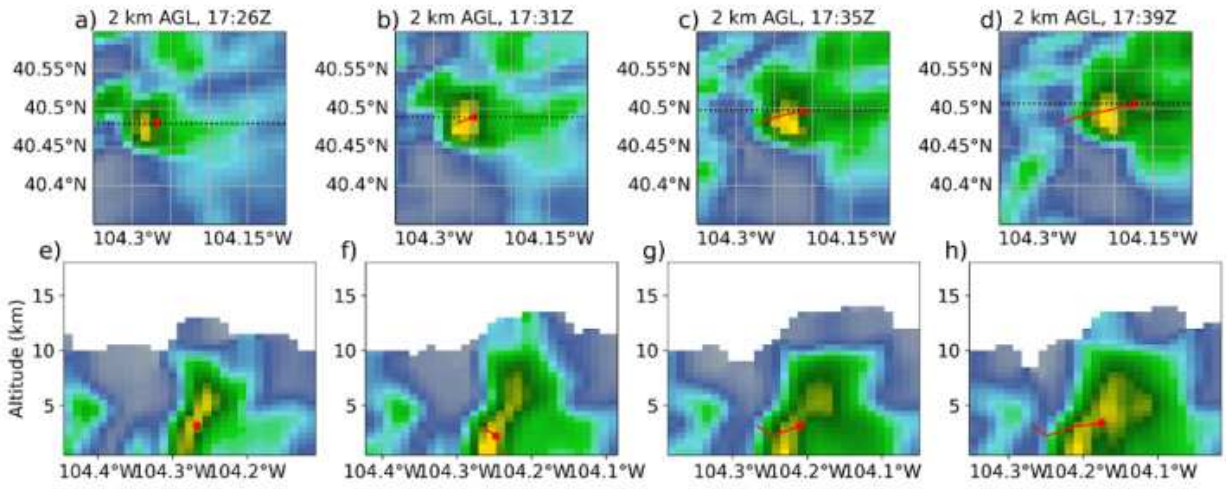

Figure 3.6: Demonstration of 3D tracking in *tobac* on NEXRAD radar reflectivity data. The top row shows the plan view in latitude-longitude space, while the bottom row consists of latitude-altitude cross sections corresponding to each of the times presented in the plan view above – thus, (a) and (e); (b) and (f); (c) and (g); and (d) and (h) are all pairs. The red dot shows the present feature location, while the red line trailing behind it shows the detected track.

3.3.2) Spectral Filtering Tool

In addition to the scientific benefits of expanding the dimensionality of tobac and enabling it to process splits and mergers of features, the addition of new data processing tools also expands scientific utility. While *tobac v1.2* already included some methods for smoothing of data, certain observational and model fields may still be too noisy for these preexisting tools to be useful (i.e., environmental noise that hides the presence of contiguous features), making the use of feature detection and other *tobac* procedures more challenging without additional data processing methods. In order to streamline working with such data for future users of this package, a new spectral filtering tool has been incorporated into *tobac* as part of the v1.5 update. This tool is designed to facilitate the identification of meteorological phenomena at specific spatial scales (e.g. the MJO, equatorial waves, atmospheric rivers, mesoscale vortices, etc), and to remove sub-mesoscale noise in high-resolution data. For example, with the MJO, sub-mesoscale wind fluctuations might obscure the overall propagation of the convectively active envelope.

The spectral filtering tool works by first performing a discrete cosine transform (DCT) on 2D atmospheric fields, representing them in spectral space as a sum of cosine functions with different frequencies (Denis et al. 2008). The resulting spectral coefficients correspond to normalized wavenumbers that can be converted to actual wavelengths, which are then used in the construction of a bandpass filter that has the same shape as these spectral coefficients in wavelength/wavenumber space. Multiplying this bandpass filter with the spectral coefficients removes wavelengths outside of the user-specified band, which can then be converted back to the original domain via inverse DCT. A visualisation of atmospheric data and the spectral elements used for filtering are demonstrated in Figure 3.7. Fig. 3.7a displays the initial 2D input field (here, a a WRF relative vorticity dataset), Fig. 3.7b illustrates the transformation of the data in Fig. 3.7a to spectral space, and Fig. 3.7c-d show the construction of 1D and 2D bandpass filters for wavelengths between 400 and 1000 km. The results from applying such filtering to an ERA5 vertically integrated water transport dataset and a WRF relative vorticity dataset are shown in Figure 3.8. Figs. 3.8a and 3.8c illustrate the original, pre-filtered fields of ERA5 and WRF data, respectively, while Figs. 3.8b and 3.8d illustrate the same corresponding fields after utilization of the filter. It is clear from Figure 3.8 b and d that the application of the spectral filtering greatly enhances our ability to identify large-scale, lower-frequency features in highly noisy data. Inclusion of this tool in *tobac* v1.5 quite clearly expands the package's utility while reducing the amount of extra work needed for end users to pre-process data of interest. This technique has previously been used to identify mesoscale vortices in convective permitting climate simulations (e.g., Kukulies et al. 2022, in review).

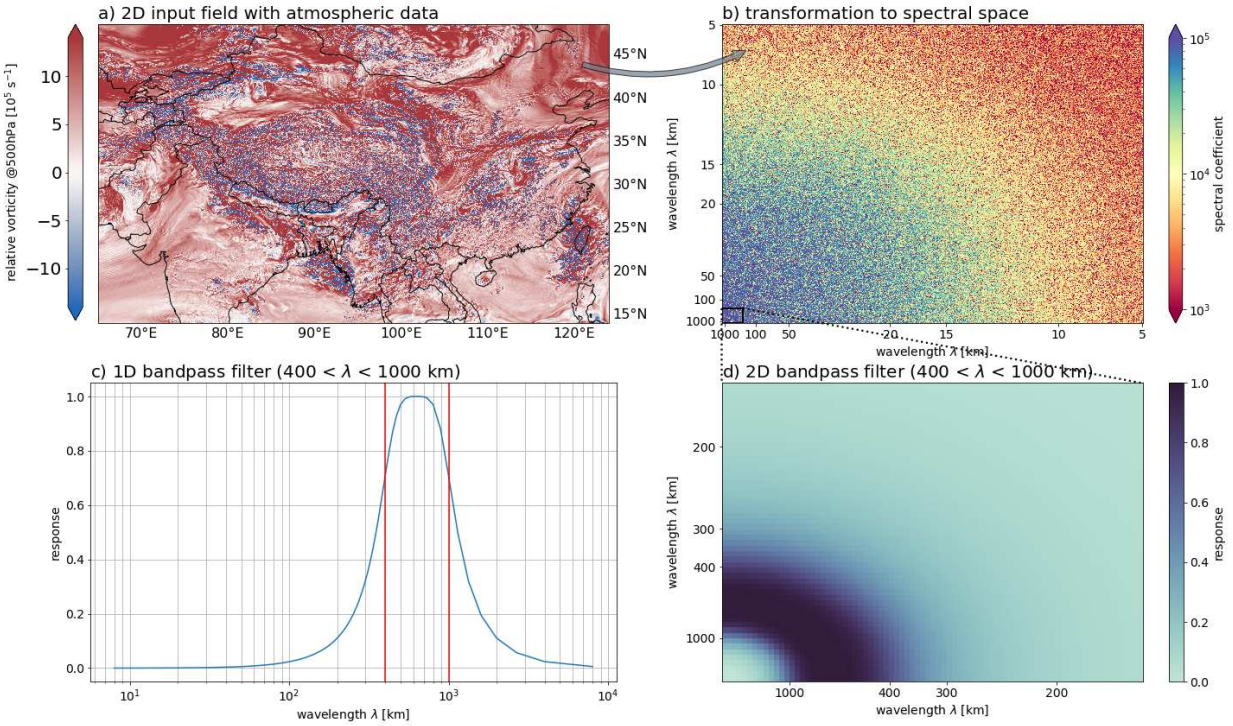

Figure 3.7: Visualization of spectral decomposition of atmospheric input fields and construction of a bandpass filter that can be specified by the user and is used to filter the input data. a) 2D input field with atmospheric data at one time step, here: hourly relative vorticity at 500 hPa [10^5] of a 4km WRF simulation over South East Asia. b) The same data after the DCT, represented by spectral coefficients as a function of wavelengths in x and y direction. c) Response of constructed bandpass filter as a function of wavelength. The two red lines indicate the cut-off wavelengths that can be specified by the user (here: 400 and 1000 km). d) Same bandpass filter but in 2D spectral domain with same shape as b) but zoomed in to show the filter response for wavelengths between 400 and 1000 km.

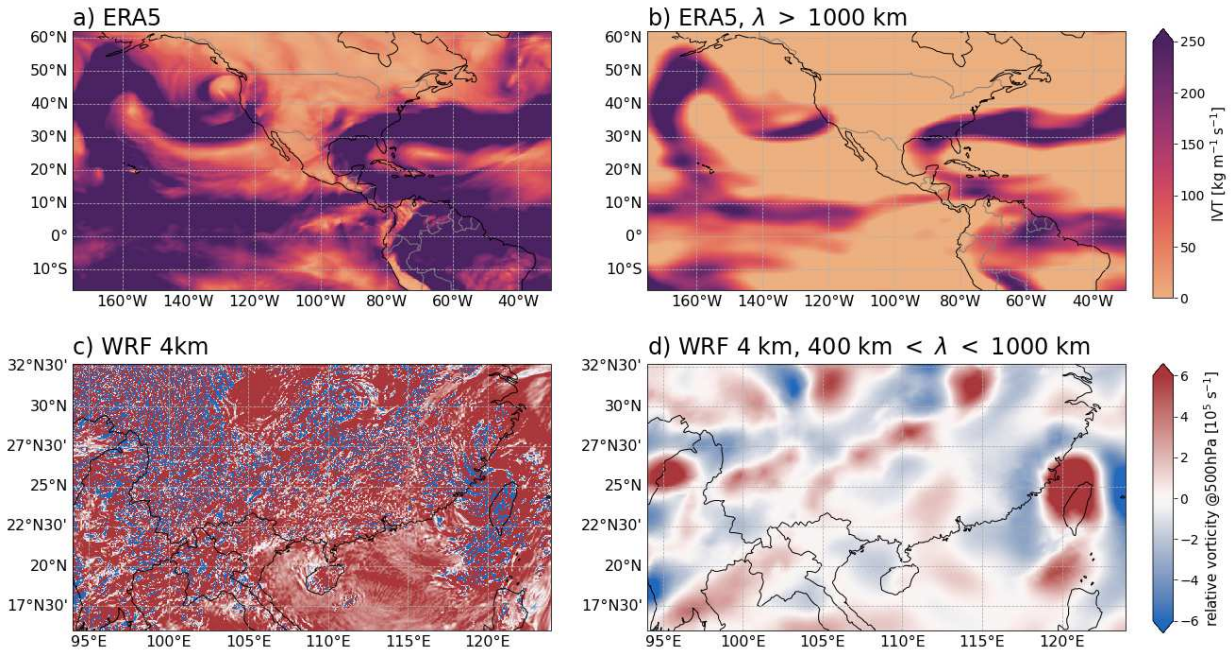

Figure 3.8: Examples for hourly atmospheric input fields (a, c) and their corresponding spectrally filtered fields (b, d). a) Vertically integrated water vapor transport (IVT) [kg m^{-1} s^{-1}] from ERA5 at 2021-01-27 10:00:00 UTC showing an atmospheric river over the San Francisco Bay area b) Same as in a) but spectrally filtered for wavelengths > 1000 km, c) Relative vorticity at 500 hPa [10^5 s^{-2}] from a WRF simulation with 4km grid spacing over Southeast Asia for 2008-07-18 05:00:00 UTC (when Typhoon Kalmaegi hit Taiwan) d) Same as in c) but spectrally filtered for wavelengths between 400 and 1000 km. Note that the typhoon over Taiwan only becomes visible in the vorticity field after the filtering has been applied, because the original vorticity field is dominated by sub-mesoscale noise.

Overall, the 3D implementation and the spectral filtering tool add a great deal of scientific power to *tobac* by expanding on the types and dimensionality of contiguous structures that it can identify within datasets, allowing the tool to be used with more dynamically evolving phenomena, and providing an additional level of filtering to isolate atmospheric phenomena of interest. However, even more improvement of *tobac* can be achieved with the addition of procedural changes such as code optimization, homogenization of grids for different data, and treatment of PBCs. These procedural adaptations are discussed at length in the following section.

3.4) tobac v1.5 – Procedural Improvements

3.4.1) Code Optimization

Several inefficiencies were identified across the body of code, and subsequently, alterations were made to each module to enhance their overall computational speed. Making

these changes led to speedups on the order of 100x for feature detection and 1,000,000x or more for tracking. The scaling of these modules' speeds as a function of the number of features, a proxy for data size and complexity, between *tobac* v1.2 and v1.5 can be seen in Figure 13, with feature detection in Fig. 3.9a and tracking in Fig. 3.9b. To provide a single example of what this means when using tobac on a moderately sized dataset, performing feature detection on a full day of GOES-16 IR data (1500 by 2500 spatial grid cells, 288 time steps) only takes about a minute of computing time now, where it originally took around an hour with *tobac v1.2* using the same computing platform. This has strong implications for the tractability of using *tobac v1.5* with larger datasets: analyses on especially large datasets (10s-100s of TB) that would take weeks to perform with *tobac v1.2* now only take hours to days, which massively expedites the research that can be conducted with this tool.

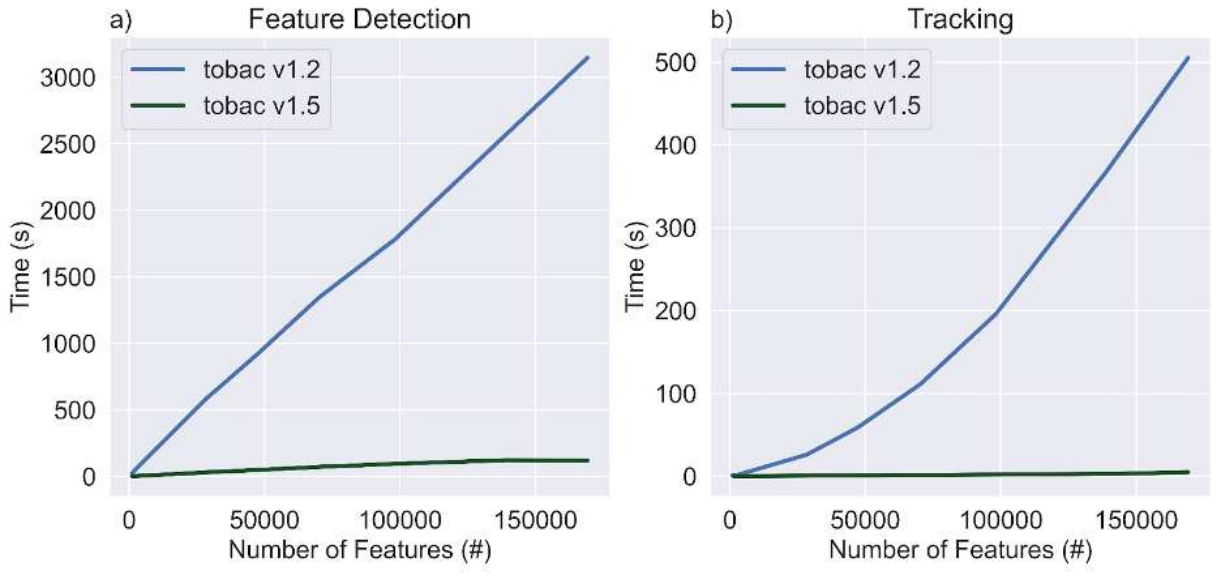

Figure 3.9: A benchmark comparison of *tobac* speed between version 1.2 (Heikenfeld et al. 2019) and version 1.5, demonstrating the increase in speed using a full day of GOES-16 Channel 10 IR imagery from 12 June 2021 on a) feature detection, with number of features on the abscissa and time taken to run feature detection on the ordinate, and b) as in a, but for tracking.

3.4.2) Remapping Data on Different Grids

Beyond recognizing that the efficiency of *tobac* needed to be improved to make certain analyses tractable, we also understood that researchers working with data from different sources often have a need to combine these datasets in some way. This process can be greatly complicated by observing platform nuances such as viewing angle and field of view; temporal frequency and spatial resolution; and the dynamic range of the data. Issues such as differing fields of view and spatial resolution have particularly strong implications for the uses of objective analysis tools like *tobac* due to the projection of data onto different spatial grids. Within the framework of *tobac*, we have introduced a new data processing tool which allows for the combination of datasets (both models, both observational, and even a mix of the two) so that *tobac* can be more easily used with a broader variety of data. One case for the use of this tool is in observational analysis of convection via radar and satellite datasets, which we demonstrate in Figure 3.10. Features detected from NEXRAD reflectivity data exceeding a 30 dBZ threshold are shown in Figure 3.10a. These features are then used as markers to segment a GOES-16 satellite-observed brightness temperature dataset, pictured in Fig. 3.10b. The satellite brightness temperature data have been remapped to the same grid as the radar data prior to performing the segmentation process, so that features are correctly located within the segmentation field of interest. Ultimately, the segmentation outlines shown in Fig. 3.10b depict the anvils corresponding to each radar reflectivity feature, except for the top-right feature marked by the grey dot in Fig. 3.10b, which is a convective core that does not yet have an associated anvil.

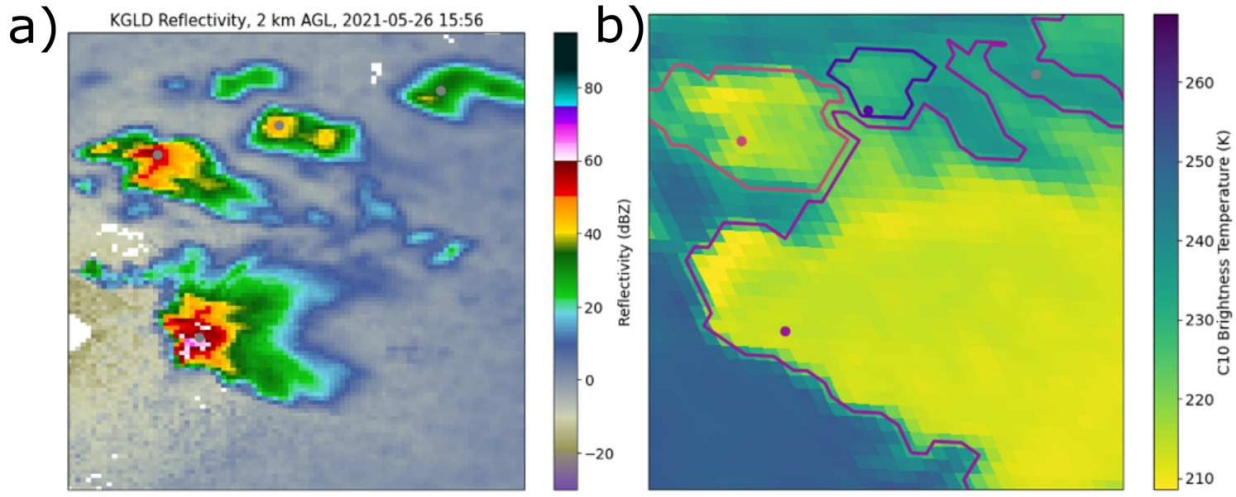

Figure 3.10: A depiction of the output from the new procedure for differently gridded data included in *tobac* v1.5. Panel (a) shows NEXRAD radar reflectivity in dBZ from the Goodland, KS site at 15:56 UTC on 26 May 2021, as well as the associated features detected at a 30 dBZ threshold marked by grey dots which represent different convective cores. Panel (b) shows GOES-16 satellite observed brightness temperature in K (initially on a different grid from the radar data), as well as the segmentation masks associated with each of these features as differently coloured outlines. The segmentation outlines shown in panel (b) are produced after regridding the satellite data to the same grid as the radar data and depict the upper-level cirrus shields associated with the different convective cores seen in the radar data.

3.4.3) PBC Treatments

As noted in the introduction, idealized numerical models often utilize PBCs in order to isolate simulations from external forcings and reduce the influence of the lateral model boundaries on the simulation behaviour. With PBCs, phenomena flowing out of one end of the model boundary simply re-enter the domain at the opposite boundary for that dimension. However, v1.2 of *tobac* did not have any capabilities for recognizing the continuity of features, segmentation masks, or cell tracks which crossed or were split into multiple parts by boundaries, and the code base required these improvements for use with model configurations including PBCs in one or both lateral dimensions.

Most of the changes needed for PBC treatments in feature detection lie within the identification of contiguous regions separated by an artificial boundary and the positioning of features which exist across both sides of a boundary. In the original v1.2 procedure, a failure to

recognize when contiguous fields are split by artificial model boundaries leads to an erroneous multiplication of detected features at these boundaries, which further cascades into unphysical segmentation fields and cell tracks. A depiction of PBC feature detection with *tobac* v1.2 and *tobac* v1.5 being performed on an LES model 2D column maximum vertical velocity field can be seen in Figure 3.11. Fig. 3.11a shows the overall data field (with values less than 0.5 m/s masked in grey), and Fig 3.11b visualizes the initial field of labelled regions identified at a 0.5 m/s threshold prior to utilizing our PBC treatment. Fig. 3.11b contains a total of 6 different regions due to the multiple boundary crosses exhibited by this vertical velocity field and would produce 6 different features if a PBC treatment was not applied, despite it being plainly apparent that this field should be a single unified region. After performing our PBC treatment which overwrites the labelled fields, the resulting unified label can be seen in Fig. 3.11c, which would be correctly identified as the single feature it actually is. Utilizing the PBC treatment in the zonal direction also facilitates the use of *tobac* with some global model and observational datasets and represents the first steps towards enabling global tracking. The PBC treatment for segmentation largely follows the same principles as that for feature detection, except it requires adjustments, rather than complete unifications, to be performed when segmentation masks collide at a model boundary. Beyond these, the PBC procedures for feature detection and segmentation are quite similar.

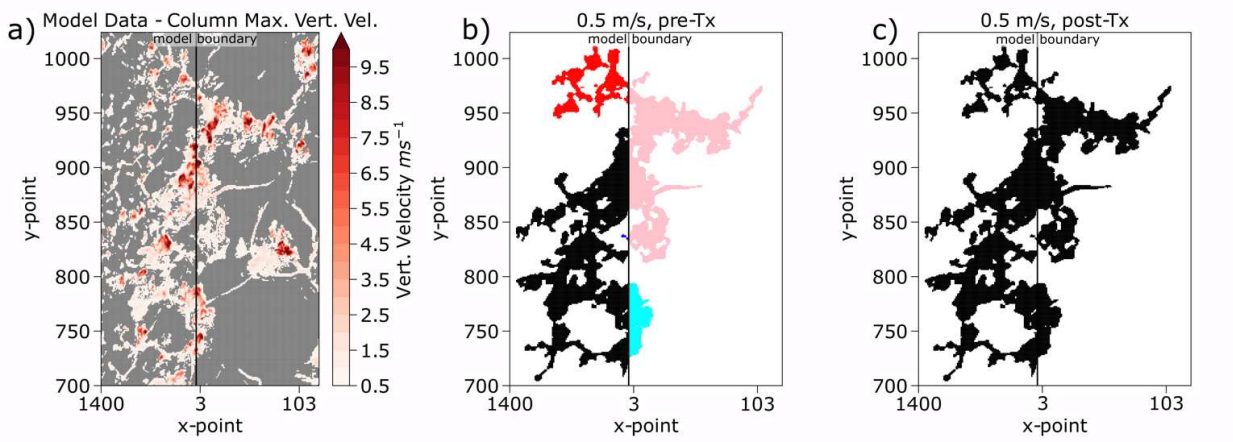

Figure 3.11: Illustration of PBC treatment algorithm for feature detection. Panel (a) shows the original column-maximum vertical velocity field (values less than 0.5 m s^{-1} masked); (b) depicts the six individual feature detection labels produced at a 0.5 m s^{-1} threshold without the PBC treatment; and (c) presents the correct unified label post-treatment for PBCs.

The tracking procedure for PBCs differs from that for both feature detection and segmentation due to the key purpose of the PBC treatment being to link cell tracks that already exist. Provided that one has performed the PBC treatment within feature detection, propagating features will be crossing boundaries in a smooth manner without the introduction of specious features. An example of the PBC tracking approach can be seen in Figure 3.12: Fig. 3.12a displays the erroneous recognition of two distinct cell tracks from an evolving feature crossing the periodic boundary, while Fig. 3.12b shows the correct identification of a single cell track with the PBC tracking approach. This new capability enables a much more robust assessment of cloud lifecycles and other such temporal processes in models with PBCs that would otherwise produce a disjoint or garbled picture with non-PBC tracking, and also becomes increasingly important with smaller domains where boundary crossings are more frequent. As discussed above with relation to feature detection, this PBC code is an important step towards the addition of global feature detection, segmentation, and tracking into tobac. At present, cylindrical (zonal) global tracking (which can be used on GPM data, for example) is enabled within this framework,

but features living near or crossing over the poles are still an issue that must be addressed in future versions of this package.

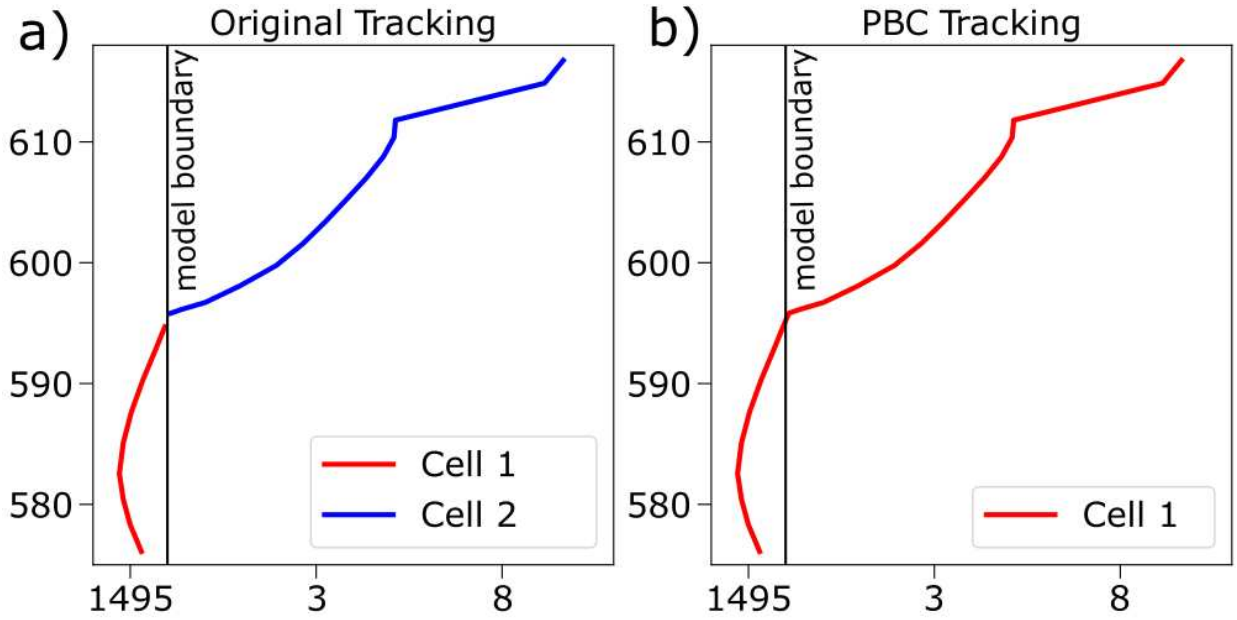

Figure 3.12: A depiction of 2D *tobac* tracking with and without accounting for PBCs. Panel (a) shows the two discrete cells that would be identified by *tobac* v1.2 when a feature crosses a boundary; panel (b) illustrates the single, unified cell that is produced with the PBC tracking procedure.

3.5) Summary and Conclusions

Our overall goals for the improvements to *tobac* detailed within this manuscript were to enhance the package's scientific capabilities and utility, improve its efficiency, and incorporate new tools for data processing and more complex analyses. The inclusion of these changes, as well as the previously existing flexibility of *tobac* and its variable- and grid-agnostic (i.e., capable of working on any gridded dataset) nature, make *tobac* simultaneously one of the most powerful and malleable objective analysis tools that presently exist in our field.

From a scientific point of view, the inclusion of the vertical dimension allows for identification, discretization, and tracking of far more complex meteorological structures than *tobac* v1.2 could perform. It also allows users to better capture the spatiotemporal evolution of clustered phenomena that are difficult to isolate in 2D projections of 3D data. Further, the

processing of mergers and splits within *tobac*'s tracking module greatly enhances the ability to assess the lifecycles, division, and assimilation of atmospheric phenomena which exhibit such processes, without requiring additional record-keeping and data processing by the end user. The included spectral filtering tool also improves the scientific utility of *tobac* by providing a method for users to isolate specific frequencies of interest in the data they are using, precluding the need for external data processing or the use of datasets that have already been smoothed.

The procedural enhancements made to *tobac* as a part of v1.5 also lead to a vast expansion in the capabilities of this package. First and arguably foremost, the computational efficiency improvements, ranging from 100x to over 1,000,000x speedup depending on the module being used and the nature of the data, allow users to conduct analyses in far less time than was possible before. Such efficiency improvements allow users to leverage higher resolution data and overall larger datasets than *tobac* could reasonably manage previously. The data regridding procedures that are now included also enable the combined use of multiple different datasets existing on different grids. New applications that this procedure enables include tracking convective cores on radar and identifying anvil regions with satellite data; and modelling the mechanical lofting of dust in haboob events to compare to satellite observations of the overall dust outflow. The new spectral filtering tool also expands the types of different data that users can include for their analyses – for example, detecting and tracking of African Easterly Waves that are obscured by noise in satellite wind field observations. Finally, adding the capability to recognize and robustly address PBCs has also widened the utility of *tobac* by enabling its use with applicable model data. PBCs are commonly used in idealized models, which would be prime candidates to analyse using the older *tobac v1.2* if they did not have these boundary conditions.

Although we have made many thorough modifications to the *tobac* code base as a part of v1.5, future updates are already in the works as part of the next major release, *tobac* v2, and an active, international community of developers continue to maintain its code base. While much of the future improvements are still under discussion, some of the key elements that are planned for the next major release include integration with the TiNT is not TITAN (TiNT; Raut et al. 2021) tracking package, and a transition away from *tobac*'s current memory-intensive data structures to data structures that allow for out-of-memory computation instead. The overarching vision for *tobac* v2 is, at present, to continue development and enable better support for Big Data use cases.

CHAPTER 4 – UPSCALE GROWTH OF TROPICAL TRIMODAL CONVECTION[3]

4.1) Introduction

In the global tropics, convective clouds are ubiquitous and fall into one of three primary convective modes: shallow cumulus clouds, moderately deep cumulus congestus (hereafter congestus) clouds, and deep convective cumulonimbus clouds (Johnson et al. 1999). The terminal heights of each mode correspond to one of the three tropical-mean stable layers: the planetary boundary layer's capping stable layer, the 0 ºC stable layer, and the tropopause. Thus, it logically follows that the position and strength of these three stable layers govern the characteristics of the overall trimodal distribution. Radiative-convective equilibrium (RCE) studies of trimodal tropical convection conducted by Posselt et al. (2008) have indeed identified that each stable layer separates discrete vertical circulations between them, and bulk analyses of trimodal convection have also emphasized the impact of low-level stability and environmental stability stratification on the characteristics of this distribution (Sokolowsky et al. 2022). Each of these trimodal cloud modes plays an important role in heat and moisture transport both within the tropics and globally (Schumacher et al. 2004), potentially impacting the formation of other convective clouds in their nearby environment (e.g. Hohenegger and Stevens, 2013; Ruppert and Johnson, 2015).

Cumulonimbus clouds are generally agreed to have three primary stages over their lifetime: a growth stage dominated by updrafts when CTH steadily increases; a quasi-steady-

---

[3] This study, entitled "Upscale Growth Sensitivities of Tropical Trimodal Convection to Aerosol", is currently in preparation for submission to the Journal of Geophysical Research (Sokolowsky and van den Heever 2022 – in preparation)

state mature stage comprised of a mix of updrafts and downdrafts when CTH remains relatively static; and a decay stage dominated by downdrafts where CTH continuously decreases (Byers and Braham, 1948). The growth and decay stages are also characterized by net upwards and downwards convective mass fluxes (CMFs), respectively (Betts, 1973; Cruz, 1973), which have important implications for the overall transport of heat and moisture. Since isolated cumulonimbus clouds must somehow develop from shallower but deepening convection (hence Byers and Braham also referring to the growth stage as the 'cumulus stage'), characterizing the growth stage and convective motions within clouds overall have been of particular interest to researchers (e.g. LeMone and Zipser 1980; Zipser and LeMone 1980; Morrison et al. 2020; Peters et al. 2020; Leung and van den Heever 2022).

Many hypotheses exist regarding the balance of different processes driving upscale growth of tropical convection (i.e. transition from cumulus to deeper convection). On large scales, Neelin and Held (1987) demonstrate that in the tropics, convection often exists in radiative-convective equilibrium (RCE). Since water vapor is abundant, and the mid-troposphere exhibits little zonal temperature gradient (known as Weak Temperature Gradient theory, e.g. Sobel et al. 2001), large-scale vertical motions result from vertical sources and sinks in heat and moisture. These convective motions in turn affect the evolution of the tropical environment through vertical transport of mass (i.e. CMF), detrainment of cloud mass, entrainment of environmental air, and the compensating subsidence produced by convection (Yanai et al. 1973; Arakawa and Schubert 1974), and these convective motions plainly impact aerosol transport also. Some studies have looked at boundary layer moistening as a key driver facilitating convective development (e.g. Yanai and Johnson 1993; Lin and Johnson 1996; Johnson and Lin 1997), and deeper congestus clouds have also been hypothesized to moisten the mid-troposphere

in a similar manner to how shallow cumulus moisten the boundary layer (Waite and Khouider 2010; Ruppert and Johnson 2015). In agreement with these findings, mesoscale organization and moisture convergence have been argued to be the dominant factors in the upscale growth of populations of congestus clouds to deep convection (Masunaga 2012; Hohenegger and Stevens 2013). As discussed in Masunaga (2012), there is a growing body of observational work associating the deepening of congestus in phase with the active, moistening phase of the MJO (Benedict and Randall 2007), indicating that organized, deep moistening supports upscale convective development. Further, large and organized tropical heat sources, such as MCSs, are known to facilitate the later gregarious development of convection in their surroundings due to gravity wave dynamics (Mapes 1993).

On smaller scales, individual convective clouds produce their own vertical heating profiles due to advective, diffusive, microphysical, and radiative processes (Schumacher et al. 2004) that can impact upscale growth. While the studies discussed in the previous paragraph (e.g. Yanai and Johnson 1993; Lin and Johnson 1996; Johnson and Lin 1997; Benedict and Randall 2007; Masunaga 2012; Hohenegger and Stevens 2013) focus primarily on larger scales, the role of moistening on convective upscale growth on smaller scales is prominent also, with other studies identifying that the transition from shallow to deeper convection essentially occurs when a cloud becomes buoyant relative to its environment. The impact of the diurnal cycle on convective upscale growth has also been examined, with tropical maritime regions exhibiting a nocturnal maximum in convection due to high precipitable water availability (relative to continental regions) and a gradually destabilizing troposphere owing to nocturnal clear-sky radiative cooling (Sui et al., 1997). Orographic influences have also been identified to have

strong impacts on convective upscale growth and maintenance (e.g. Rasmussen and Houze 2016).

As stated above, RCE studies of trimodal tropical convection performed by Posselt et al. (2008) have identified the presence of discrete vertical circulations separated by the 0 ºC stable layer, and an observational study by Luo et al. (2009) using collocated, simultaneous MODIS and CloudSat data has confirmed that some congestus clouds are negatively buoyant at this level and will not continue growing. These "terminal" congestus clouds differ morphologically and dynamically from "transient" congestus clouds which continue growing upscale into deeper convection (Luo et al. 2009; Leung and van den Heever 2022). Oceanic tropical congestus also differ in structure from their continental counterparts, with more "bell-shaped" versus "cauliflower-shaped" appearances and greater condensate loading at cloud base owing to more efficient warm rain processes in comparison to continental clouds (Rangno and Hobbs 2005; Wall et al. 2013).

Convective clouds and their upscale growth are also subject to aerosol direct effects and indirect effects (AIEs), with many recent studies examining hypotheses of convective invigoration by increased aerosol loading (Andreae et al. 2004; Khain et al. 2004; van den Heever et al. 2006; Rosenfeld et al. 2008; Lebo et al. 2012; Altaratz et al. 2010; van den Heever et al. 2011; Sokolowsky et al. 2022). The changes in these clouds' morphology ensuing from aerosol impacts has further implications on the evolution of the tropical environment, the clouds it contains, and their transport of moisture and energy (Grant and van den Heever 2014; Morrison and Grabowski 2011; Sheffield et al. 2015; Anber et al. 2019; Park and van den Heever 2021; Sokolowsky et al. 2022). Numerous studies have identified mitigating factors including environmental factors such as wind shear, CAPE and RH (Khain et al. 2008; Lebsock et al.

2008; Fan et al. 2009; Storer et al. 2010, 2014; Lebo and Morrison 2014; Park and van den Heever 2022; Freeman et al. 2022); the cloud type and organization (Khain et al. 2005; Seifert and Beheng 2006; Koren et al., 2008; van den Heever et al. 2011; Grant and van den Heever 2015), and the convective lifecycle (Phillips et al., 2002; van den Heever et al. 2006; Storer and van den Heever 2013). Questions have also been raised regarding the integrated impacts of aerosols on shallow through deep convection within regional environments, with most studies finding a more muted response to aerosol forcing under such circumstances (Seifert and Beheng 2006; Huang et al., 2009; van den Heever et al. 2011; Grabowski and Morrison 2011; Chen et al., 2016). However, most of these studies are based in snapshot or bulk assessments which do not incorporate temporal evolution into the analysis, in spite of the indication that aerosol impacts on convective processes may vary as a function of lifecycle (Phillips et al., 2002; van den Heever et al. 2006; Storer and van den Heever 2013). Capturing the temporal evolution of key convective growth processes is challenging without robust methods for identifying and tracking the upscale development of convective clouds in time.

Although there have been extensive observational and modeling characterizations of convective upscale growth, remarkably few observations exist of convective vertical motions themselves, especially over oceans (Battaglia et al. 2013). The challenges in collecting such data make it difficult to properly characterize the mechanisms behind convective vertical motions and the controls on these mechanisms. For example, deep convective clouds have strong updrafts and downdrafts (as well as strong gradients between them and turbulence) and may contain large, glaciated particles, making aircraft penetrations difficult to precisely target as well as dangerous (Geerts et al. 2018). Ground-based in situ observations, such as tethered balloons and radiosondes, are also challenging to time and place for interactions with convection that will

produce accurate measurements (Cotton et al. 2011; Marinescu et al. 2020). While differing from the shortcomings of in situ observations, remote sensing observations have their own limitations, such as attenuation of W-band and Ka-band radar in heavy precipitation (e.g. Tanelli et al. 2008). To supplement these observational and modeling efforts, development of analysis tools capable of tracking the temporal evolution for a variety of cloud systems has been a recent focus of researchers (e.g. Dixon and Weiner 1993; Ghambeer and Bhat 2000; Dawe and Austin 2012; Heus and Seifert 2013; Heikenfeld et al. 2019; Hu et al. 2019; Núñez Ocasio et al. 2020), but none of these tools could analyze such multidimensionally complex scenes as tropical trimodal convection without extensive modification. Only with a recent advancement of the uniquely variable- and grid-agnostic Tracking and Object-Based Analysis of Clouds (*tobac*; Heikenfeld et al. 2019; Sokolowsky* and Freeman* et al. 2022, in prep) Python library has robust 3D identification, discretization, and tracking of tropical trimodal convection become possible.

Our goal in this study is to investigate the modeled upscale growth of tropical trimodal convection and its microphysical, dynamic, and thermodynamic sensitivities to aerosol loading on both a morphological and process level. This goal will be achieved through the use of the newly developed *tobac* v1.5 tool. This work is an extension of that in Sokolowsky et al. (2022) (described in Chapter 2). We contrast the composited growth stages of each convective mode, both within the same simulation and between the three simulations. Section 4.2 presents an overview of the model setup and analysis methods, Section 4.3 discusses the results and ensuing analysis, and Section 4.4 details the conclusions and some future research suggestions.

4.2) Model Setup and Analysis Methodology

The methodology of this study relies heavily on the simulations used in Chapter 2 and the *tobac v1.5* tool presented in Chapter 3. Where Chapter 2 utilized a suite of 9 simulations in

which aerosol loading and low-level static stability were co-varied, in this chapter we analyze a subset of these simulations – ls-100 (the control simulation for this study), ls-500, ls-3000 – to focus solely on the impacts of aerosol loading on convective upscale growth. This is achieved by isolating individual periods of convective growth from the clouds in these simulations, contrasting those between shallow and deeper convection during equivalent periods in their growth (i.e., when a growing congestus or cumulonimbus cloud are still at shallow cumulus altitudes) to identify the key upscale growth processes, and then comparing these upscale growth process differences between the simulations. From these simulations, we focus on a 6-hour period of each of these simulations at 1-minutely temporal resolution, in contrast to the analysis of 46 hours of 5-minutely temporal resolution data in Chapter 2's bulk analyses. This 6-hour period covers the nighttime hours from 1300-1900 Z on 22 August (21:00 – 03:00 Local Time 22-23 August), when convection is at its deepest and the trimodal distribution is most apparent. The increase in temporal resolution was necessary to properly link feature movement in *tobac* tracking due to the mean minimum distance between cloud features, as is discussed in Heikenfeld et al. (2019).

Each of the feature detection, segmentation, and tracking components in *tobac,* as described in Chapter 3, were utilized in this study. Feature detection was performed on the model total condensate field, and used 3 thresholds of 0.01 g/kg, 0.1 g/kg, and 1 g/kg. These thresholds were chosen due to the former two thresholds' common use as total condensate thresholds for defining a cloud in modeling studies (e.g. Jiang and Feingold 2006; Cotton et al. 2011; van den Heever et al. 2011) and the third being evenly spaced from the second in logarithmic space. We tracked on total condensate as opposed to updraft velocities because we wanted to capture the evolution of the cloud condensate envelope rather than the individual convective updrafts, as

clouds may contain multiple discrete updrafts that come in and out of existence. Later in the analysis, we impose thresholds on integrated CMF to assess whether a cloud was actively growing. Features were required to be comprised of at least 10 grid cells due to numerical issues that arise in tracking 3D features smaller than this size. Given that the horizonal grid spacing is 100 m and the vertical grid spacing is stretched from 50 to 300 m, this means that cloud features smaller than 300 x 300 x 150 m^3 will not be detected, tracked, and considered in these results. Segmentation was also performed on the model total condensate field, with the minimum feature threshold of 0.01 g/kg being used for segmentation. Tracking was configured to require continuous spatiotemporal evolution of a feature – i.e., features were not allowed to disappear for a frame and then be considered part of the same cell.

Several additional constraints and classifications were used to streamline the overall analysis by identifying the different terminal modes of convection, the presence and length of growth stages in their evolution, and the tracked clouds which were either too short-lived or not convectively active to be of use in this analysis. For cloud classification, the same contiguity and depth thresholds were imposed as in Chapter 2: each convective mode was required to have a base below 2 km, with cumulus terminating below 4 km, congestus between 4 and 7 km, and cumulonimbus above 7 km. The *tobac*-produced segmentation volumes were used to construct mean vertical profiles of each feature-detected cloud, which were then stitched together using the *tobac*-produced tracks into time-height evolving cloud cells. Once complete cell lifecycles were constructed, the maximum and minimum CTH reached over the cloud's lifetime were used to gauge whether the deepest convective cloud mode reached was a cumulus, congestus, or cumulonimbus cloud. Unlike the instantaneous assessment approach used in Chapter 2, this ensures that terminal and transient shallow convective clouds (i.e., cumulus and congestus) are

properly classified and compared to each other and deep convection in the context of upscale growth. For deeper convection, we also imposed a maximum 1-minute change in cloud top height of 2400 m - the maximum vertical velocity present in these simulations, 40 m/s, times 60 seconds. In doing so, we prevent the misidentification of deeper convection from clouds crossing over and precipitating into one another, which can lead to artificially deepened segmentation masks, as growth greater than this is clearly unphysical.

In keeping with previous literature (e.g. Byers and Braham 1948; Betts 1973; Cruz 1973), convective growth stages within the tracked clouds were identified using a combination of CTH evolution and total vertical CMF. For a point in the cloud's evolution to be considered in a growth stage, two criteria must be met: (1) the vertically integrated CMF of the cloud must be positive, and (2) the CTH must be either increasing or static from the previous temporal point. This will undoubtedly include some contamination of the identified growth stages by mature stages (as CTH will be near-constant in the mature stage and a combination of updrafts and downdrafts can still produce a net positive total CMF), however, examining individual tracked clouds revealed to us that many of them exhibit a "pulsing" growth over their lifetimes. In other words, we saw multiple growth stages separated by slight decay or quasi-steady-state periods, after which the clouds often grew even deeper than during their first growth stage. Since our criteria explicitly exclude the decaying periods from our growth stage analysis, by virtue of excluding any periods in time where the CTH decreased and/or integrated CMF was negative, we felt it reasonable to include quasi-steady-state periods if the net mass flux was positive and the CTH was not actively declining.

We also count multiple growth stages from the same continuous cloud, if separated by declining CTH and/or net downwards CMF: it is quite reasonable for a convective cloud

undergoing growth to become deeper, stall a bit due to environmental inversions or other impediments while still actively pumping mass upwards, and then continue growing even deeper once these barriers have been overcome. This finding of pulsed convective behavior is also in keeping with theories of "thermal chains" in convective growth (e.g. Morrison et al. 2020; Peters et al. 2020). Compositing of different growth stages identified in a convective cloud's lifecycle is performed by sorting growth stages both by their parent cloud's deepest CTH and the current stage's maximum CTH. In contrast to clouds with multiple growth stages, some clouds which fit the depth criteria for cumulus, congestus, or cumulonimbus clouds did not exhibit any growth stages. These clouds were therefore excluded from the analyses, as were clouds which did not fit the depth criteria for convective clouds at any point in their lifetimes.

Two different temporal thresholds were imposed for our tracking procedure: (1) tracked clouds must be at least 10 minutes in length, and (2) the growth stage(s) within a tracked cloud must be at least 4 minutes in length. Cumulus clouds, the smallest and shortest-lived of the trimodal distribution, typically exhibit lifetimes of 10-30 minutes (Cotton et al. 2011) and clouds shorter-lived than these are therefore not of interest for this study. The 4-minute growth stage threshold was based in previous studies' demonstration that cloud lifecycles follow a roughly symmetrical evolution from growth to steady-state to decay (Cruz 1973), thus, a 4 minute growth stage length is in keeping with 40% of the minimum lifetime threshold of 10 mins. We also impose a spatial threshold, excluding clouds less than 4 grid cells in depth (less than 400 meters within the boundary layer, ~200 at the surface), as cumulus clouds shallower than this are unlikely to be captured with our *tobac* feature detection threshold, and deeper clouds far exceed this threshold simply due to how they are defined. In Figure 4.1, we provide visual depictions of time-height series evolutions of total condensate and CMF for each of cumulus (Fig. 4.1a,b),

congestus (Fig. 4.1c,d), and cumulonimbus (Fig. 4.1e,f) in the control simulation ~~in Figure 4.1~~ to add context to these clouds' temporal evolution. We also depict example shallow (cumulus) and midlevel (congestus) growth stages in the normalized CMF plots (Fig 4.1, right column) as blue and black bounding boxes, respectively.

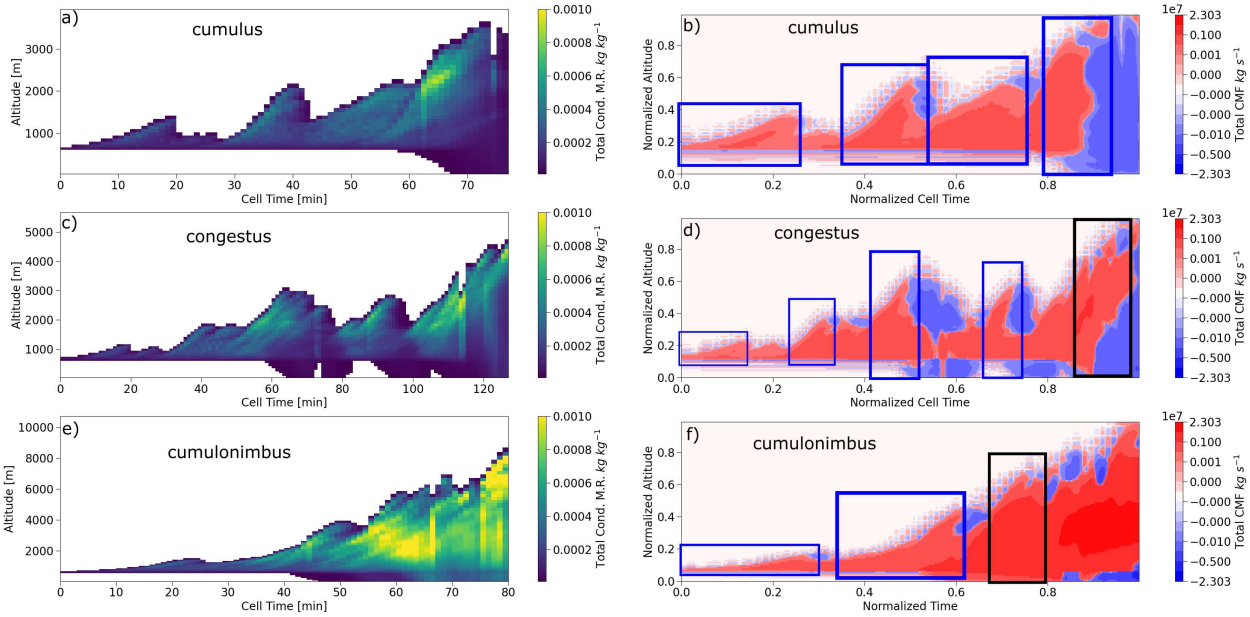

Figure 4.1: Examples of mean total condensate loading (left column) as a function of time (abscissa) and height (ordinate) and normalized CMF (right column) for a single cumulus (panel a,b), congestus (panel c,d), and cumulonimbus (panel e,f) cloud in the control simulation (ls-100). The right column also depicts "cumulus" (shallow) and "congestus" (midlevel) growth stages in blue and black bounding boxes, respectively. For calculation of normalized growth stages, the edges of each bounding box range between zero and one in normalized time-height space. Note that both the horizontal and vertical scales differ for each panel.

All of the growth stages were normalized, interpolated, and composited for each terminal mode within each simulation. Additional filters on growth stage maximum CTH were also used to ensure that comparable stages in convective growth were grouped – e.g., cumulus growth stages were compared with those from congestus and cumulonimbus so long as max CTH during the growth stage was below 4 km, and similarly for congestus and cumulonimbus while the growth stages' maximum CTH were below 4 km ("cumulus stage") and between 4 and 7 km ("congestus stage"). For the normalization process, the minimum and maximum CTH occurring within a discrete growth stage correspond to normalized altitudes of 0 and 1, respectively, with

an analogous approach to normalize time by the beginning and end of each growth stage. In order to smoothly composite values on a uniform grid, we interpolated these data from the depth and time range encompassed by the growth stage to a 100 by 1000 altitude by time grid using the scipy.interpolate.RectBivariateSpline function from the Python SciPy package (Virtanen et al. 2020) and masked values where the total condensate or cloud area were zero in normalized space when compositing data.

We took differences between the composited growth stages of cumulus, congestus, and cumulonimbus for each simulation to ascertain what triggers upscale growth from shallower to deeper convection. Growth stages were categorized by simulation, terminal convective mode, and maximum CTH during growth to ensure that growth stages with similar depths were compared. Variables that were compared in these differences include the mean area; mean total condensate loading; total and mean CMF; and the mean radii and number mixing ratios of all condensate species in RAMS. These variables were initially calculated from our segmentation volumes by taking the sum (total CMF, total area) or horizontal mean (total condensate loading, mean CMF, condensate species) at each vertical level with nonzero area within the feature-associated cloud volumes to obtain a mean cloud profile, concatenating these together in time, and then interpolating and normalizing the data. Data were composited by summing up values across the phase space (counting every instance where an unmasked value was added to the composite) and then taking the arithmetic mean of these data, which provides us with characteristic normalized growth stage properties for each convective mode, depth classification, and simulation.

We compared these normalized differences between the three simulations (ls-100, ls-500, and ls-3000) to understand how increasing the aerosol loading impacted various aspects of the

upscale growth process (i.e., calculating differences of differences). We also analyzed aerosol impacts on the convective growth through changes to our normalized results in the conceptual framework of an entraining plume model (e.g. (Simpson et al. 1965; Yanai et al. 1973; Emanuel 1994). Although this framework is simple and does not wholly consider all of the processes in a convective updraft, growing convective clouds are dynamically similar to entraining plumes, and recent studies of convection reflect that a classical entraining plume model remains an accurate comparison for the growth stage of convective clouds (the focus of this work), even at high resolution (e.g. Takahashi et al. 2021; Strauss et al. 2022). As the growth stage data are normalized and these growing convective clouds are tracked through time using *tobac*, an entraining plume model provides a useful estimate of the cloud dynamic structure that can be contrasted between growth stages of the different convective modes. We primarily utilize the fractional rate of mass entrainment provided in Emanuel (1994):

$$\lambda = \frac{1}{M}\frac{dM}{dz}$$

(Equation 4. 1)

where λ is the fractional mass entrainment rate and M is the convective mass flux. Equation 4.1 is useful for illustration of where in the cloud's vertical structure entrainment and detrainment occur, particularly in combination with our calculations of changes to cloud properties such as area and condensate loading. We use Equation 4.1 with our normalized total CMF data for each mode and growth stage to calculate fractional entrainment profiles and their differences between modes and simulations. Total CMF values less than 10,000 kg s^{-1} (equivalent to a dry 100 m x 100 m x 100 m volume with a density of 1 kg m^{-3} moving upwards at 0.01 m/s) were masked for the fractional entrainment calculations to avoid spuriously large entrainment/detrainment values owing to a small CMF.

We also consider our results in the context of the equations provided by Emanuel (1994) to characterize turbulent plumes originating from a point source:

$$w = \frac{F^{\frac{1}{3}}}{z^{\frac{1}{3}}} * f\left(\frac{r}{R}\right)$$

(Equation 4. 2)

$$B = \frac{F^{\frac{2}{3}}}{z^{\frac{5}{3}}} * f\left(\frac{r}{R}\right)$$

(Equation 4. 3)

$$R = \alpha z$$

(Equation 4. 4)

where w represents the nondimensional vertical velocity, B the nondimensional buoyancy, and F the nondimensional buoyancy flux. R is the radius of the plume at altitude z, α is a constant, and $f\left(\frac{r}{R}\right)$ is a function relating the radial position within the plume to the total radius of the plume. LeMone and Zipser (1980) and Zipser and LeMone (1980) found tropical convective updrafts to exhibit a "triangular" vertical velocity structure with a linear decay of vertical velocity from the maximum at the plume center. This provides $f\left(\frac{r}{R}\right)$ with the general form of:

$$f\left(\frac{r}{R}\right) = \frac{c_r(R - r)}{R}$$

(Equation 4. 5)

where c_r is a constant. Coupling this with our equations above, we have:

$$w = \frac{F^{\frac{1}{3}}}{z^{\frac{1}{3}}} * \frac{c_r(R-r)}{R}$$

(Equation 4. 6)

$$B = \frac{F^{\frac{2}{3}}}{z^{\frac{5}{3}}} * \frac{c_r(R-r)}{R}$$

Equation 4. 7

$$R = \alpha z$$

Equation 4. 8

which, using the definition of R in Equation 4.8, we can simplify Equations 4.6 and 4.7 to:

$$w = \frac{F^{\frac{1}{3}}}{\alpha z^{\frac{4}{3}}} * c_r - \frac{F^{\frac{1}{3}}}{z^{\frac{1}{3}}} * c_r$$

Equation 4. 9

$$B = \frac{F^{\frac{2}{3}}}{\alpha z^{\frac{9}{3}}} * c_r - \frac{F^{\frac{2}{3}}}{z^{\frac{5}{3}}} * c_r$$

Equation 4. 10

Examining Equations 4.9 and 4.10, it can be seen that when all else is unchanged, the magnitude of the first term in the vertical velocity and buoyancy equations scales inversely with the plume radius scaling α – i.e., as the plume's aspect ratio becomes wider at the top and narrower at the bottom (higher α), the positive terms in the vertical velocity and buoyancy equations degrade more rapidly with height. We discuss the implications of different α in terms of the cloud structure in context with our CMF results and the movement of condensate species within the profile.

Keeping the canonical depictions of cumulus, congestus, and cumulonimbus clouds in mind alongside our approach for normalizing, interpolating, and compositing the growth stages, we now analyze the upscale growth sensitivities of the different convective modes to assess how our tracked process changes interact to invigorate or suppress upscale convective growth in the context of an entraining plume model.

4.3) Results and Analysis

4.3.1) Responses of Tracked Convective Modes to Aerosol Loading

Each mode comprising the trimodal distribution is represented in all three aerosol loading simulations. Cumulus clouds are the most frequent mode, with congestus about an order of magnitude less frequent than cumulus, and cumulonimbus one to two orders of magnitude less frequent than congestus (Table 4.1). As aerosol loading is increased, the cumulus mode and associated growth stages monotonically decrease in occurrence, especially at high aerosol loading. Congestus and cumulonimbus responses, however, are nonmonotonic: a moderate increase in aerosol loading increases the frequency of both deeper convective modes (especially cumulonimbus, which are nearly twice as frequent), while a high aerosol loading suppresses both modes (especially cumulonimbus).

Table 4.1: Quantification of cumulus, congestus, and cumulonimbus frequencies, as well as the frequency of growth stages for each mode as a function of aerosol loading. The "ls-100" simulation is our control run, and the percent changes bolded in the ls-500 and ls-3000 columns denote the percent change from the control values.

	Ls-100 count	ls-100 growth stage count	ls-500 count **(+/- % change from control)**	ls-500 growth stage count **(+/- % change from control)**	ls-3000 count **(+/- % change from control)**	ls-3000 growth stage count **(+/- % change from control)**
cumulus	25,998	38,106	24,330 **(-6.42%)**	34,179 **(-10.3%)**	13889 **(-46.6%)**	26115 **(-31.5%)**
congestus	2320	2040 (cumulus) 1804 (congestus)	2451 **(+5.65%)**	1764 **(-13.5%)** (cumulus) 2113 **(+17.1%)** (congestus)	1237 **(-46.7%)**	1298 **(-36.4%)** (cumulus) 1161 **(-35.6%)** (congestus)
cumulonimbus	91	61 (cumulus) 119 (congestus)	181 **(+98.9%)**	99 **(+62.3%)** (cumulus) 167 **(+40.3%)** (congestus)	17 **(-81.3%)**	22 **(-63.9%)** (cumulus) 49 **(-58.8%)** (congestus)

The nonmonotonic changes in the frequency of deeper convection to aerosol loading (Table 4.1, fourth through seventh columns from left) point to a strong nonlinear feedback between greater aerosol loading and cloud microphysics, dynamics, and thermodynamics in deeper convection that does not exist in shallow cumulus. In the following subsection, we analyze and discuss the morphological and dynamical differences between cumulus and congestus clouds in their growth stages (which speaks to the triggers of upscale growth of cumulus to congestus) and also how increases to aerosol loading change this upscale growth process.

4.3.2) Responses of Cumulus Upscale Growth to Aerosol Loading

We start by comparing the cumulus growth stages comprising terminal cumulus with the cumulus growth stages comprising terminal congestus, as differences in these cumulus growth phases determine whether cumulus clouds develop to form congestus. Terminal congestus clouds in our simulation exhibit several important differences from terminal cumulus. The cumulus growth stages of terminal congestus are wider than those of terminal cumulus, and become increasingly so over time (Fig 4.2a). They also exhibit greater condensate loading that moves upwards more rapidly before slowing substantially in association with the increasing mean area (Fig 4.2d). Considering these structural changes in the context of Equations 4.9 and 4.10 with a constant buoyancy flux, the increasing aspect ratio (and thus, increasing α) with altitude results in the plume's maximum vertical velocity and buoyancy decaying more rapidly with height. This suggests that the initial vertical growth of terminal congestus clouds (i.e., their cumulus stage) is more intense and more effective at condensate formation in the cumulus stage than for terminal cumulus clouds, although this ultimately results in a cloud with heavy condensate loading at cloud top and an aspect ratio which inhibits later upscale growth into deeper convection. Dynamically, this process can be inferred through increased total mass flux through the depth of congestus clouds (Fig 4.2g), and a much stronger initial mean mass flux (Fig 4.2j). Congestus clouds also exhibit a reduced fractional entrainment rate in the upper part of the growth profile during the cumulus growth stage, an increased entrainment rate in the lower part, and enhanced detrainment at cloud top (Fig 4.2m). This suggests that terminal cumulus may entrain more air aloft that is thermodynamically unfavorable for convective growth, while terminal congestus entraining air lower in the profile during their cumulus growth stage may have the opposite effect. Developing congestus may also be more effective at moistening the environment, due to

enhanced detrainment at cloud top as seen in Fig 4.4m (blue line near top of profile). Microphysically, we see more active initial nucleation (Fig 4.3a) and growth of cloud droplets (Fig 4.4a) in the cumulus phase of congestus compared with cumulus clouds themselves. This drives enhanced collision-coalescence processes leading to greater drizzle and warm rain production (Fig 4.3d,g) and rain drop sizes (Fig 4.4d,g), particularly higher up in the cloud. The location of congestus-cumulus differences suggest that warm rain production occurs higher aloft in developing congestus, which is reflected in the CMF profiles (Fig 4.2 g,j).

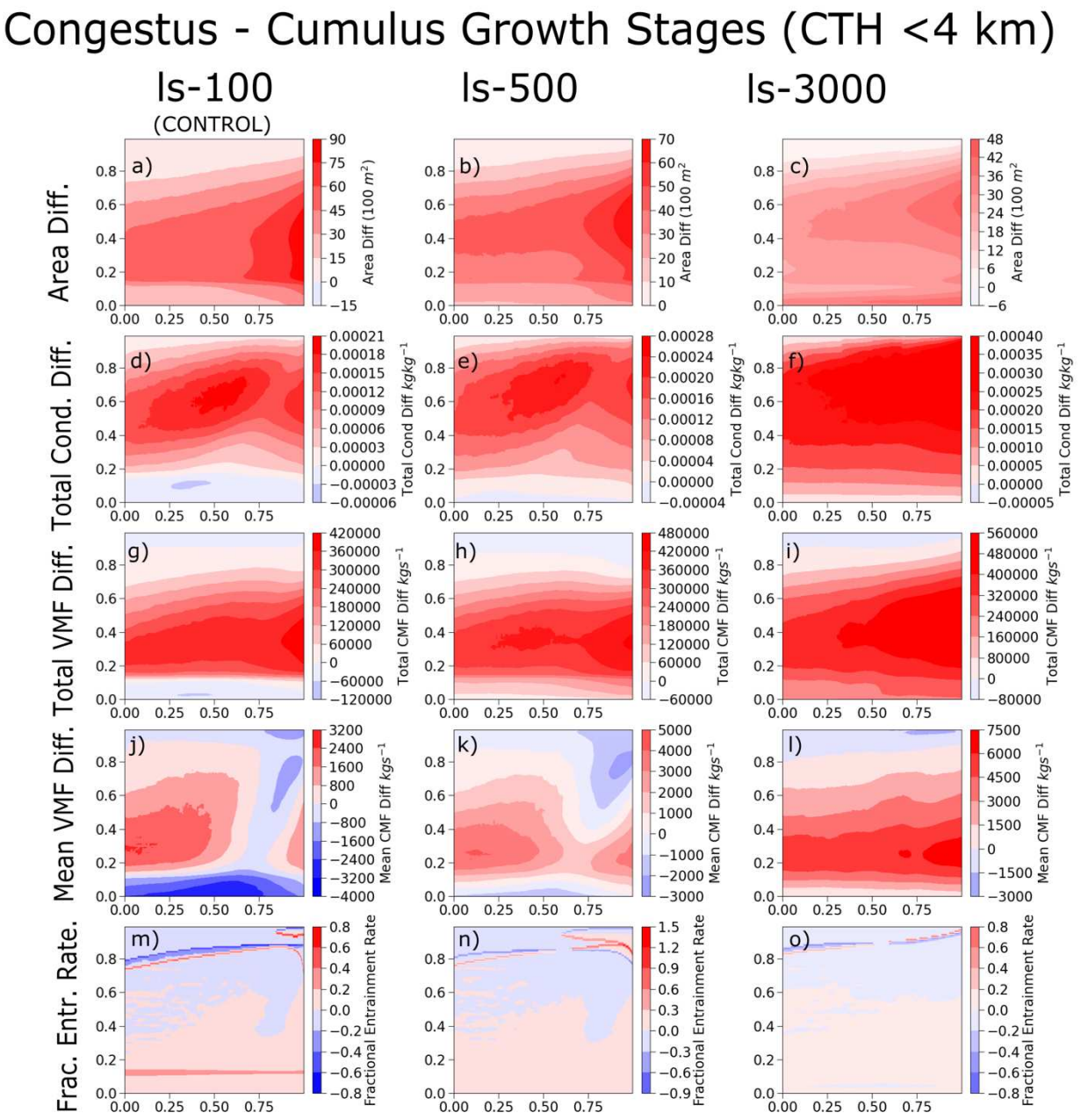

Figure 4.2: Depiction of congestus – cumulus (congestus minus cumulus) growth stage differences during growth stages within the cumulus altitude range. Panels (a)-(c) show the difference in area (in multiples of 10,000 m^2, one grid cell's area), (d-f) the mean total condensate loading difference (kg kg^{-1}), (g-i) the total CMF difference, (j-l) the mean CMF difference, and (m-o) the fractional entrainment rate difference. The left column shows the congestus-cumulus difference in the control simulation, while the center and right columns show the differences in the ls-500 and ls-3000 simulations, respectively. The x-axis denotes normalized time ranging from 0 to 1, with the same being true for the y-axis for normalized altitude. Note that the colorbar differs between panels for the same field.

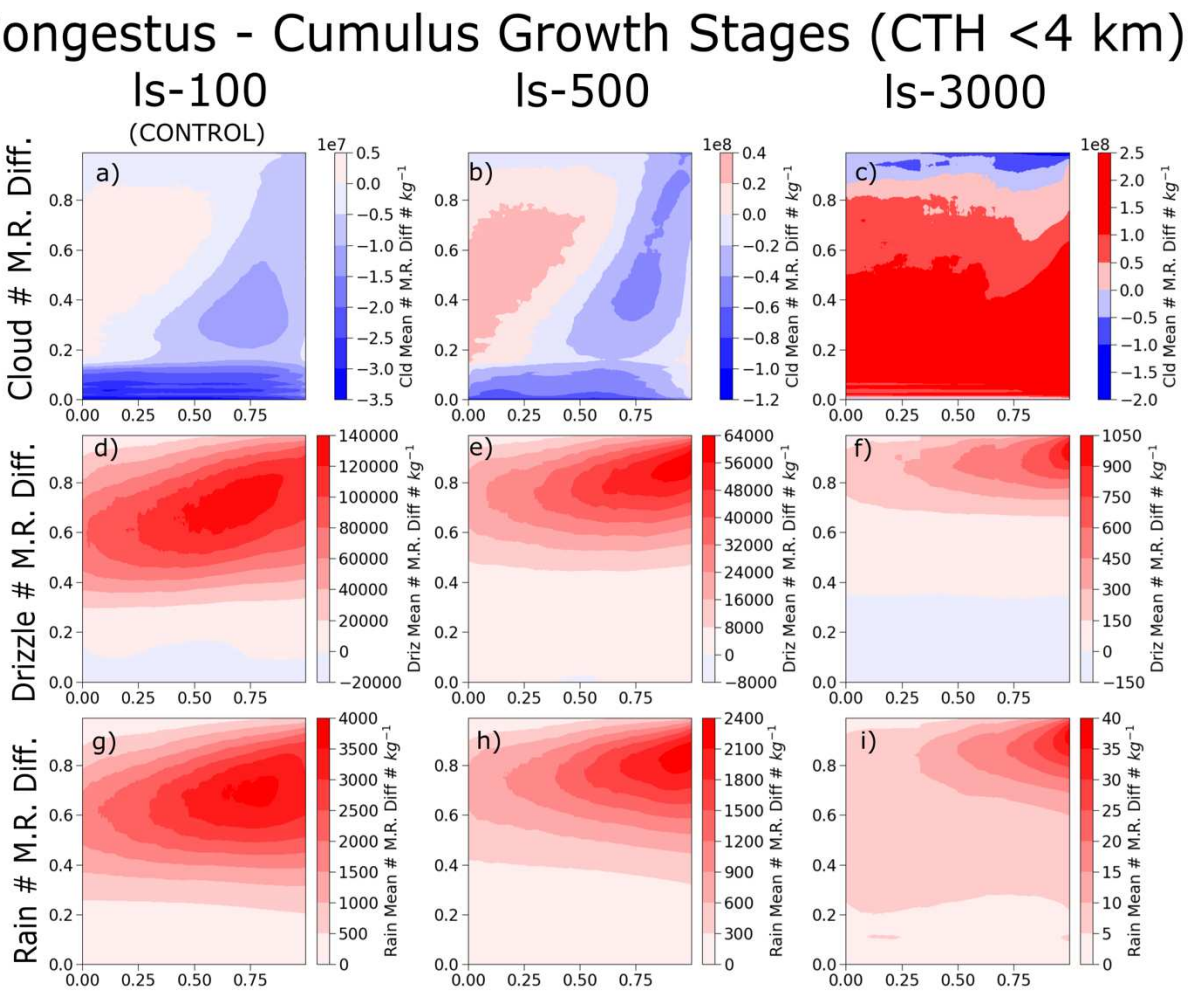

Figure 4.3: The same as Fig. 4.2, but for the number mixing ratio (# kg^{-1}) of different liquid condensate species. Panels (a)-(c) depict the cloud number mixing ratio; (d-f) the drizzle number mixing ratio, and (g-i) the rain number mixing ratio. Note the difference in colorbar scales between the different panels.

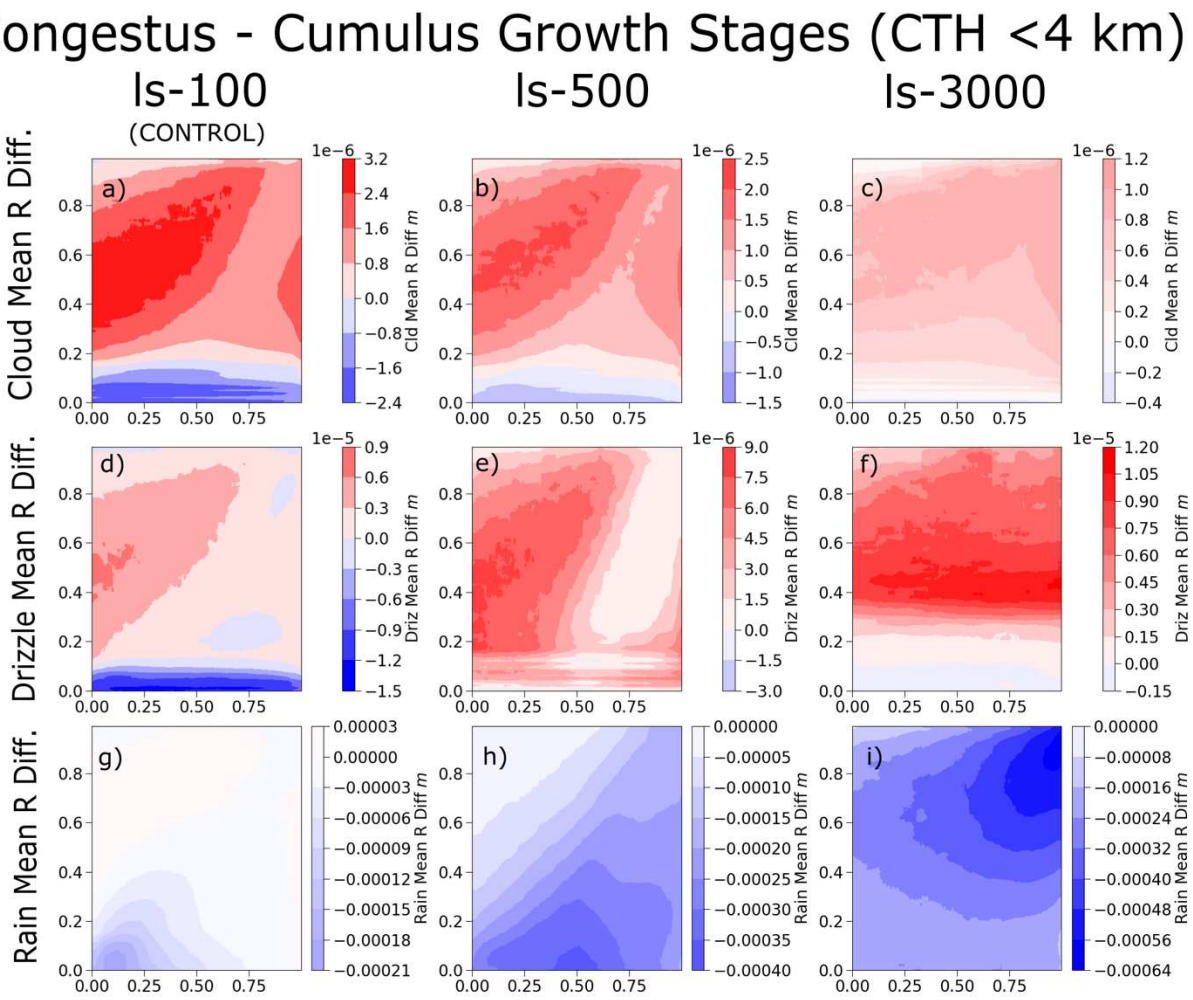

Figure 4.4: The same as Fig. 4.3, but for the mean radii differences of the liquid condensate species. Note the difference in colorbar scales between the different panels.

These microphysical and morphological changes indicate that clouds in the control simulation which grow upscale from cumulus but terminate at the congestus mode have more efficient warm rain processes occurring at a greater elevation than do shallow cumulus clouds. Cloud drops grow more rapidly and do so at higher altitudes (Fig 4.4a), but also reduce in number more sharply after the midpoint of the growth stage (Fig 4.3a). This is associated with an enhancement in drizzle production (Fig 4.3d, 4.4d), but a decrease in rain production (4.3d, 4.4d). Drizzle are also larger in size (similar to the cloud drop population), though this decreases in concert with the difference in mean CMF, while rain sizes in this region are only slightly

enhanced (Fig 4.3g, 4.4g). Comparing the location of our different condensate species, mean CMF, and fractional entrainment over time, the evolution of these values indicates that the cumulus stages of terminal congestus clouds exhibit greater initial vertical development, areal coverage, and condensate loading at a relatively higher altitude within the cloud that also decays more quickly than terminal cumulus clouds. On a process level, these results suggest that the differences in the entrainment profile and aspect ratio of the cumulus clouds developing to congestus favor greater initial lofting and growth of cloud droplets, which in turn enhances collision-coalescence processes in drizzle and rain production. This result is corroborated by a sharp reduction in mean CMF towards the bottom of the profile, indicating greater precipitation in congestus. However, the changes occurring near cloud top ultimately load the top of the profile with more condensate than is present in cumulus, which is associated with a more rapid weakening of the mean upscale growth. Glaciation is negligible in cumulus due to the freezing level existing above the cumulus mode's terminal height of 4 km, so while congestus may glaciate, freezing of condensate is not a process that is required for cumulus to grow upscale into congestus.

We now turn our focus from the congestus-cumulus (congestus minus cumulus) structural differences during the cumulus growth stage to how increases in aerosol loading impact these differences. When aerosol loading is moderately increased, the differences between cumulus and congestus shallow growth stages exhibit several important differences. Congestus clouds exhibit a more mushroom-like aspect ratio (wider cloud top, narrower cloud base; Fig 4.2b), greater condensate loading higher up in the cloud (Fig 4.2e) and increases in mid-level and low-level total (Fig 4.2h) and mean (Fig 4.2k) CMF, respectively, than they do relative to cumulus in the control simulation. In keeping with the entraining plume theory discussed in

section 4.2, Equations 4.9 and 4.10 reflect that all else being equal, the buoyancy and vertical velocity will decay more quickly with height owing to larger alpha (wider cloud top and narrower cloud base). The results in Fig 4.2n, however, do not appear to indicate any strong changes to the entrainment profile. Since the microphysical processes associated with congestus growth exhibit more differences than entrainment (Figs 4.3,4.4, center and right columns), it appears that the manner in which the entrainment profile synergizes with changes in warm-phase microphysical processes plays a larger role than modifications to entrainment dynamics themselves. Microphysically, developing congestus in the moderate aerosol loading scene exhibit greater initial nucleation and lofting of more numerous but smaller cloud drops (Fig 4.3b, 4.4b). This more numerous population of smaller cloud drops suppresses formation of rain and drizzle (Fig 4.3e,h), but drizzle sizes are enhanced (through enhanced collection of available cloud water), especially initially (Fig 4.4e), while rain is suppressed in both number and size (4.3h, 4.4h). For these terminal congestus clouds, the overall morphological changes to the cloud (Fig 4.2b,e) have a negative impact on the upper levels of the mid-to-late growth stage CMFs (Fig 4.2h,k). We hypothesize that this is related to how the change in aspect ratio affects the entraining plume formulation from Equations 4.9 and 4.10: Since the vertical velocity and buoyancy decay more rapidly with height for a plume with a greater value of α (Equations 4.9, 4.10), the enhanced condensate loading at cloud top produces additional drag which further reduces these quantities towards the top of the thermal.

At high levels of aerosol loading, many of the congestus-cumulus growth stage differences follow similar patterns to that of moderate loading, but are even more extreme and detrimental to later vertical growth of the terminal congestus clouds. Clouds are narrower overall but exhibit even more dramatic changes to aspect ratio (Fig 4.2c) and are far more top-heavy in

their condensate mass than at moderate aerosol loading (Fig 4.2f). The enhanced nucleation, lofting, and growth of cloud drops (Fig 4.3c,4.4c) now occurs consistently through the column and does not decay over time as is seen in the control and moderate aerosol scenarios. Since Figs. 4.3f,i and 4.4f,i show a much smaller congestus-cumulus difference in drizzle and rain production, it appears that high aerosol loading fundamentally changes the cloud structure to promote continued lofting and growth of cloud droplets over the course of the growth stage, subsequently making the cumulus growth stages of terminal congestus more microphysically similar to terminal cumulus growth stages, except for the greater promotion of cloud drop growth in congestus. The lack of a negative CMF difference later on in the growth stage (Fig. 4.2i,l) also seems to indicate that strongly suppressing collision-coalescence processes serves to mitigate some of the differences between terminal cumulus and terminal congestus later in their growth stage. However, at high aerosol loading, drizzle sizes are larger in the middle of the growth column (Fig 4.4f), which is also associated with a deeper enhancement of entrainment in the growing congestus clouds (Fig 4.2o). This might indicate that congestus clouds forming in more polluted environments entrain more air in such a way that facilitates drizzle sizes and reduces buoyancy in the midlevels of the growing cloud – e.g., by evaporating smaller drizzle droplets at cloud edges. A similar process has been identified by Small et al. (2009) to result from aerosol perturbations on shallow, nonprecipitating cumulus clouds.

Overall, many of these aerosol-induced changes to the upscale growth process from cumulus to terminal congestus exhibit an initial enhancement of cloud drop nucleation (Fig 4.3b) and condensational growth (Fig 4.4b) in response to moderate loading that later lead the congestus cloud's growth to stall more quickly (Fig 4.2h,k). However, these impacts are nonmonotonic, with high aerosol loading appearing to fundamentally change the cloud structure

in a way that leads to more sustained increases in condensate loading aloft (Fig 4.2f) and CMF (Fig 4.2i,l) at low levels. The congestus-cumulus growth stage comparison only captures the differences between cumulus and terminal congestus during their cumulus growth stages, and thus excludes those changes which impact upscale growth of transient congestus clouds into cumulonimbus. Since Table 4.1 clearly illustrates that moderate aerosol loading enhances both congestus and cumulonimbus while high aerosol loading suppresses both, we explore the aerosol-induced process changes which drive this nonmonotonic response in cumulonimbus in the following subsection.

4.3.3) Responses of Cumulonimbus Upscale Growth to Aerosol Loading

Assessing the characteristics of congestus to cumulonimbus upscale growth in the control simulation through their composited growth stages reveals even more stark differences in these convective modes than between terminal cumulus and congestus. Here, we separately compare the cumulonimbus-congestus (cumulonimbus minus congestus) differences during both the cumulus (CTH < 4 km) and congestus (4 km < CTH < 7 km) growth stages to gauge what differences in cloud structure promote upscale growth during different parts of cumulonimbus and congestus growth.

To begin with comparing the shallow growth stage characteristics, we present the mean area, mean condensate loading, total and mean CMF, and fractional entrainment rate differences in Figure 4.5. Unlike when comparing the shallow development of cumulus and congestus clouds in Section 4.3.2, the cumulus stage in terminal congestus actually exhibit wider clouds at the beginning of their growth (Fig. 4.5a), though by the end of shallow growth cumulonimbus clouds tend to be wider. In the context of the entraining plume consideration from Equations 4.9 and 4.10, this means an initially narrower aspect ratio, thus resulting in a slower decay of vertical

velocity and buoyancy with height in developing cumulonimbus clouds. The widening of the cloud in the cumulus growth stage of cumulonimbus is also concentrated more towards the bottom of the profile, so this aspect ratio difference does not appear to become more extreme over time, either. Condensate loading in the cumulus growth stage is initially less in cumulonimbus than terminal congestus, but it becomes greater in the low-levels shortly after the initiation of the growth phase and deepens over time (Fig 4.5d). Total and mean CMF exhibit a consistent dipole signature, being greater in cumulonimbus at low levels and greater in terminal congestus aloft, while deepening in time similar to the low-level condensate loading difference (Fig 4.5g,j). Since this CMF signal precedes the enhancement in condensate loading, it appears that sustained vertical mass flux in the low levels facilitates condensate formation in this region of the cloud, and leads to the establishment of a wider cloud base and narrower aspect ratio more supportive of deep convective growth. Although developing cumulonimbus entrain over a deeper layer at cloud top than terminal congestus (Fig 4.5m), they entrain less environmental air than terminal congestus through much of the growth column during the latter half of shallow growth, which may also support deeper convective growth.

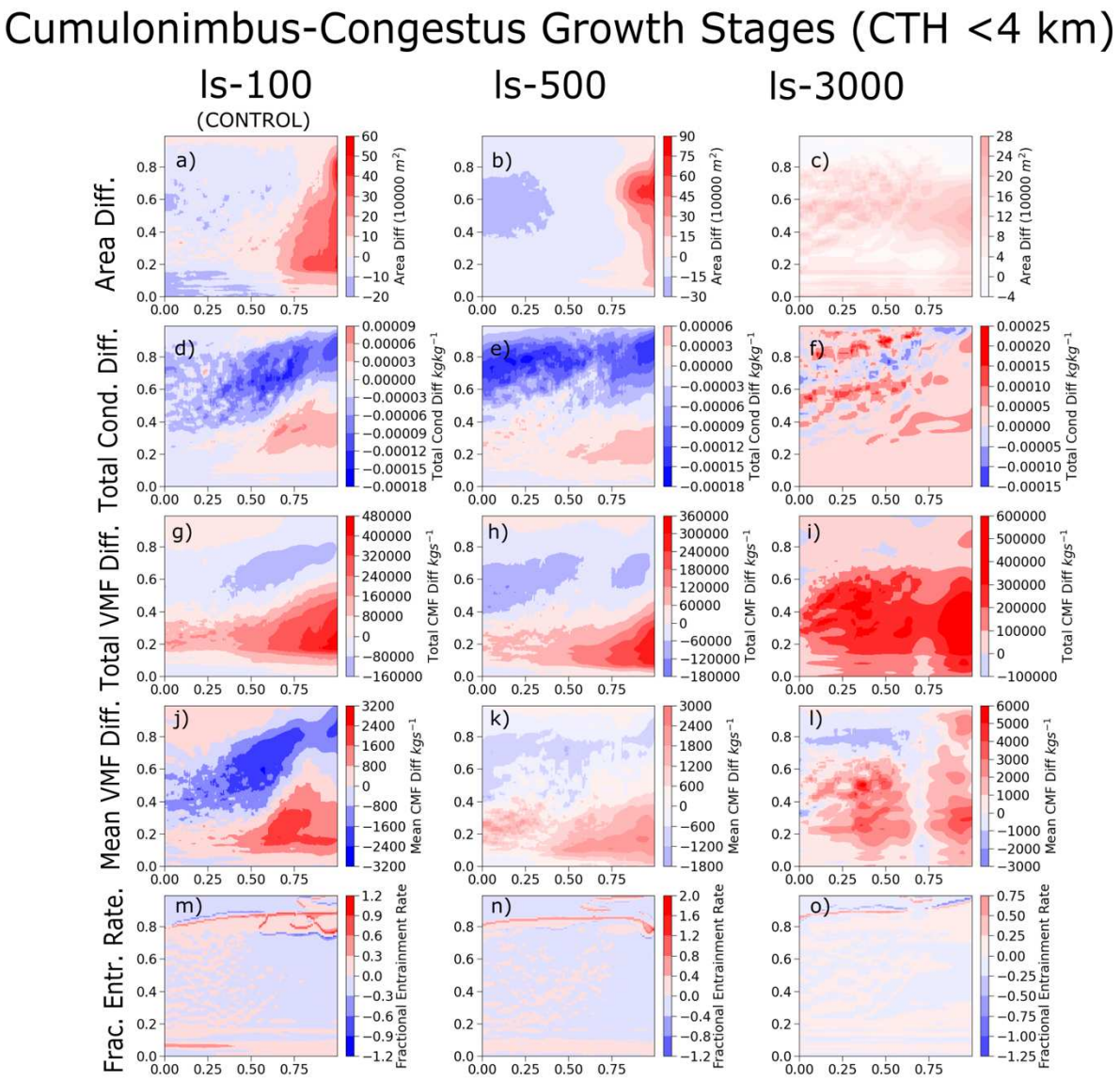

Figure 4.5: The same as Fig. 4.2, but for the cumulonimbus-congestus upscale growth differences during cumulus growth. Note the difference in colorbar scales between the different panels.

Microphysically, it is evident from the left column of both Figures 4.6 and 4.7 that changes to warm-phase microphysical processes are strongly associated with the previous cloud characteristics. Fig. 4.6a and 4.7a illustrate that terminal congestus exhibit more nucleation and condensational growth of cloud droplets, particularly early on and in the upper portion of the cloud than in the developing stages of cumulonimbus. This is collocated with enhanced drizzle

and rain number (Fig 4.6d,g) and sizes (Fig 4.7d,g) that indicate that collision-coalescence processes in terminal congestus occur both higher up in the cloud and on a faster relative timescale. Cloud, drizzle, and rain number and size enhancements in developing cumulonimbus relative to terminal congestus all occur lower in the cloud, similar to the changes in CMF, reinforcing that there are more gradual and sustained nucleation, growth, and collision-coalescence occurring lower in developing cumulonimbus, thereby indicating the importance of this process for sustained convective growth.

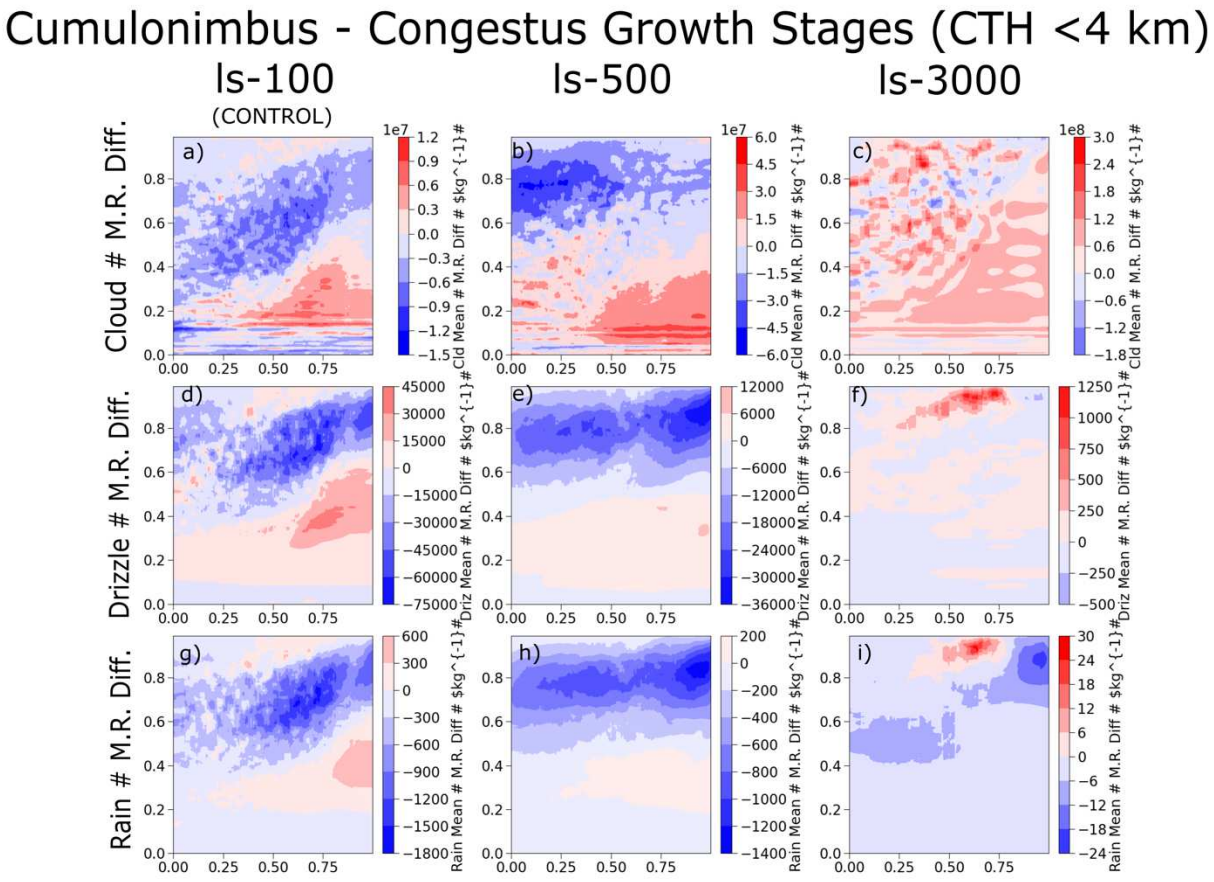

Figure 4.6: The same as Fig. 4.3, but for the cumulonimbus-congestus (cumulonimbus minus congestus) upscale growth differences during the cumulus growth stage. Note the difference in colorbar scales between the different panels.

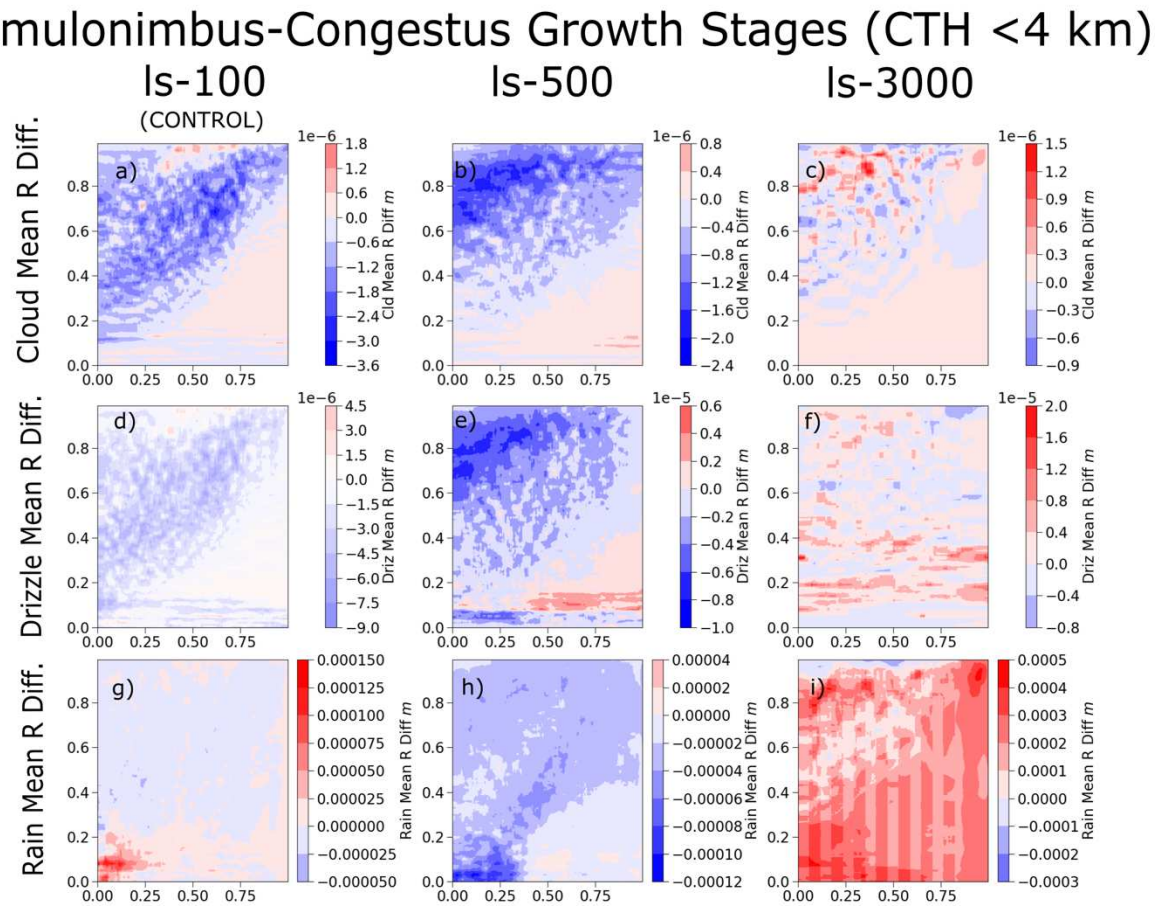

Figure 4.7: The same as Fig. 4.4, but for the cumulonimbus-congestus (cumulonimbus minus congestus) upscale growth differences during the cumulus growth stage. Note the difference in colorbar scales between the different panels.

Enhancing aerosol loading to moderate concentrations amplifies some of the cumulonimbus-congestus (cumulonimbus minus congestus) cumulus growth stage differences in a manner that is similar to how it amplified congestus-cumulus shallow growth stage differences. Condensate growth (Fig 4.5e), total CMF (Fig 4.5h), and mean CMF (Fig 4.5k) all exhibit similar cumulonimbus-terminal congestus differences as in the control simulation, though there does appear to be less variation in these differences over the growth stage. Cloud area for cumulonimbus is similarly narrower at the beginning of growth and wider at the end, but now widens the most towards the top. Providing context via the entraining plume model from

Equations 4.9 and 4.10, this increase in aspect ratio results in a more rapid decay of vertical velocity and buoyancy with height. However, unlike in terminal congestus vs cumulus, condensate loading does not concurrently increase aloft (Fig 4.5e), thus, condensate drag effects at the top of the column would be reduced relative to terminal congestus, and the layer of enhanced entrainment near cloud top is also narrower (Fig 4.5n). Examination of Figures 4.6 and 4.7 reveal that similar to the control simulation, these cumulonimbus-terminal congestus differences at moderate aerosol loading can be explained through changes in the microphysical composition of the cloud, which does not differ substantially from that of the control simulation.

High aerosol loading, however, causes a fundamental difference in the shallow growth of cumulonimbus relative to terminal congestus, as it did for terminal congestus relative to cumulus. Areal coverage is now consistently greater for developing cumulonimbus than congestus through the column (Fig 4.5c), resulting in a consistently more extreme aspect ratio than was present in congestus. In the conceptual framework of an entraining plume, (Equations 4.9, 4.10) this amplifies the decay of buoyancy and vertical velocity with height, and entrainment also seems to be slightly enhanced in these cumulonimbus clouds relative to congestus (Fig 4.5o). Developing cumulonimbus now exhibit more extensive condensate loading versus terminal congestus through much of the column (Fig 4.5f), including at the cloud top, which contrasts with our findings at other aerosol loadings. This is associated with greater total CMF (Fig 4.5i), but interestingly produces a mean CMF difference profile that exhibits similar characteristics to the congestus-cumulus mean CMF differences in Fig. 4.5g,h. For terminal congestus, we identified this to be associated with greater lofting and condensational growth of cloud droplets leading to collision-coalescence processes occurring higher in the cloud and subsequently impeding its further growth. Examining the warm-phase microphysical changes in

the right columns of Figs. 4.6 and 4.7 reinforce this argument: while the signal is somewhat mixed due to the low sample size and noise ensuing from the interpolation process, we do see an enhancement of cloud number and size aloft relative to terminal congestus (Figs. 4.6c,4.7c), resulting in an enhancement of drizzle and warm rain formation atop the column during the middle of the growth period. Similar to when we saw these processes in our congestus-cumulus comparison, this increase in collision-coalescence processes is clearly collocated with the reduction in cumulonimbus CMF relative to congestus during shallow growth.

Now that we have assessed the differences between cumulonimbus and terminal congestus while both are undergoing shallow (CTH < 4 km) growth, we turn our attention to when these populations of clouds are undergoing midlevel (4 km < CTH < 7 km) growth to assess their differences when both warm-phase and cold-phase microphysical processes may be occurring. Most of the cloud structure differences present between terminal congestus and cumulus also appear between cumulonimbus and terminal congestus, such as a wider cloud base and middle (Fig 4.8a), enhanced condensate loading through the column (Fig 4.8d), and greater total CMF (Fig 4.8g). All these changes, however, are amplified for cumulonimbus clouds, and the condensate loading enhancement exists at both lower levels and upper levels. *This indicates that for congestus to grow upscale into cumulonimbus, not only must there be enhanced vertical transport of condensate higher in the cloud, but also sustained condensate growth/formation lower in the cloud relative to terminal congestus.* Terminal congestus are also more likely to exhibit stronger mean CMF in the middle of their growth stage versus cumulonimbus, but less in initial and final stages of growth period (Fig 4.8j), and experience greater entrainment, particularly later in the simulation and higher up in the cloud (Fig 4.8m). Considering these changes in the context of our entraining plume model, these differences during the midlevel

growth phase lead to a less extreme aspect ratio in developing cumulonimbus that would promote higher values of buoyancy and vertical velocity though the column.

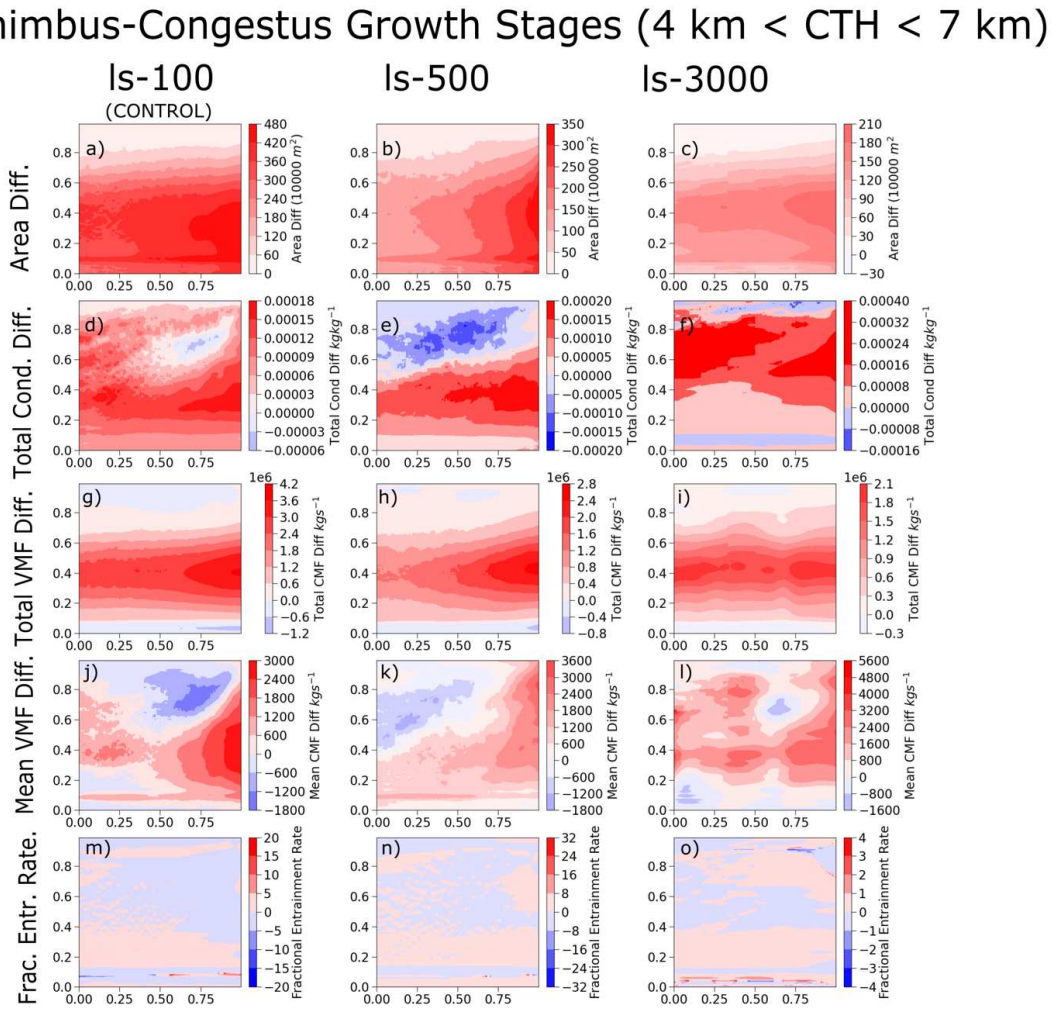

Figure 4.8: The same as Fig. 4.5, but for the cumulonimbus-congestus midlevel growth (congestus growth) stages when CTH is between 4 and 7 km. Note the difference in colorbar scales between the different panels.

Examining the changes to both warm- and cold-phase condensate species provides further reinforcement of the process findings above. In cumulonimbus midlevel growth, sustained enhancement of cloud droplet nucleation and growth at cloud base occurs relative to congestus, as well as an initial increase in droplet concentrations and size aloft (Fig 4.9a, 4.10a). This upper-level behavior in cloud droplets are also associated with increases in drizzle number

(Fig 4.9d) and size (Fig. 4.10d) in this part of the cloud, with rain concentrations (albeit not size) in these regions being suppressed relative to terminal congestus (Fig 4.9g, 4.10g). Rain and drizzle number concentrations in cumulonimbus are also greater in the lower half of the cloud (Fig 4.9d,g Fig. 4.10d), with strong increases in drizzle size at low levels and rain sizes aloft. This may indicate that drizzle growth is promoted in the low-levels due to collection of small, freshly nucleated cloud drops, while rain sizes aloft may be increased by collection of larger, lofted cloud droplets and drizzle. As discussed previously, these changes to warm-phase microphysics suggest that sustained condensational growth and collision-coalescence processes are key parts of sustaining deep convective growth. Changes to warm-phase microphysics are also likely to impact the glaciation and growth of ice condensate (Fig. 4.11-4.12).

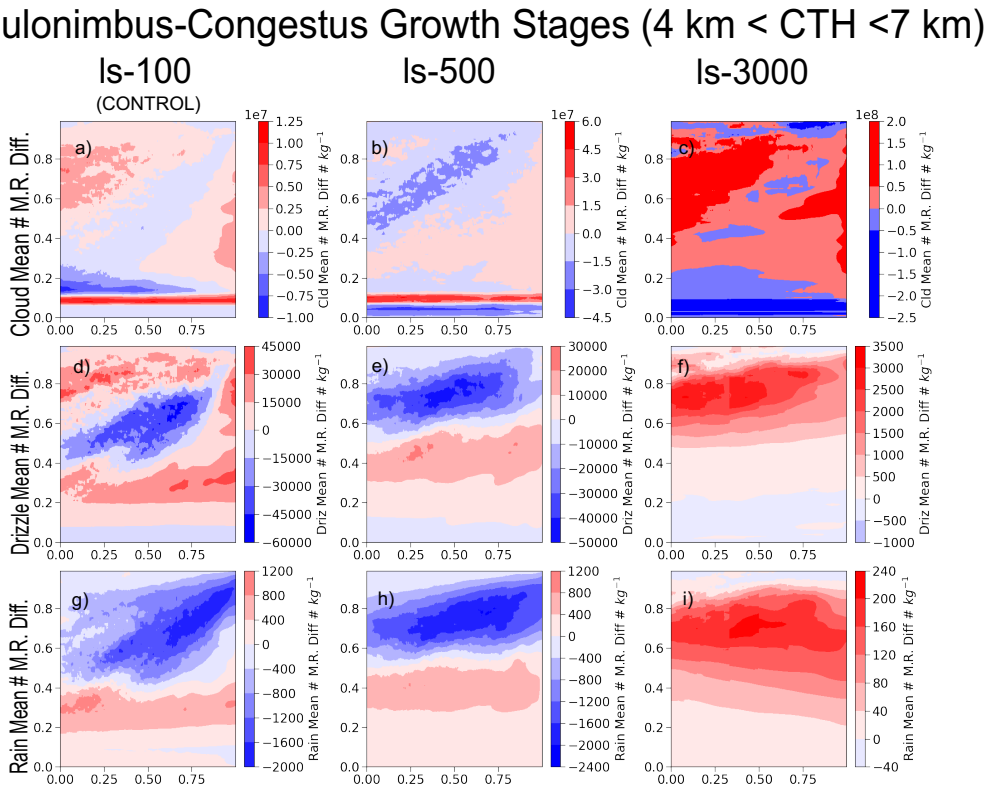

Figure 4.9: The same as Fig. 4.6, but for the cumulonimbus-congestus midlevel growth stages when CTH is between 4 and 7 km. Note the difference in colorbar scales between the different panels.

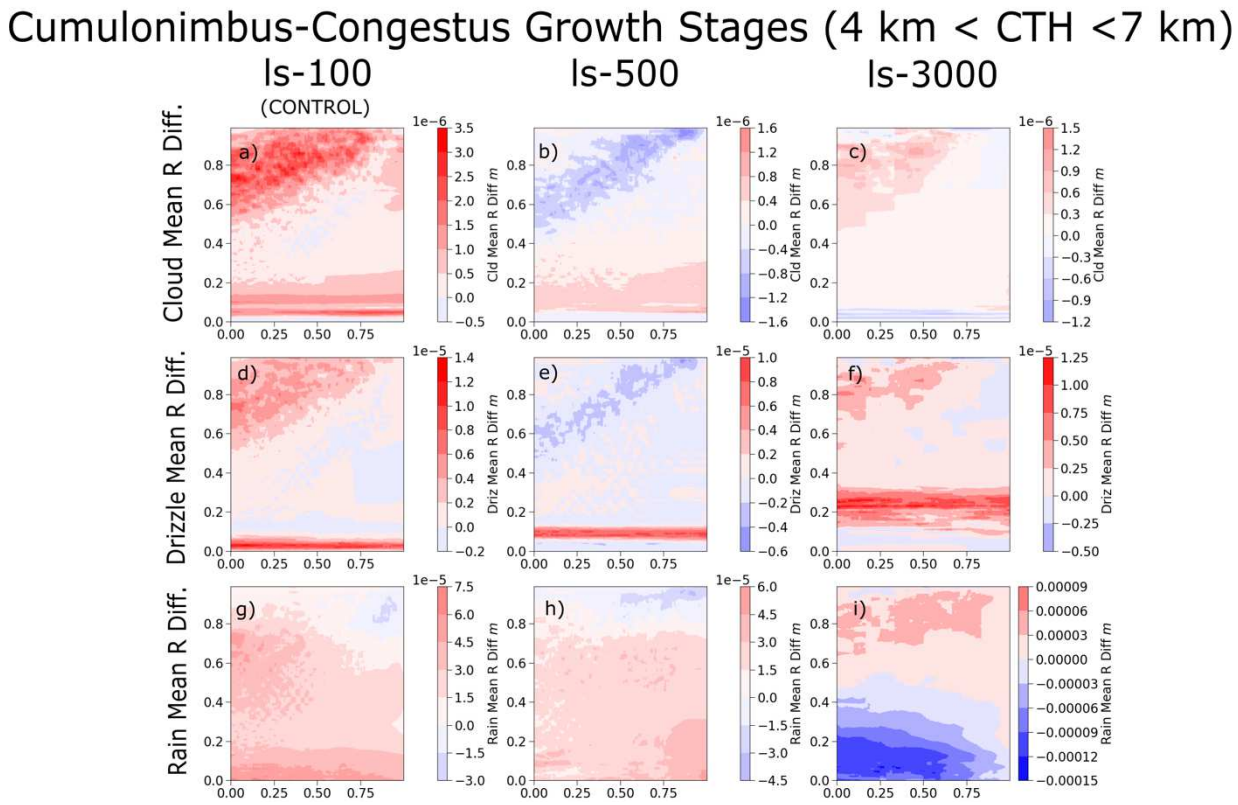

Figure 4.10: The same as Fig. 4.7, but for the cumulonimbus-congestus midlevel growth stages when CTH is between 4 and 7 km. Note the difference in colorbar scales between the different panels.

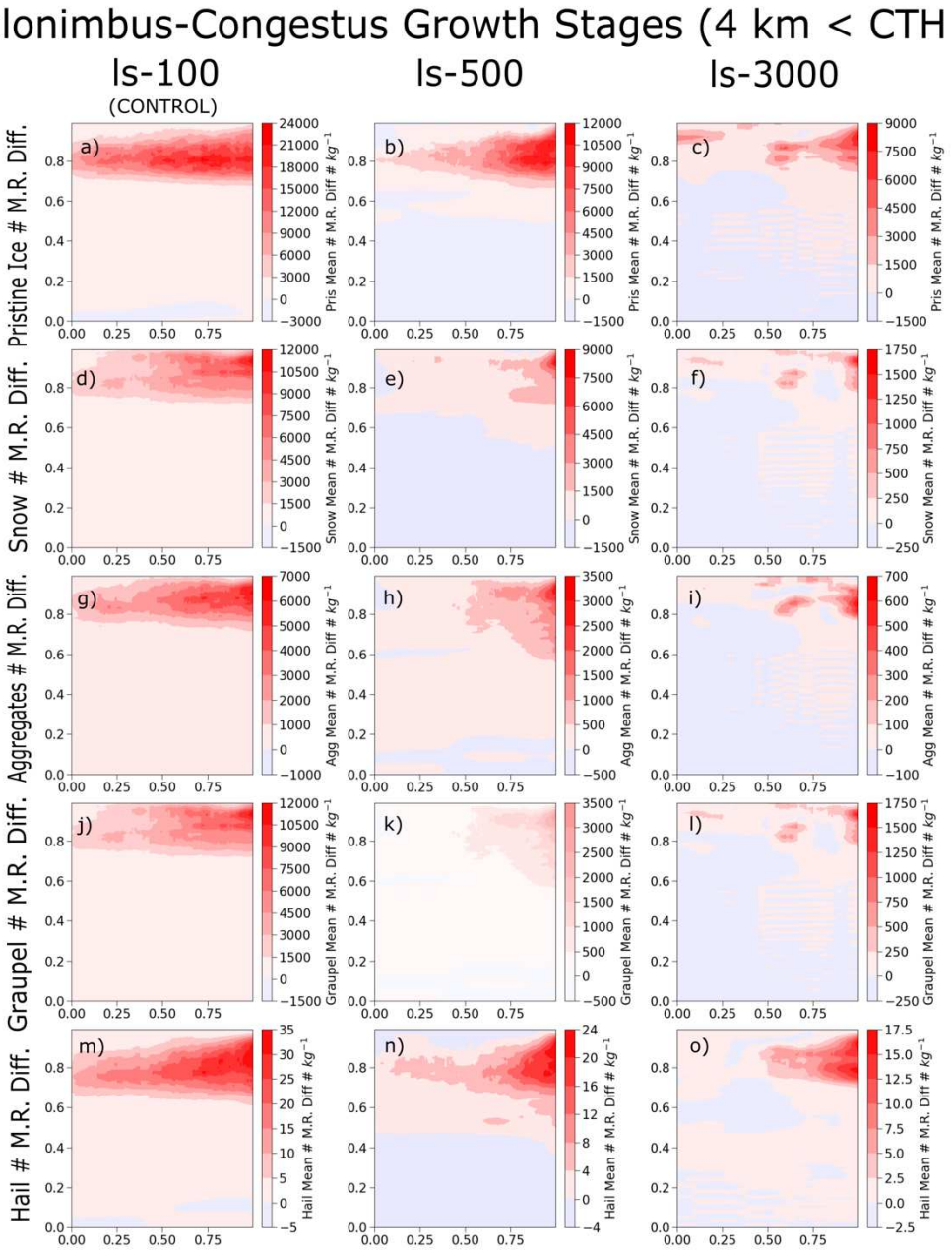

Figure 4.11: The same as Fig. 4.9, but for the ice condensate species – from top to bottom, these include pristine ice, snow, aggregates, graupel, and hail. Note the difference in colorbar scales between the different panels.

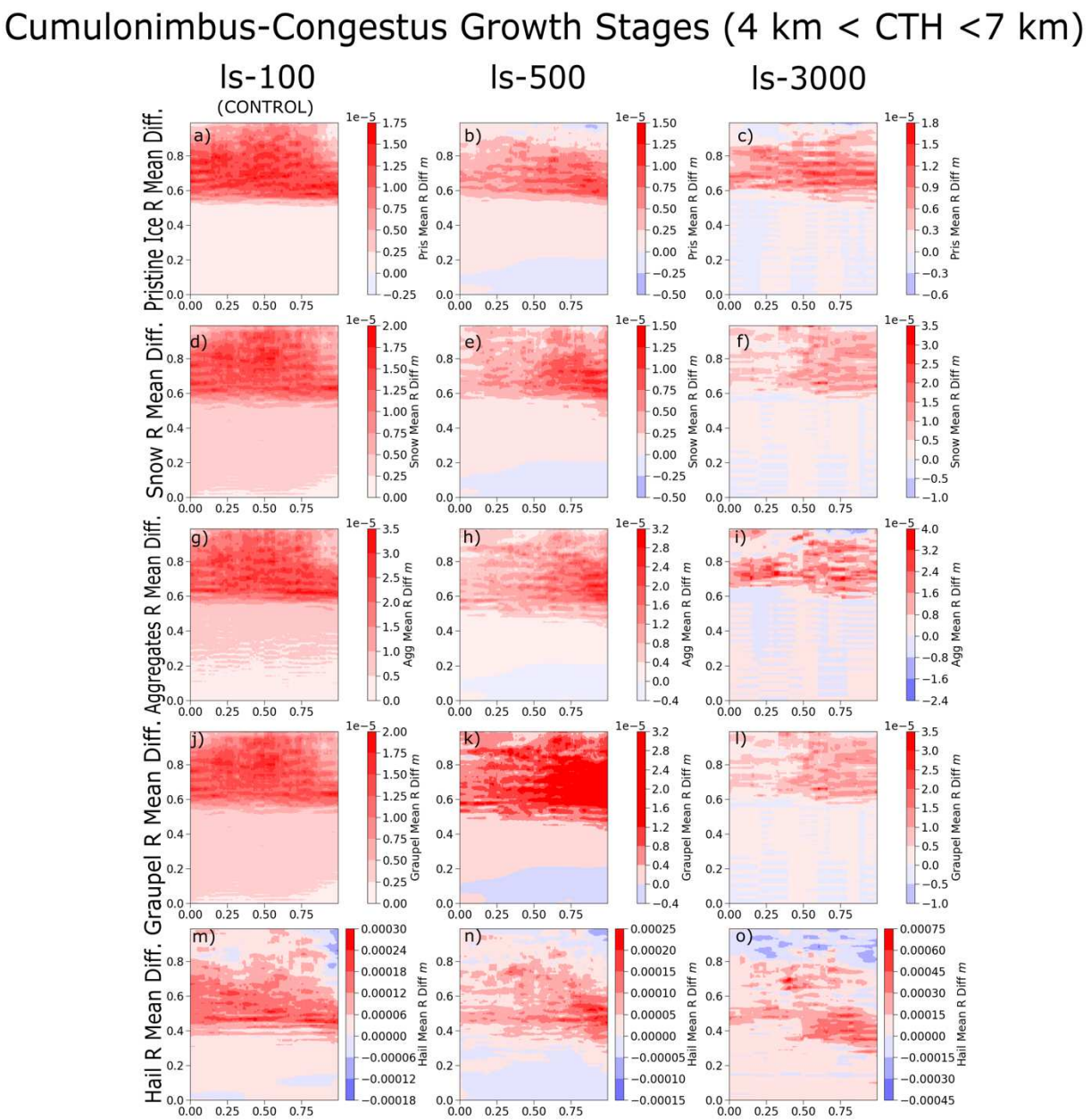

Figure 4.12: The same as Fig. 4.11, but for the ice condensate species' mean radii. Note the difference in colorbar scales between the different panels.

The left columns of Figs. 4.11 and 4.12 illustrate that the mid-level growth processes within cumulonimbus clouds overwhelmingly exhibit greater glaciation than the corresponding processes within terminal congestus clouds. While we do not calculate the process rate changes here, concentrations of pristine ice (Fig. 4.11a) and snow (Fig. 4.11d) increase near the top of the

column as the increase in lofted cloud water and drizzle in this region becomes shallower and more concentrated towards cloud top in time. This finding suggests that in cumulonimbus, the lofting of these particles during the midlevel growth stage strongly contributes to the development of ice, whereas lofting these particles relatively high in the cloud during the shallow growth stage does not, and also speaks to the importance of the time scale of convective growth. *The continued increase in all ice species over the course of midlevel growth (Fig. 4.11, left column) further indicates the need for sustained ice formation in the upper levels (top 20-40% of the cloud) of developing cumulonimbus to ascend past terminal congestus.* Ice particle size differences between congestus and cumulonimbus, however, show little temporal variation and except for hail (Fig. 4.12m) are generally split vertically with greater enhancements in size above the cloud's halfway point, and lesser enhancements below (Fig. 4.12, left column). This simply speaks to more effective ice formation and growth processes in cumulonimbus, and more effective hail growth processes in the middle of these clouds (though we cannot say whether this is greater dry growth, wet growth, or some synergy between the two growth modes).

Moderately increasing the aerosol loading produces similar cumulonimbus-congestus differences for midlevel growth as was seen in shallow growth. The areal coverage exhibits greater increases higher up in the cloud (Fig 4.8b), resulting in a more extreme aspect ratio and subsequently a greater vertical decay of vertical velocity and buoyancy. Concurrently, the enhancement of condensate loading is limited to the low and mid-levels of the cloud (Fig 4.8e), with a reduction aloft indicating that developing terminal congestus tops are more heavily loaded with condensate than developing cumulonimbus, increasing condensate loading drag atop terminal congestus to a greater extent than cumulonimbus. The midlevel increases in total CMF and mean CMF (Figs. 4.8h,k, respectively) also reflect that cumulonimbus vertical mass flux

becomes increasingly stronger and deeper over time relative to terminal congestus. The warm-phase microphysical properties seen in Figs. 4.9 and 4.10 seem to be associated most strongly with these changes: Fig 4.9b shows that cumulonimbus in the moderate aerosol environment do not exhibit the same enhanced lofting and nucleation of cloud drops aloft seen in the low aerosol environment (Fig 4.9a). Instead, cloud droplet number and size differences are increased more in the lower portion of the cloud, with these differences increasing in depth and magnitude over time. The enhanced drizzle formation aloft is also absent in Figs. 4.9e and 4.10e, with drizzle enhancements and reductions now more closely mirroring those of rain (Figs. 4.9h,4.10h). Rain drop size and number differences as a function of height and time are largely unchanged relative to the control (Figs. 4.9h,4.10h), suggesting that the changes to cloud and drizzle drop properties play a more important role in the context of aerosol convective invigoration.

Ice number and size across all species are generally suppressed at moderate aerosol loading (Figs 4.11 and 4.12, center column), though the temporal trend in ice number differences (Fig 4.11, center column) is especially interesting to consider along with the changes to cloud and drizzle processes aloft. It appears from contrasting these changes that the relative inhibition of lofting cloud and drizzle droplets at moderate aerosol loading delays ice processes at the top of the cloud, particularly regarding snow, aggregate, and graupel formation (Fig 4.11e,h,k). *Since the moderate aerosol loading results in more congestus and cumulonimbus clouds (Table 4.1), the promotion of midlevel warm-phase condensate growth over earlier lofting and freezing of liquid condensate seems to facilitate deeper and more vigorous convection.* Ice species also exhibit more growth in time over the course of the midlevel growth stage of cumulonimbus at higher aerosol loading (Fig 12, center column), which in conjunction with the previous finding, suggests that suppression of earlier ice nucleation may lead to greater vapor depositional growth

of ice later in the growth period. If true, this would result in greater latent heat release towards the top of a cumulonimbus cloud later in its midlevel growth stage, which would be expected to promote continued upscale growth.

For high amounts of aerosol loading, however, changes to cloud structure do not appear to favor deep convective growth. The aspect ratio becomes even more extreme (Fig. 4.8c), which leads to a more rapid decay of buoyancy and vertical velocity in the framework of the entraining plume model. Condensate loading is also much more concentrated towards cloud top (Fig 4.8f), which increases condensate drag at the top of the growth column. Examining the microphysical species' properties illustrates that cloud drops, drizzle, and rain are all larger and more concentrated in the upper portion of cumulonimbus than in terminal congestus (Fig 4.9, 4.10, right column). This indicates a shift in the location of collision-coalescence processes, which are concentrated towards both the bottom and top of the column in the low aerosol environment (Fig 4.9, 4.10, left columns) and towards the middle of the column at moderate aerosol loading (Fig 4.9,4.10, center column), towards being at the very top of the column at high aerosol loading. In combination with the entraining plume model predicting a more rapid decay of buoyancy and vertical velocity with height, it is possible that the displacement of collision-coalescence processes higher in the column further degrades cloud top buoyancy and strongly inhibits deeper convective growth in the high aerosol loading scenario. Ice number concentration is also suppressed and more intermittent at high aerosol loading (Fig 4.11, right column), suggesting that the enhancement of collision-coalescence processes aloft may impede liquid condensate from glaciating. What particles do glaciate are either larger to begin with or quickly grow larger than the cumulonimbus-congestus differences at low or moderate aerosol loading, but do not

seem to exhibit the temporal increase in size differences seen at moderate aerosol loading (Fig. 4.12, right column).

Ultimately, these results indicate that the changes to warm-phase microphysical processes, cloud structure, and the dynamics ensuing from their interaction are a delicate balancing act where upscale growth of convection is concerned. The interplay of plume structure, condensate loading, entrainment, and collision-coalescence processes are most suitable for cumulonimbus growth and sustenance when clouds exhibit relatively little change in area with height, vigorous collision-coalescence occurs in the cloud midlevels, and liquid condensate is lofted relatively late in the growth stage. When the cloud grows rapidly in the vertical, the aspect ratio is too extreme, and the cloud is very top-heavy with liquid condensate overall, the combination of its dynamic plume structure and relatively elevated location of large condensate particles and collision-coalescence processes inhibit the subsequent development of deeper convection. These warm-phase impacts and their feedbacks from high aerosol loading are also seen in terminal congestus clouds growing upscale from shallow cumulus and inhibit the upscale growth of these clouds as well.

4.4) Conclusions

In this study, we examined a set of LES model runs of tropical trimodal convection where initial aerosol loading was varied to understand the impacts of AIEs on the upscale growth of convection. These simulations were analyzed using the new *tobac v1.5* Python package, which is uniquely able to detect, discretize, and track these clouds in 3D space and in time, as well as properly interpret the model PBCs. Our findings from this study resulted in two key conclusions regarding aerosol impacts on tropical convective upscale growth.

First and foremost, the interaction between aerosol-induced warm-phase microphysical changes and cloud dynamics (i.e., where changes in condensate processes occur in the cloud, and how the cloud dynamics move different condensate species around) is the single most important factor in determining whether the cold-phase microphysics essential to deep convective development are enhanced or suppressed. *We saw from our results that when aerosol-microphysical-dynamical interactions lead to collision-coalescence occurring primarily in the middle of the cloud and to less lofting of cloud and drizzle droplets, these changes were associated with a delayed but seemingly more vigorous ice growth process in the upper portion of developing cumulonimbus clouds.* However, when the cloud is initially more top-heavy with liquid condensate of all species, ice formation mostly occurs in this region, which ultimately weighs the cloud down through condensate loading, thereby inhibiting deeper convection. Strongly increasing the aerosol loading leads to a rapid lofting of condensate concentrated towards the top of the cloud, while moderately increasing aerosol loading delayed the lofting seen in the control simulation in such a way as to promote later deep convective development. These findings are in keeping Igel and van den Heever (2021) and Marinescu et al. (2021) who have similarly identified that warm-phase invigoration by aerosol plays a key role in storm dynamics and whether cold-phase invigoration or enervation occurs. Our results also extend these previous studies by offering additional insights into the process links between microphysics and dynamics, particularly concerning the time evolution of these interactions.

Second, the upscale growth of convection is governed by a highly complex interplay of aerosol, microphysical, thermodynamic, and dynamic processes, and *it appears from our results that the timing of these various processes is especially crucial.* As discussed in Section 4.4.3, we found that the formation and lofting of cloud drops and drizzle play especially significant roles in

the upscale growth of cumulonimbus. Moderately increasing aerosol loading weakly suppressed this process initially, but led to later, more vigorous CMF and greater ice growth at the top of the column. Strongly increasing aerosol resulted in greater initial transport of condensate and condensate loading aloft, but this inhibited development later on in the growth stage.

Thus, studies on aerosol convective invigoration must consider all of these processes, their effective timescales, and the location and timing of occurrence in tandem to capture an accurate picture of aerosol effects on different modes of convection. Considering any of these changes in isolation (such as through parcel model or 2D kinematic model studies) or neglecting to track the evolution of these clouds through time cannot possibly capture all of the key interactions occurring throughout space and time identified within this study.

These findings reinforce those from earlier studies (e.g. Lebo and Seinfeld 2011; Lebo et al. 2012; Tao et al. 2012; Storer and van den Heever 2013; Grabowski and Morrison 2020) suggesting a delicate balancing act between aerosol, microphysical, dynamic, and thermodynamic processes. However, unlike these earlier studies, we are now able to capture the actual process **evolution** across all three modes of tropical convection in three dimensions thanks to *tobac v1.5*. It is our hope that the availability of this new tool, and our key findings in this study, facilitate and inspire future work from researchers of aerosol-cloud interactions. Our study was conducted in a modeled LES domain with substantial vertical wind shear that was also very dry above 12 km, thus, researchers examining different convective environments may find that the interplay of the processes discussed above are not universally consistent. Entrainment effects may be altered dramatically in an unsheared or differently sheared environment, and the use of more sophisticated ice growth parameterizations that incorporate variable surface attachment

kinetics (e.g. Harrington et al. 2021) may also manifest different glaciation feedbacks. We welcome the pursuit of these research avenues and comparisons to our findings.

CHAPTER 5 – CONCLUSIONS

5.1) Overarching Conclusions

Convective clouds exist around the globe, but those in the tropics are particularly important due to their near-constant presence, their roles in vertical and poleward transport of heat and moisture (which in turn drives the global Hadley Cell circulation), and their characteristic trimodal distribution of cumulus, congestus, and cumulonimbus clouds. Despite decades of research on tropical convection, many pressing science questions remain as to the mechanisms behind their upscale growth from shallow to deep convection; how they will respond to ongoing and future changes in the Earth's climate; and the integrated effects of different amounts of aerosol loading on convective environments producing both shallow and deep clouds.

Three studies presented in this dissertation address some of these lingering questions while also providing new tools for future researchers to continue advancing our understanding of tropical convective clouds. The overarching goals in this dissertation were to (1) perform bulk analyses of the trimodal distribution and its convective environment's sensitivities to low-level static stability and aerosol; (2) enhance the existing *tobac* Python library to enable detection, discretization, and tracking of a wide variety of observed and modeled 3D meteorological phenomena that were not possible before and which were necessary to achieve goal (3); and (3) use the new version of *tobac* to analyze the upscale growth of convection and its sensitivities to aerosol loading at a process (rather than bulk analysis) level. The first and third goals were achieved using the same suite of idealized RAMS simulations of trimodal convection (although

the latter uses a subset of these model runs), while the second was achieved through adding a series of both scientific and performance enhancements to *tobac*.

In the first study, presented in Chapter 2, the science question we sought to address was "how do independently and simultaneously varying initial low-level thermodynamic and aerosol properties affect the evolution of the bulk environment and the nature of the three modes of the tropical convective cloud distribution?". We utilized a suite of LES model experiments which covered two full diurnal cycles and covaried the initial thermodynamic and aerosol conditions. We subsequently conducted bulk analyses of both environmental characteristics (e.g. stability, radiative transfer, and cloud coverage) and amalgamated properties of each mode (e.g. vertical mass fluxes, mean condensate loading, and moist static energy) in the trimodal distribution. Five different conclusions were ascertained regarding the sensitivities of both the bulk mesoscale environment and its convective cloud production:

1. Large amounts of aerosol loading and low-level static stability suppress the bulk convective environment and the intensity and coverage of convective clouds.
2. Cloud and environmental responses to aerosol loading tend to be stronger than those from static stability.
3. The effects of aerosol and stability perturbations modulate each other substantially.
4. The deepest convection and highest dynamical intensity occur at moderate aerosol loading, rather than at low or high aerosol loading.
5. Most of the strongest feedbacks due to aerosol and stability perturbations are seen in the boundary layer, though some are stronger above the freezing level.

These findings provided us with new insights as to the myriad of sensitivities inherent in both tropical convective clouds and their formative environment. However, they also speak to

the nonlinearity of these feedbacks, particularly in the context of increased aerosol loading, which spawned further questions on what actual processes are impacting convective upscale growth as a function of aerosol loading. We pursued this as a follow-up study, but quickly realized that a tool capable of performing this kind of study did not exist at the time – in order to perform this investigation, we needed a robust tracking tool capable of identifying 3D cloud features and tracking them across model periodic boundaries. This is what inspired us to pursue the work discussed in Chapter 3.

For Chapter 3, our primary science question was "How can a previously existing tool, the Tracking and Object-Based Analysis of Clouds (*tobac*) Python package, be enhanced to enable its use with a wider breadth of science questions, larger datasets, and more complex atmospheric structures than it was capable of doing before?". This question arose since we could not find any tools that were capable of detecting, tracking, and analyzing a modeled cloud field varying in all three spatial dimensions, especially when the model used periodic boundaries. Most of the tools that did exist were also computationally expensive, which was also an impediment since the high-resolution LES model fields we wanted to analyze are on the order of several TB and would have taken many weeks to process with existing tools .We assessed the above science question primarily through an expansion of capabilities to work with 3D data and include a spectral filtering tool, as well as procedural enhancements such as computational optimization, the ability to regrid data, and a treatment to properly interpret periodic boundaries in data. Beyond these code changes, we also included extensive testing and demonstrations of *tobac* with new datasets that earlier versions of *tobac* would have had difficulty processing. The conclusions ensuing from our *scientific* enhancements were:

1. *tobac* has a better ability to capture the spatiotemporal evolution of clustered phenomena that are difficult to isolate in 2D projections of 3D data.
2. The new spectral filtering method allows users to isolate specific frequencies of interest in the data they are using, precluding the need for external data processing or the use of datasets that have already been smoothed.

Additionally, the conclusions from our *procedural* improvements were:

1. Computational efficiency improvements on the order of 100 to 1,000,000 times allow users to leverage higher resolution data and overall larger datasets than *tobac* could reasonably manage previously.
2. The new data regridding procedures facilitate the combined use of multiple different datasets existing on different grids.
3. The capability to recognize and robustly address periodic boundary conditions (PBCs) has also widened the utility of *tobac* by enabling its use with applicable model and even observational data, such as Global Precipitation Measurement (GPM) data

The findings in this chapter illustrate that we now have an extremely powerful and efficient cloud tracking tool in *tobac* v1.5 that can be used for a wide variety of scientific pursuits. As a result of developing this tool, we were now able to conduct the process-focused upscale growth study that was inspired by the bulk analysis study from Chapter 2.

Finally, the study discussed in Chapter 4 sought to understand the processes driving the upscale growth from cumulus to congestus and congestus to cumulonimbus, as well as how aerosol impacts modify this upscale growth transition. In this work, we focused on a subset of the simulations in Chapter 2 where only the aerosol loading was varied. Using *tobac* v1.5, we detected, discretized, and tracked maxima in total condensate mixing ratio, which was used to

examine cumulus-to-congestus and congestus-to-cumulonimbus upscale growth differences over the 6-hour period when convection was at its most active. This study revealed that:

1. The interplay between aerosol-induced changes to warm-phase microphysics (particularly collision-coalescence processes) and cloud dynamics are the most important elements for the invigoration of convective growth.
2. How these changes affect the timescales of different processes' evolution is especially crucial to this interplay between warm-phase microphysics and cloud dynamics.

These findings are incredibly important from the perspective of aerosol-induced convective invigoration: they illustrate that in order to assess the full battery of aerosol impacts on convection, the changes to cloud *processes and their timescales* must be considered in tandem with one another. This means that while studies utilizing snapshot or bulk perspectives can assess aerosol-induced changes to cloud microphysical, dynamic, and thermodynamic structure, and even instantaneous process rates, they have difficulty assessing the temporal changes to any of these processes (only inferring such changes), nor how these changes modulate one another, without utilizing a cloud tracking framework at high temporal resolution.

5.2) Future Work

The research advances detailed in this dissertation both motivate and enable a wealth of future studies on aerosol-induced convective invigoration. Our findings highlight that the processes contributing to upscale growth are best considered in combination rather than isolation, especially regarding any relative adjustments in the timescales of these different processes (e.g., when and where condensate lofting, collision-coalescence, and glaciation occur during the clouds' growth stages). Chapter 4 especially shows that the formation of drizzle and rain, their vertical transport, and whether/where they glaciate are crucial components to the

upscale growth of deeper convection. Thus, the aerosol impacts on collision-coalescence processes and their spatiotemporal evolution within a growing cloud must be carefully considered in the context of cloud dynamics and thermodynamics, as well as the timescale of different processes contributing to convection, to understand whether an increase in aerosol loading will promote or inhibit deep convective development.

The implications of the results in Chapters 2 and 4 specifically inform new research avenues on spatial scales ranging from those of individual convective clouds to entire scenes of convective cloud populations and/or systems. In the long term, climate modeling will be greatly improved once processing power and memory advances are sufficient to run global cloud-resolving or LES modeling studies. However, in the short term, advances in the convective parameterizations used by climate models are needed. Utilizing the findings of our research with cutting-edge methodologies like Machine Learning approaches could improve convective parameterizations greatly, particularly regarding the identification of microphysical and thermodynamic patterns which accompany glaciation processes and other nonlinear feedbacks occurring within clouds. Additionally, using *tobac*, maxima in individual microphysical, dynamical, and thermodynamical process rates can be detected and tracked to gain an even deeper understanding of the mechanics behind convective upscale growth and aerosol convective invigoration. While we do examine these processes in Chapter 4, they can be even better understood by explicitly detecting and tracking on the temporally evolving process rates themselves. Such approaches are informative for individual convective clouds as well as larger cloud clusters and systems including mesoscale convective systems and tropical cyclones, which are complex thermodynamic engines driven by multifaceted interactions between large- and small-scale processes.

Beyond the new research motivations on clouds and cloud systems that our results provide, the upgrades to *tobac* as a part of *tobac* v1.5 also enable a vast new breadth of process-focused studies in atmospheric science and beyond. Procedurally, the advances in computational speed alone allow the use of far larger datasets than *tobac* could reasonably handle before, with datasets on the order of 100 TB now needing only hours or days to process instead of weeks. As model and observational dataset sizes steadily grow larger, it is increasingly important for data analysis tools to be able to process Big Data efficiently. The new data regridding procedure allows *tobac* to natively combine analyses based on datasets existing on different grids. For example, satellite-derived wind data could now be used in conjunction with gridded observations of dust concentrations to detect and track dust advection. Additionally, the PBC treatment not only allows for use with PBC model data (commonly used in idealized studies), but also enables use of *tobac* in global observational data with zonal cyclic boundaries, such as GPM data, and represents the first step towards the inclusion of truly global tracking in this tool.

Scientifically, the inclusion of fully 3D data processing allows for the use of *tobac* with highly complex 3D meteorological structures, such as layered clouds; vertically sheared cloud systems (e.g., squall lines); and heavily polluted environments with multiple aerosol layers. It can also be used with non-meteorological data (provided it is gridded), for example, locating and tracking populations of migratory birds equipped with radio trackers (e.g., Crewe et al. 2020). The new spectral filtering tool also provides *tobac* with the capabilities to isolate phenomena such as synoptic- or planetary-scale atmospheric waves from data with mesoscale or sub-mesoscale noise (e.g., finely resolved wind fields) without requiring users to use external tools for data processing. On the whole, it is plainly evident that the uses discussed in the previous two paragraphs only cover a handful of the nearly endless research possibilities that *tobac* v1.5

enables. Any future advances to *tobac*, such as the inclusion of split and merger processing that is planned for an upcoming release, expand the power of this unique tool even further.

REFERENCES

Albrecht, B. A., 1989: Aerosols, Cloud Microphysics, and Fractional Cloudiness. *Science*, **245**.

Allan, D. B., T. Caswell, N. C. Keim, C. M. van der Wel, and R. W. Verweij, 2021: *soft-matter/trackpy: Trackpy v0.5.0*.

Altaratz, O., I. Koren, Y. Yair, and C. Price, 2010: Lightning response to smoke from Amazonian fires. *Geophys. Res. Lett.*, **37**, https://doi.org/10.1029/2010gl042679.

Altaratz, O., I. Koren, L. A. Remer, and E. Hirsch, 2014: Review: Cloud invigoration by aerosols—Coupling between microphysics and dynamics. *Atmos. Res.*, **140–141**, 38–60.

Anber, U. M., S. Wang, P. Gentine, and M. P. Jensen, 2019: Probing the Response of Tropical Deep Convection to Aerosol Perturbations Using Idealized Cloud-Resolving Simulations with Parameterized Large-Scale Dynamics. *J. Atmos. Sci.*, **76**, 2885–2897.

Andreae, M. O., D. Rosenfeld, P. Artaxo, A. A. Costa, G. P. Frank, K. M. Longo, and M. A. F. Silva-Dias, 2004: Smoking rain clouds over the Amazon. *Science*, **303**, 1337–1342.

Arakawa, A., and W. H. Schubert, 1974: Interaction of a Cumulus Cloud Ensemble with the Large-Scale Environment, Part I. *J. Atmos. Sci.*, **31**.

——, and V. R. Lamb, 1977: Computational Design of the Basic Dynamical Processes of the UCLA General Circulation Model. *Methods in Computational Physics: Advances in Research and Applications*, J. Chang, Ed., Vol. 17 of, Elsevier, 173–265.

Atwood, S. A., and Coauthors, 2017: Size-resolved aerosol and cloud condensation nuclei (CCN) properties in the remote marine South China Sea – Part 1: Observations and source classification. *Atmos. Chem. Phys.*, **17**, 1105–1123.

Benedict, J. J., and D. A. Randall, 2007: Observed Characteristics of the MJO Relative to Maximum Rainfall. *J. Atmos. Sci.*, **64**, 2332–2354.

Betts, A. K., 1973: A Composite Mesoscale Cumulonimbus Budget. *J. Atmos. Sci*.

Bukowski, J., and S. C. van den Heever, 2021: Direct radiative effects in haboobs. *J. Geophys. Res.*, **126**, https://doi.org/10.1029/2021jd034814.

Byers, H. R., and R. R. Braham Jr, 1948: Thunderstorm Structure and Circulation. *Journal of Meteorology*.

Charlson, R. J., and M. J. Pilat, 1969: Climate: The Influence of Aerosols. *J. Appl. Meteorol.*, **8**.

Cotton, W. R., and Coauthors, 2003: RAMS 2001: Current status and future directions. *Meteorol. Atmos. Phys.*, **82**, 5–29.

Cotton, W. R., G. H. Bryan, and S. C. van den Heever, 2011: *Storm and Cloud Dynamics*. Academic Press.

Crewe, T. L., D. Kendal, and H. A. Campbell, 2020: Motivations and fears driving participation in collaborative research infrastructure for animal tracking. *PLoS One*, **15**, e0241964.

Cruz, L. A., 1973: Venezuelan Rainstorms as Seen by Radar. *J. Appl. Meteorol.*, https://doi.org/10.1175/1520-0450(1973)012<0119:VRASBR>2.0.CO;2.

Dawe, J. T., and P. H. Austin, 2012: Statistical analysis of an LES shallow cumulus cloud ensemble using a cloud tracking algorithm. *Atmos. Chem. Phys.*, **12**, 1101–1119.

Del Genio, A. D., and W. Kovari, 2002: Climatic Properties of Tropical Precipitating Convection under Varying Environmental Conditions. *J. Clim.*, **15**, 2597–2615.

——, Y. Chen, D. Kim, and M.-S. Yao, 2012: The MJO Transition from Shallow to Deep Convection in CloudSat/CALIPSO Data and GISS GCM Simulations. *Journal of Climate*, **25**, 3755–3770.

DeMott, P. J., and Coauthors, 2010: Predicting global atmospheric ice nuclei distributions and their impacts on climate. *Proc. Natl. Acad. Sci. U. S. A.*, **107**, 11217–11222.

Dixon, M., and G. Weiner, 1993: TITAN: Thunderstorm Identification, Tracking, Analysis, and Nowcasting - a Radar-based Methodology. *J. Atmos. Ocean. Technol.*, **10**.

Drager, A. J., and S. C. van den Heever, 2017: Characterizing convective cold pools. *J. Adv. Model. Earth Syst.*, **9**, 1091–1115.

——, L. D. Grant, and S. C. van den Heever, 2020: Cold pool responses to changes in soil moisture. *J. Adv. Model. Earth Syst.*, **12**, https://doi.org/10.1029/2019ms001922.

Emanuel, K. A., 1994: *Atmospheric Convection*. Oxford University Press.

Fan, J., and Coauthors, 2009: Dominant role by vertical wind shear in regulating aerosol effects on deep convective clouds. *J. Geophys. Res.*, **114**, https://doi.org/10.1029/2009jd012352.

Feingold, G., B. Stevens, W. R. Cotton, and A. S. Frisch, 1996: The Relationship between Drop In-Cloud Residence Time and Drizzle Production in Numerically Simulated Stratus Clouds. *J. Atmos. Sci.*, **53**.

Feng, Z., S. Hagos, A. K. Rowe, C. D. Burleyson, M. N. Martini, and S. P. Szoeke, 2015: Mechanisms of convective cloud organization by cold pools over tropical warm ocean during the AMIE/DYNAMO field campaign. *J. Adv. Model. Earth Syst.*, **7**, 357–381.

Freeman, S. W., S. C. van den Heever, J. S. Reid, and D. J. Posselt, 2019: Tropical Deep Convective Morphology in the Different Thermodynamic and Aerosol Environments of CAMP2Ex and PISTON. Oral presentation at 2019 American Geophysical Union Fall Annual meeting, December 2019, San Francisco, CA, USA.

——, ——, D. J. Posselt, and J. S. Reid, 2022: Dynamic and Thermodynamic Environmental Modulation of Tropical Deep Convection in the Maritime Continent. Accepted pending revision at *J. Atmos. Sci*.

Gambheer, A. V., and G. S. Bhat, 2000: Life Cycle Characteristics of Deep Cloud Systems over the Indian Region Using INSAT-1B Pixel Data. *Monthly Weather Review*, **128**.

Geerts, B., and Coauthors, 2018: Recommendations for In Situ and Remote Sensing Capabilities in Atmospheric Convection and Turbulence. *Bull. Am. Meteorol. Soc.*, **99**, 2463–2470.

Ghate, V. P., M. A. Miller, and P. Zhu, 2016: Differences between Nonprecipitating Tropical and Trade Wind Marine Shallow Cumuli. *Mon. Weather Rev.*, **144**, 681–701.

Gill, A. E., and E. M. Rasmusson, 1983: The 1982–83 climate anomaly in the equatorial Pacific. *Nature*, **306**, 229–234.

Grabowski, W. W., 2018: Can the Impact of Aerosols on Deep Convection be Isolated from Meteorological Effects in Atmospheric Observations? *J. Atmos. Sci.*, **75**, 3347–3363.

——, and H. Morrison, 2020: Do Ultrafine Cloud Condensation Nuclei Invigorate Deep Convection? *J. Atmos. Sci.*, **77**, 2567–2583.

Grant, L. D., and S. C. van den Heever, 2014: Aerosol-cloud-land surface interactions within tropical sea breeze convection. *J. Geophys. Res.*, **119**, 8340–8361.

Gropp, M. E., and C. E. Davenport, 2021: Python-Based Supercell Tracking for Coarse Temporal and Spatial Resolution Numerical Model Simulations. *J. Atmos. Ocean. Technol.*, **38**, 1551–1559.

Harrington, J. Y., 1997: The Effects of Radiative and Microphysical Processes on Simulated Warm and Transition Season Arctic Stratus. Ph.D. dissertation, Colorado State University, 278 pp.

——, G. A. Sokolowsky, and H. Morrison, 2021: Semi-Analytic Functions to Calculate the Deposition Coefficients for Ice Crystal Vapor Growth in Bin and Bulk Microphysical Models. *J. Atmos. Sci.*, https://doi.org/10.1175/jas-d-20-0307.1.

Harrop, B. E., and D. L. Hartmann, 2015: The Relationship between Atmospheric Convective Radiative Effect and Net Energy Transport in the Tropical Warm Pool. *J. Clim.*, **28**, 8620–8633.

Heikenfeld, M., P. J. Marinescu, M. Christensen, D. Watson-Parris, F. Senf, S. C. van den Heever, and P. Stier, 2019: Tobac 1.2: Towards a flexible framework for tracking and analysis of clouds in diverse datasets. *Geosci. Model Dev.*, **12**, 4551–4570.

Hersbach, H., and Coauthors, 2018: ERA5 hourly data on pressure levels from 1979 to present. *Copernicus Climate Change Service (C3S) Climate Data Store (CDS)*, https://doi.org/10.24381/cds.bd0915c6.

Heus, T., and A. Seifert, 2013: Automated tracking of shallow cumulus clouds in large domain, long duration large eddy simulations. *Geosci. Model Dev.*, **6**, 1261–1273.

Heus, T., H. J. J. Jonker, H. E. A. Van den Akker, E. J. Griffith, M. Koutek, and F. H. Post, 2009: A statistical approach to the life cycle analysis of cumulus clouds selected in a virtual reality environment. *J. Geophys. Res.*, **114**, https://doi.org/10.1029/2008jd010917.

Heymsfield, G. M., L. Tian, A. J. Heymsfield, L. Li, and S. Guimond, 2010: Characteristics of Deep Tropical and Subtropical Convection from Nadir-Viewing High-Altitude Airborne Doppler Radar. *J. Atmos. Sci.*, **67**, 285–308.

Hilario, M. R. A., and Coauthors, 2020: Investigating size-segregated sources of elemental composition of particulate matter in the South China Sea during the 2011 Vasco cruise. *Atmos. Chem. Phys.*, **20**, 1255–1276.

Hohenegger, C., and B. Stevens, 2013: Preconditioning Deep Convection with Cumulus Congestus. *J. Atmos. Sci.*, **70**, 448–464.

Hu, J., and Coauthors, 2019: Tracking and characterization of convective cells through their maturation into stratiform storm elements using polarimetric radar and lightning detection. *Atmos. Res.*, **226**, 192–207.

Igel, A. L., and S. C. van den Heever, 2021: Invigoration or enervation of convective clouds by aerosols? *Geophys. Res. Lett.*, **48**, https://doi.org/10.1029/2021gl093804.

Igel, M. R., and S. C. van den Heever, 2015: The relative influence of environmental characteristics on tropical deep convective morphology as observed by CloudSat. *J. Geophys. Res.*, **120**, 4304–4322.

Jakob, C., G. Tselioudis, and T. Hume, 2005: The radiative, cloud, and thermodynamic properties of the major tropical western Pacific cloud regimes. *J. Clim.*, **18**, 1203–1215.

Jensen, M. P., and A. D. Del Genio, 2006: Factors limiting convective cloud-top height at the ARM Nauru Island climate research facility. *J. Clim.*, **19**, 2105–2117.

Jiang, H., and G. Feingold, 2006: Effect of aerosol on warm convective clouds: Aerosol-cloud-surface flux feedbacks in a new coupled large eddy model. *Journal of Geophysical Research*, **111**, https://doi.org/10.1029/2005JD006138.

Johnson, R. H., and X. Lin, 1997: Episodic trade wind regimes over the western pacific warm pool. *J. Atmos. Sci.*, **54**, 2020–2034.

——, T. M. Rickenbach, S. A. Rutledge, P. E. Ciesielski, and W. H. Schubert, 1999: Trimodal characteristics of tropical convection. *J. Clim.*, **12**, 2397–2418.

Khain, A., A. Pokrovsky, M. Pinsky, A. Seifert, and V. Phillips, 2004: Simulation of effects of atmospheric aerosols on deep turbulent convective clouds using a spectral microphysics

mixed-phase cumulus cloud model. Part I: Model description and possible applications. *J. Atmos. Sci.*, **61**, 2963–2982.

——, D. Rosenfeld, and A. Pokrovsky, 2005: Aerosol impact on the dynamics and microphysics of deep convective clouds. *Quart. J. Roy. Meteor. Soc.*, **131**, 2639–2663.

Khain, A. P., N. BenMoshe, and A. Pokrovsky, 2008: Factors Determining the Impact of Aerosols on Surface Precipitation from Clouds: An Attempt at Classification. *J. Atmos. Sci.*, **65**, 1721–1748.

Knight, S. M., G. M. Pitman, D. T. T. Flockhart, and D. R. Norris, 2019: Radio-tracking reveals how wind and temperature influence the pace of daytime insect migration. *Biol. Lett.*, **15**, 20190327.

Kukulies, J., D. Chen, and J. Curio, 2021: The role of mesoscale convective systems in precipitation in the Tibetan plateau region. *J. Geophys. Res.*, **126**, https://doi.org/10.1029/2021jd035279.

Lebo, Z. J., and J. H. Seinfeld, 2011: Theoretical basis for convective invigoration due to increased aerosol concentration. *Atmos. Chem. Phys.*, **11**, 5407–5429.

Lebo, Z. J., and H. Morrison, 2014: Dynamical Effects of Aerosol Perturbations on Simulated Idealized Squall Lines. *Mon. Weather Rev.*, **142**, 991–1009.

Lebo, Z. J., H. Morrison, and J. H. Seinfeld, 2012: Are simulated aerosol-induced effects on deep convective clouds strongly dependent on saturation adjustment? *Atmos. Chem. Phys.*, **12**, 9941–9964.

Lee, T. J., 1992: The Impact of Vegetation on the Atmospheric Boundary Layer and Convective Storms. Ph.D. dissertation, Colorado State University, 128 pp.

LeMone, M. A., and E. J. Zipser, 1980: Cumulonimbus Vertical Velocity Events in GATE. Part I: Diameter, Intensity and Mass Flux. *J. Atmos. Sci.*, **37**, 2444–2457.

Leung, G. R., and S. C. van den Heever, 2022: Updraft Structure and Detrainment in Transient and Terminal Congestus Clouds. Accepted pending revisions at *J. Atmos. Sci*.

Li, X., W.-K. Tao, H. Masunaga, G. Gu, and X. Zeng, 2013: Aerosol Effects on Cumulus Congestus Population over the Tropical Pacific: A Cloud-Resolving Modeling Study. *Journal of the Meteorological Society of Japan. Ser. II*, **91**, 817–833.

Li, Y., Y. Liu, Y. Chen, B. Chen, X. Zhang, W. Wang, Z. Shu, and Z. Huo, 2021: Characteristics of Deep Convective Systems and Initiation during Warm Seasons over China and Its Vicinity. *Remote Sensing*, **13**, https://doi.org/10.3390/rs13214289.

Lin, X., and R. H. Johnson, 1996: Heat, Moistening, and Rainfall over the Western Pacific Warm Pool During TOGA COARE. *J. Atmos. Sci.*, **53**.

Liu, C., and M. W. Moncrieff, 1998: A Numerical Study of the Diurnal Cycle of Tropical Oceanic Convection. *J. Atmos. Sci.*, **55**, 2329–2344.

Luo, Z., G. Y. Liu, G. L. Stephens, and R. H. Johnson, 2009: Terminal versus transient cumulus congestus: A CloudSat perspective. *Geophys. Res. Lett.*, **36**, https://doi.org/10.1029/2008gl036927.

Malkus, J. S., 1958: On the structure of the trade wind moist layer. *Papers in Physical Oceanography and Meteorology*, **13**.

Malkus, J. S., and H. Riehl, 1964: Cloud structure and distributions over the tropical Pacific Ocean. *Tellus*, **16**.

Mapes, B. E., 1993: Gregarious Tropical Convection. *J. Atmos. Sci.*, **50**.

Marinescu, P. J., P. C. Kennedy, M. M. Bell, A. J. Drager, L. D. Grant, S. W. Freeman, and S. C. van den Heever, 2020: Updraft Vertical Velocity Observations and Uncertainties in High Plains Supercells Using Radiosondes and Radars. *Mon. Weather Rev.*, **148**, 4435–4452.

——, and Coauthors, 2021: Impacts of Varying Concentrations of Cloud Condensation Nuclei on Deep Convective Cloud Updrafts—A Multimodel Assessment. *J. Atmos. Sci.*, **78**, 1147–1172.

Masunaga, H., 2012: A Satellite Study of the Atmospheric Forcing and Response to Moist Convection over Tropical and Subtropical Oceans. *J. Atmos. Sci.*, **69**, 150–167.

——, T. S. L'Ecuyer, and C. D. Kummerow, 2005: Variability in the characteristics of precipitation systems in the tropical Pacific. Part I: Spatial structure. *J. Clim.*, **18**, 823–840.

Matsui, T., S. Q. Zhang, S. E. Lang, W.-K. Tao, C. Ichoku, and C. D. Peters-Lidard, 2018: Impact of radiation frequency, precipitation radiative forcing, and radiation column aggregation on convection-permitting West African monsoon simulations. *Clim. Dyn.*, **55**, 193–213.

Maze, A., 1889: Sur la classification des nuages. *Congrés Météorologique International*, Congrés Météorologique International, 25–37.

Meyers, M. P., R. L. Walko, J. Y. Harrington, and W. R. Cotton, 1997: New RAMS cloud microphysics parameterization. Part II: The two-moment scheme. *Atmos. Res.*, **45**, 3–39.

Morrison, H., and W. W. Grabowski, 2011: Cloud-system resolving model simulations of aerosol indirect effects on tropical deep convection and its thermodynamic environment. *Atmos. Chem. Phys.*, **11**, 10503–10523.

Morrison, H., J. M. Peters, A. C. Varble, W. M. Hannah, and S. E. Giangrande, 2020: Thermal Chains and Entrainment in Cumulus Updrafts. Part I: Theoretical Description. *J. Atmos. Sci.*, **77**, 3637–3660.

Neelin, J. D., and I. M. Held, 1987: Modeling Tropical Convergence Based on the Moist Static Energy Budget. *Mon. Weather Rev.*, **115**.

Neggers, R. A. J., J. D. Neelin, and B. Stevens, 2007: Impact Mechanisms of Shallow Cumulus Convection on Tropical Climate Dynamics. *J. Clim.*, **20**, 2623–2642.

Núñez Ocasio, K. M., J. L. Evans, and G. S. Young, 2020: Tracking Mesoscale Convective Systems that are Potential Candidates for Tropical Cyclogenesis. *Mon. Weather Rev.*, **148**, 655–669.

Park, J. M., and S. C. van den Heever, 2022: Weakening of tropical sea breeze convective systems through interactions of aerosol, radiation, and soil moisture. *Atmos. Chem. Phys.*, 22, 10527–10549. https://doi.org/10.5194/acp-22-10527-2022.

Peters, J. M., H. Morrison, A. C. Varble, W. M. Hannah, and S. E. Giangrande, 2020: Thermal Chains and Entrainment in Cumulus Updrafts. Part II: Analysis of Idealized Simulations. *J. Atmos. Sci.*, **77**, 3661–3681.

Pielke, R. A., and Coauthors, 1992: A Comprehensive Meteorological Modeling System-RAMS. *Meteorol. Atmos. Phys.*, **49**, 69–91.

Plant, R. S., 2009: Statistical properties of cloud lifecycles in cloud-resolving models. *Atmos. Chem. Phys.*, **9**, 2195–2205.

Posselt, D. J., S. C. van den Heever, and G. L. Stephens, 2008: Trimodal cloudiness and tropical stable layers in simulations of radiative convective equilibrium. *Geophys. Res. Lett.*, **35**, https://doi.org/10.1029/2007gl033029.

Randall, D. A., 1980: Conditional instability of the first kind upside-down. *J. Atmos. Sci.*, **37**, 125–130.

Rangno, A. L., and P. V. Hobbs, 2005: Microstructures and Precipitation Development in Cumulus and Small Cumulonimbus Clouds over the Warm Pool of the Tropical Pacific Ocean. *Quart. J. Roy. Meteor. Soc.,* **131** (606): 639–73, http://doi.wiley.com/10.1256/qj.04.13

Rasmussen, K. L., and R. A. Houze, 2016: Convective Initiation near the Andes in Subtropical South America. *Mon. Weather Rev.*, **144**, 2351–2374.

Rauber, R. M., and Coauthors, 2007: Rain in Shallow Cumulus over the Ocean: the RICO Campaign. *Bull. Am. Meteorol. Soc.*,.

Raut, B. A., R. Jackson, M. Picel, S. M. Collis, M. Bergemann, and C. Jakob, 2021: An Adaptive Tracking Algorithm for Convection in Simulated and Remote Sensing Data. *J. Appl. Meteorol. Climatol.*, **60**, 513–526.

Reid, J. S., and J. Wang, 26-27 March 2020: Personal communication via email pertaining to characterization of sulfate aerosol properties observed during CAMP2Ex.

——, and Coauthors, 2022: The coupling between tropical meteorology, aerosol science, convection and the energy budget during the Clouds, Aerosol Monsoon Processes Philippines Experiment (CAMP2Ex). *Bull. Am. Meteorol. Soc.*,.

——, and Coauthors, 2013: Observing and understanding the Southeast Asian aerosol system by remote sensing: An initial review and analysis for the Seven Southeast Asian Studies (7SEAS) program. *Atmos. Res.*, **122**, 403–468.

——, and Coauthors, 2016a: Aerosol meteorology of the Maritime Continent for the 2012 7SEAS southwest monsoon intensive study – Part 1: regional-scale phenomena. *Atmos. Chem. Phys.*, **16**, 14041–14056.

——, and Coauthors, 2016b: Aerosol meteorology of Maritime Continent for the 2012 7SEAS southwest monsoon intensive study – Part 2: Philippine receptor observations of fine-scale aerosol behavior. *Atmos. Chem. Phys.*, **16**, 14057–14078.

Riehl, H., and J. S. Malkus, 1958: On the Heat Balance of the Equatorial Trough Zone. *Geophysica*, **6**.

Rosenfeld, D., and I. M. Lensky, 1998: Satellite–based insights into precipitation formation processes in continental and maritime convective clouds. *Bull. Am. Meteorol. Soc.*, **79**, 2457–2476.

——, U. Lohmann, G. B. Raga, C. D. O'Dowd, M. Kulmala, S. Fuzzi, A. Reissell, and M. O. Andreae, 2008: Flood or drought: how do aerosols affect precipitation? *Science*, **321**, 1309–1313.

Ruppert, J. H., Jr, and R. H. Johnson, 2015: Diurnally Modulated Cumulus Moistening in the Preonset Stage of the Madden–Julian Oscillation during DYNAMO. *J. Atmos. Sci.*, **72**, https://doi.org/10.1175/JAS-D-14-0218.1.

Saleeby, S. M., and S. C. van den Heever, 2013: Developments in the CSU-RAMS Aerosol Model: Emissions, Nucleation, Regeneration, Deposition, and Radiation. *J. Appl. Meteorol. Climatol.*, **52**, 2601–2622.

——, S. R. Herbener, S. C. van den Heever, and T. L'Ecuyer, 2015: Impacts of Cloud Droplet–Nucleating Aerosols on Shallow Tropical Convection. *J. Atmos. Sci.*, **72**, 1369–1385.

Schubert, W. H., 1976: Experiments with Lilly's Cloud-Topped Mixed Layer Model. *J. Atmos. Sci.*, **33**.

Schumacher, C., R. A. Houze Jr, and I. Kraucunas, 2004: The tropical dynamical response to latent heating estimates derived from the TRMM precipitation radar. *J. Atmos. Sci.*, **61**, 1341–1358.

——, M. H. Zhang, and P. E. Ciesielski, 2007: Heating Structures of the TRMM Field Campaigns. *J. Atmos. Sci.*, **64**, 2593–2610.

Sheffield, A. M., S. M. Saleeby, and S. C. van den Heever, 2015: Aerosol‐induced mechanisms for cumulus congestus growth. *J. Geophys. Res.*, **120**, 8941‐8952.

Simpson, J., R. H. Simpson, D. A. Andrews, and M. A. Eaton, 1965: Experimental cumulus dynamics. *Rev. Geophys.*, **3**, 387.

Singarayer, J. S., J. L. Bamber, and P. J. Valdes, 2006: Twenty-first-century climate impacts from a declining Arctic sea ice cover. *J. Clim.*, **19**, 1109–1125.

Small, J. D., P. Y. Chuang, G. Feingold, and H. Jiang, 2009: Can aerosol decrease cloud lifetime? *Geophys. Res. Lett.*, **36**, https://doi.org/10.1029/2009gl038888.

Sokolowsky, G. A., S. W. Freeman, and S. C. van den Heever, 2022: Sensitivities of Maritime Tropical Trimodal Convection to Aerosols and Boundary Layer Static Stability. *J. Atmos. Sci.*, **1**, https://doi.org/10.1175/JAS-D-21-0260.1.

Squires, P., 1958: The Microstructure and Colloidal Stability of Warm Clouds. *Tellus*, **10**.

——, and S. Twomey, 1960: The relation between cloud droplet spectra and the spectrum of cloud nuclei. *Physics of Precipitation: Proceedings of the Cloud Physics Conference*, *Geophysical Monograph Series*, American Geophysical Union Cloud Physics Conference, Washington D. C., American Geophysical Union, 211–219.

Storer, R. L., S. C. van den Heever, and G. L. Stephens, 2010: Modeling Aerosol Impacts on Convective Storms in Different Environments. *J. Atmos. Sci.*, **67**, 3904–3915.

Storer, R. L., S. C. van den Heever, and T. S. L'Ecuyer, 2014: Observations of aerosol-induced convective invigoration in the tropical east Atlantic. *J. Geophys. Res.*, **119**, 3963–3975.

Strauss, C., D. Ricard, and C. Lac, 2022: Dynamics of the Cloud–Environment Interface and Turbulence Effects in an LES of a Growing Cumulus Congestus. *J. Atmos. Sci.*, **79**, 593–619.

Sui, C.-H., K.-M. Lau, Y. N. Takayabu, and D. A. Short, 1997: Diurnal Variations in Tropical Oceanic Cumulus Convection during TOGA COARE. *J. Atmos. Sci.*, **54**, 639–655.

Takahashi, H., Z. J. Luo, and G. Stephens, 2021: Revisiting the entrainment relationship of convective plumes: A perspective from global observations. *Geophys. Res. Lett.*, **48**, https://doi.org/10.1029/2020gl092349.

Tanelli, S., E. Im, S. L. Durden, D. Giuli, and L. Facheris, 2008: Spaceborne Doppler radars for atmospheric dynamics and energy budget studies. *2008 IEEE Radar Conference*, 1–6.

Tao, W.-K., J.-P. Chen, Z. Li, C. Wang, and C. Zhang, 2012: Impact of aerosols on convective clouds and precipitation. *Rev. Geophys.*, **50**, https://doi.org/10.1029/2011rg000369.

Tompkins, A. M., 2001: On the Relationship between Tropical Convection and Sea Surface Temperature. *Journal of Climate*,.

Toms, B. A., E. A. Barnes, E. D. Maloney, and S. C. van den Heever, 2020a: The global teleconnection signature of the madden‐Julian oscillation and its modulation by the quasi‐biennial oscillation. *J. Geophys. Res.*, **125**, https://doi.org/10.1029/2020jd032653.

——, S. C. van den Heever, E. M. Riley Dellaripa, S. M. Saleeby, and E. D. Maloney, 2020b: The Boreal Summer Madden–Julian Oscillation and Moist Convective Morphology over the Maritime Continent. *J. Atmos. Sci.*, **77**, 647–667.

Twomey, S., 1974: Pollution and the Planetary Albedo. *Atmos. Environ.*, **8**, 1251–1256.

——, 1977: The Influence of Pollution on the Shortwave Albedo of Clouds. *J. Atmos. Sci.*, **34**.

Twomey, S.A., Piepgrass, M., Wolfe, T.L., 1984: An assessment of the impact of pollution on global cloud albedo. *Tellus B Chem. Phys. Meteorol.*, **36**, 356–366.

Ullrich, P. A., and C. M. Zarzycki, 2017: TempestExtremes: a framework for scale-insensitive pointwise feature tracking on unstructured grids. *Geosci. Model Dev.*, **10**, 1069–1090.

van den Heever, S. C., 2022: The INCUS Mission. ATS/CIRA Colloquium, 24 February 2022, Fort Collins, CO, USA.

——, G. G. Carrió, W. R. Cotton, P. J. DeMott, and A. J. Prenni, 2006: Impacts of Nucleating Aerosol on Florida Storms. Part I: Mesoscale Simulations. *Journal of the Atmospheric Sciences*, **63**, 1752–1775, https://doi.org/10.1175/jas3713.1.

——, G. L. Stephens, and N. B. Wood, 2011: Aerosol Indirect Effects on Tropical Convection Characteristics under Conditions of Radiative–Convective Equilibrium. *J. Atmos. Sci.*, **68**, 699–718.

——, and Coauthors, 2021a: The Colorado State University Convective CLoud Outflows and UpDrafts Experiment (C3LOUD-Ex). *Bull. Am. Meteorol. Soc.*, **102**, E1283–E1305.

——, S. M. Saleeby, L. D. Grant, A. L. Igel, and S. W. Freeman, 2021b: *RAMSmodel/RAMS: RAMS release version 6.3.01*.

Varble, A., 2018: Erroneous Attribution of Deep Convective Invigoration to Aerosol Concentration. *J. Atmos. Sci.*, **75**, 1351–1368.

Virtanen, P., and Coauthors, 2020: SciPy 1.0: fundamental algorithms for scientific computing in Python. *Nat. Methods*, **17**, 261–272.

Waite, M. L., and B. Khouider, 2010: The Deepening of Tropical Convection by Congestus Preconditioning. *J. Atmos. Sci.*, **67**, 2601–2615.

Walko, R. L., and Coauthors, 2000: Coupled atmosphere–biophysics–hydrology models for environmental modeling. *J. Appl. Meteorol.*, **39**, 931–944.

Wall, C., C. Liu, and E. Zipser, 2013: A climatology of tropical congestus using CloudSat. *J. Geophys. Res.*, **118**, 6478–6492.

van der Walt, S., and Coauthors, 2014: scikit-image: image processing in Python. *PeerJ*, **2**, e453.

Wang, Y., B. Geerts, and J. French, 2009: Dynamics of the Cumulus Cloud Margin: An Observational Study. *J. Atmos. Sci.*, **66**, 3660–3677.

Warner, J., and S. Twomey, 1967: The Production of Cloud Nuclei by Cane Fires and the Effect on Cloud Droplet Concentration. *J. Atmos. Sci.*, **24**.

Weaver, J. R., 1985: Centrosymmetric (cross-symmetric) matrices, their basic properties, eigenvalues, and eigenvectors. *Am. Math. Mon.*, **92**, 711–717.

Webster, P. J., and R. Lukas, 1992: TOGA COARE: the Coupled Ocean-Atmosphere Response Experiment. *Bulletin of the American Meteorological Society*, **73**.

Weickmann, K. M., 1983: Intraseasonal Circulation and Outgoing Longwave Radiation Modes During Northern Hemisphere Winter. *Mon. Weather Rev.*, **111**.

Weller, R. A., and S. C. Anderson, 1996: Surface Meteorology and Air-Sea Fluxes in the Western Equatorial Pacific Warm Pool During the TOGA Coupled Ocean-Atmosphere Response Experiment. *J. Clim.*, **9**.

Wood, R., C. S. Bretherton, D. Leon, A. D. Clarke, P. Zuidema, G. Allen, and H. Coe, 2011: An aircraft case study of the spatial transition from closed to open mesoscale cellular convection over the Southeast Pacific. *Atmos. Chem. Phys.*, **11**, 2341–2370.

Xue, H., G. Feingold, and B. Stevens, 2008: Aerosol Effects on Clouds, Precipitation, and the Organization of Shallow Cumulus Convection. *J. Atmos. Sci.*, **65**, 392–406.

Yanai, M., and R. H. Johnson, 1993: Impacts of Cumulus Convection on Thermodynamic Fields. *The Representation of Cumulus Convection in Numerical Models*, K.A. Emanuel, Ed., 39–62.

——, S. Esbensen, and J.-H. Chu, 1973: Determination of Bulk Properties of Tropical Cloud Clusters from Large-Scale Heat and Moisture Budgets. *J. Atmos. Sci.*, **30**.

Yuter, S. E., and R. A. Houze Jr, 1995: Three-Dimensional Kinematic and Microphysical Evolution of Florida Cumulonimbus. Part II: Frequency Distributions of Vertical Velocity, Reflectivity, and Differential Reflectivity. *Mon. Weather Rev.*, **123**.

Zhang, H., and Coauthors, 2022: Development and application of a street-level meteorology and pollutant tracking system (S-TRACK). *Atmos. Chem. Phys.*, **22**, 2221–2236.

Zhao, M., and P. H. Austin, 2005a: Life cycle of numerically simulated shallow cumulus clouds. Part I: Transport. *J. Atmos. Sci.*, **62**, 1269–1290.

——, and ——, 2005b: Life cycle of numerically simulated shallow cumulus clouds. Part II: Mixing dynamics. *J. Atmos. Sci.*, **62**, 1291–1310.

Zipser, E. J., 2003: Cloud Systems, Hurricanes, and the Tropical Rainfall Measuring Mission (TRMM). *Some Views on "Hot Towers" after 50 Years of Tropical Field Programs and Two Years of TRMM Data.*, *Meteorological Monographs*, American Meterological Society.

Zipser, E. J., and M. A. LeMone, 1980: Cumulonimbus Vertical Velocity Events in GATE. Part II: Synthesis and Model Core Structure. *J. Atmos. Sci.*, **37**, 2458–2469.

Zuidema, P., 1998: The 600–800-mb Minimum in Tropical Cloudiness Observed during TOGA COARE. *J. Atmos. Sci.*, **55**, 2220–2228.